Design of Metal Oxide-Based Electrodes for Efficient Photoelectrochemical Water Splitting

Dissertation

zur Erlangung des Doktorgrades

Dr. rer.nat.

vorgelegt der

Fakultät für Mathematik und Naturwissenschaften der

Technischen Universität Ilmenau

von

M. Sc. Nasori

Ilmenau

TECHNISCHE UNIVERSITÄT
ILMENAU

Gedruckt mit Unterstützung des Deutschen Akademischen Austauschdienstes

Die Arbeit wurde von Prof. Dr. Yong Lei betreut.

1. Gutachter: Prof. Dr. Yong Lei
2. Gutachter: Prof. Dr. J. Michael Köhler
3. Gutachter: Prof. Dr. Zhijie Wang
Tag der Einreichung: 14.09. 2017
Tag der wissenschaftlichen Aussprache: 28.02.2018

urn:nbn:de:gbv:ilm1-2018000076

Abstract

In order to overcome the disadvantages of conventional photocathodic and photoanodic materials, this dissertation focuses on the exploitation of new candidates for the development of highly efficient photoelectrochemical (PEC) systems. Consequently, high-performance photoelectrodes are prepared by the deposition of metal oxide semiconductor on different substrates by employing various methods such as electrodeposition and spin coating. Following methodologies are utilized for the preparation of highly efficient metal oxide-based photoelectrodes:

1. The fabrication of $CuBi_2O_4$ (CBO) films on FTO and FTO/Au substrates, respectively, through the electrochemical deposition approach. The observation indicated that the existence of the Au thin layer contributed to the improvement of crystal quality of the grown CBO films, promotion of photo-generated charge separation in the corresponding material and reduction of the resistance of the system. In comparison to the FTO/CBO, the FTO/Au/CBO photocathode exhibited an exceptional improvement in the photocurrent, from − 0.23 mA cm^{-2} to − 0.50 mA cm^{-2} at 0.1 V vs RHE. Once PEC system was optimized by depositing Pt nanoparticles on the CBO films, the plateau photocurrent has been further amplified to −1.24 mA cm^{-2}. These data present an attractive p-type material in photoelectrochemistry without pertaining to the corrosion problem in aqueous electrolytes.
2. P-type Cu_2O has long been regarded as an advantageous material in photoelectrochemistry due to its suitable band gap structure and cost-effective production. However, this promising material is prone to corrosion in aqueous electrolytes. To address this issue and attain a high photoelectrochemical performance, protective oxide layers and expensive catalysts have to be used. The complexity of such additional procedures, however, limits the further applications. Instead of utilizing surface protecting oxide layers and expensive catalysts, this dissertation reports the surface treatment of Cu_2O photocathodes using trisodium citrate (TSC) to enhance the photoelectrochemical performance. In comparison to the electrode without TSC, the photocathode of FTO/Au/Cu_2O/TSC/TiO_2/Pt shows a pronounced increment in photocurrent by a factor of about 2.

3. $BiFeO_3$ ferroelectric photoelectrodes breaks the limits imposed by common semiconductors. As a result of their prominent ferroelectric properties, photoelectrodes were able to tune the transfer of photo-excited charges generated either in $BiFeO_3$ or the surface modifiers by manipulating the poling conditions of the ferroelectric domains. At 0 V vs Ag/AgCl, the photocurrent could be switched from 0 mA cm^{-2} to 10 mA cm^{-2} and the open-circuit potential changes from 33 mV to 440 mV, when the poling bias of pretreatment is manipulated from –8 V to +8 V. Additionally, the pronounced photocurrent from charge injection of the excited surface modifiers could be quenched by switching the poling bias from +8 V to –8 V.
4. Fabrication of n-type $CuWO_4$ photoanode nanograin arrays by electrochemical deposition which results in the difference in-between distance initially performed with nanaoimprinted AAO template was successfully conducted. The effectivity and efficiency of the result on the control parameters disposition are indicated by photoelectrochemical performance with current density of 1.02 mA cm^{-2} (vs Ag/AgCl) under solar simulator 1.5G irradiation, as well as electron converted-radiation 1.78 % at a biased voltage of 0.7 V (vs Ag/AgCl). The length of in-between distance indicates the optimization of electrolyte penetration towards the interface and provides (a) a increased donor density of 2.86 $x10^{20}$ cm^{-3} at flat band voltage of 0.14 V (vs Ag/AgCl) and (b) quantum external efficiencies at wavelength around 410 nm. Then (c) the optimization of in-between distance of nanograin arrays is indicated as an assuring structure to increase photoelectrochemical water splitting performance.

Photoelectrodes based on metal oxides are promising candidates for the development of efficient PEC cells for the next generation energy applications. The structured semiconductor surfaces minimize the losses in the form of over potentials due to the low current flux per real area of the electrode. Hence, the present methodologies allow the effective utilization of earth-abundant metal oxides for innovating new generation PEC cells for various applications.

Kurzzusammenfassung

In Anbetracht der Nachteile konventioneller Photokathoden und Photoanodenmaterialien, fokkusieren wir uns auf die Erschließung neuer Kandidaten für hocheffiziente photoelektrochemische Systeme (PEC). Diese Dissertation befasst sich mit der Erforschung von Oxidhalbleitern hergestellt durch Elektrodeposition und Spin-coating, unterteilt sich in folgende Teilbereiche:

1. Die Herstellung von $CuBi_2O_4$ (CBO) Filmen auf FTO und FTO/Au Substraten durch elektrochemische Abscheidung. Die Beobachtung deutet darauf hin, dass die Existenz eines dünnen Goldfilms zur Verbesserung der Kristallqualität des gewachsenen CBO-Films, einer besseren Trennung photogenerierte Ladungsträgerpaare im entsprechendem Material und zur Reduktion des Widerstands im System beiträgt. Im Vergleich zu FTO/CBO zeigt die FTO/Au/CBO Photocathode eine ausergewöhnliche Verbesserung des Photostroms von –0,23mA cm^{-2} zu –0,50 mA cm^{-2} bei 0,1V vs. RHE. Das PEC System wurde weiter optimiert durch Abscheidung von Pt-Partikeln auf den CBO-Film, dadurch wurde der Photostromdichte weiter verstärkt zu –1,24 mA cm^{-2}. Diese Daten zeigen einen attraktives p-Typ Material in der Photoelektrochemie ohne betroffen zu sein von Korrosion in wässrigen Elektrolyten.
2. P-Typ Cu_2O wurde lange Zeit als vorteilhaftes Material in der Photoelektrochemie gehalten, durch seine geeignete Bandlückenstruktur und kostengünstige Herstellung. Jedoch zeigt dieses vielversprechende Material eine hohe Anfälligkeit für Korrosion in wässrigen Elektrolyten. Um dieses Problem zu adressieren und zu einer guten photoelektrochemischen Leistungsfähigkeit zu gelangen müssen schützende Oxidschichten und teure Katalysatoren eingesetzt werden. Die Komplexität solcher zusätzlicher Prozesse jedoch limitieren die weiteren Anwendungen. Anstelle die Oberfläche schützende Oxidschichten und teure Katalysatoren zu verwenden, kommt in dieser Arbeit eine Oberflächenbehandlung der Cu_2O Photokathoden mit Trisodium Citrate (TSC) zum Einsatz, welche die photoelektrochemische Leistungsfähiglkeit enorm steigern könnte. Im Vergleich der Elektrode ohne TSC Behandlung und mit, zeigt die Photokathode aus FTO/Au/Cu_2O/TSC/TiO_2/Pt eine deutliche Erhöhung der Photostromdichte um etwa den Faktor 2.
3. Ferroelektrische $BiFeO_3$ Photoelektroden durchbrechen die Limitierungen gewöhnlicher Halbleitermaterialien. Als ein Ergebnis ihrer typischen

ferroelektrischen Eigenschaften wurden Photoelektroden eingestellt auf den Transfer lichtangeregter Ladungsträger, erzeugt im $BiFeO_3$ oder den Oberflächen, durch Manipulation der Polungszustände der ferroelektrischen Bereiche. Bei 0 V gegen Ag/AgCl konnte der Photostrom geschaltet werden von 0 mA cm^{-2} zu 10 mA cm^{-2} und die offene Klemmspannung ändert sich von 33 mV zu 440mV wenn die Biaspolung der Vorbehandlung von –8V zu +8V geändert wird. Zusätzlich konnte der Photostrom von Ladungsträgerinjektion der angeregten Oberflächenattribute getilgt werden durch Änderung der Biasspannung von +8V auf –8V.

4. Strukturkonstruktion von Photoanoden aus n-Typ $CuWO_4$ Nanograin-Arrays mittels elektrochemischer Abscheidung und vorgeprägten AAO Templaten, resultierend in unterschiedlichen Zwischenabständen, wurde erfolgreich ausgeführt. Die Effektivität und Effizienz des Ergebnisses auf die Kontrollparameterbestimmung sind erkennbar durch photoelektrochemische (PEC) mit einer Stromdichte von 1,02 mA cm^{-2} (vs. Ag/AgCl) unter simulierter 1,5G Solarstrahlung, sowie einer Elektronen umgewandelten Strahlung 1,78% bei einem Bias von 0,7V (vs Ag/AgCl). Die Länge der Zwischenabstände zeigen eine Optimierung der Elektrolytpenetration zum Inteface (a) liefert Auswirkungen zur Erhöhung der Donatordichte $2{,}86 \times 10^{20}$ cm^{-3} in der Flachbandspannung, (b) externe Quanteneffizienz für Wellenlänge 410 nm. Und (c) die Zwischenabstände der Nanograin-Arrays wirk als eine sichere Struktur zur Erhöhung der Leistungsfähigkeit zur photoelektrochemischen Wasserspaltung.

Photoelektroden sind vielversprechender Kandidat für effiziente PEC Verbesserungen um die konventionellen erneuerbaren Energien in der Zukunft zu übertreffen. Strukturierte Halbleiteroberflächen sollen elektrokatalytische Verluste in Form des Überpotentials durch den geringeren Stromfluss per Oberflächeneinheit der Elektrode minimieren. Im Wesentlichen, durch niedrigere Aktivitäten könnte dieser Effekt es erlauben auf der Erde reichhaltig vorkommende Katalysatoren zu verwenden und eine ausgezeichnete Verteilung über die strukturierte Elektrode gewährleisten um die Nutzung der hochaktiven Edelmetallkatalysatoren zu ersetzen.

Acknowledgments

Four years is indeed a long time and I have been with many people who gave millions of memories. That is why; I would like to express my utmost gratitude to all of them especially to my advisor, Professor Yong Lei for providing invaluable guidance and continuous support throughout my study. The present research would have not been complete without his encouragement and helpful advices. Also, I would like to thank to scientists in the FG 3D Nanostructuring, Dr. Dawei Cao and Dr. Yang Xu for their friendship and support. I would also like to thank Dr. Huaping Zhao and Dr. Chengliang Wang, Dr. Min Zhu for their helpful suggestions and discussions. I am also grateful to Prof. Dr. Zhijie Wang in Laboratory of Semiconductor Materials Science, Institute of Semiconductors, Chinese Academy of Sciences, Beijing for his support and for suggestions.

I am extremely grateful to all members in ZMN and Institute of Physics. I especially thank Dr. Henry Romanus and Dr. Arne Albert for their help and suggestions during SEM measurements, Dr. Alexander Könkin for helping me in UV-Vis spectroscopy measurements, and Mr. Jens Schawohl and Dr. Grieseler Rolf for XRD measurements. I thank all group members in the FG 3D nanostructuring for their valuable suggestions, help, encouragement, wonderful friendship, and also keeping a nice place to work. Dr.rer.nat. Ranjith Vellacheri, Dr. rer.nat. Ahmad Al Hadad, Dr. rer.nat. Liaoyong Wen, Mr. Wenxin Wang, Ms. Liying Liyang, Mr. Shipu Xu, Mr. Rui Xu, and Ms. Dr.rer.nat. Samar al Hadad. I thank Mrs. Moumou Li for her help during my study at TU Ilmenau.

I thank Prof. Dr.rer.nat. Agus Rubiyanto, Dr. Ananta Kusuma Seta, Dr. Suhartanti, Dr. rer. nat. Ahmad Saufi and Miss Mahdalika in Education and Culture (BU-BPKLN) Bureau of Ministry of Education and Culture of Republic of Indonesia for stimulating my research interests in PEC water splitting and encouraging me to finish my study. I also express my indebtedness to all my friends and church members for their encouragement to complete my study and accommodating me. Especially, I would like to thank apl. Prof. Dr. Wahyu Wijaya Hadiwikarta and Miss. Risang Ayu for their help in measuring gas chromatography. Also, Mr. Max Sommerfeld and Mrs. Haruming Saraswati for heart-warming encouragements during my study.

I would like to thank all members in the Indonesian community particularly to all those in the Indonesian student association (PPI) in Ilmenau, Jena, and Nordhausen, to PCINU German, to members of the WA Group Ilmenau Ceria, to members of Pengajian Ilmenau and of course to those part of the Indonesian Embassy in Berlin.

I also want to express my gratitude to my family, Bapak Kusnan, Ibu Somirah, Ibu Hj. Rubiah, Madiun and Surabaya family for their love and support. There are no adequate acknowledgments to express my deepest gratitude. Without their support and love, I would not have accomplished this study. Finally, I am thankful to Farida Ariyanti and Fathurrahman An Nashori. Their continuous encouragement and supports helped me a lot.

Ilmenau, 14th September 2017

Nasori

Table of Contents

List of Figures

Abbreviation

AAO	anodic aluminum oxide
ALD	atomic layer deposition
AZO	aluminum doped zinc oxide
BCP	block copolymer
BFO	bismuth ferrite oxide
CA	cyclic anodization
CBO	copper (II) bismuth oxide
C cm^{-3}	volumetric energy capacity
CVD	chemical vapor deposition
CV	cyclic voltammetry
CWO	copper (II) tungsten oxide
CBO	copper bistmut oxide
D_{int}	interpore distance
D_p	pore diameter
E	electric field
E	potential (e.g., volts)
e	signed electron charge
E_a	activation energy
E_{cb}	conduction band edge energy
E_F	fermi level
E_{fb}	flat band potential
$E_{F,n}$	quasi-fermi level for electrons
$E_{F,p}$	quasi-fermi level for holes
E_g	band gap energy
E_{max}	theoretical maximum potential extractable from a photoelectrochemical
E_{vac}	vacuum level
E_{vb}	valence band edge energy
EBL	electron beam lithography
ED	electrochemical deposition
EDX	energy-dispersive detector X-rays
E_{DP}	depolarization electric field

EQY	external quantum yield
ES	electrochemical supercapacitors
FDTD	finite difference time domain
FTIR	Fourier transform infrared transmission
FTO	fluorine doped tin Oxide
J	current density
J-V	Current density-voltage
HA	hard anodization
HER	hydrogen evolution reaction
HRTEM	high resolution transmission electron microscopy
IPCE	incident photon to charge carrier efficiency
ITO	indium doped tin oxide
j_{limit}	limiting current
LIL	laser interference lithography
L_D	diffusion length
LSV	linear sweep voltammogram
MA	mild anodization
MIM	metal/insulator/metal
MTSTM	multi-tip scanning tunnelling microscopy
OER	oxygen evolution reaction
P	Porosity
PA	pulse anodization
PBR	pilling bedworth ratio
PDMS	poly-dimethylsiloxane
PEC	photoelectrochemical
PRET	plasmon resonance energy transfer
$Pt(MeCp)Me_3$	trimethyl(methylcyclopentadienyl) platinum (IV)
R	series resistance
SEM	scanning electron microscopy
$SnCl_4$	tin (IV) chloride
SPEIS	staircase potentio-electrochemical impedance spectroscopy
SPR	surface plasmon resonance

STH	solar-to-hydrogen efficiency
T	Temperature
TEM	transmission electron micrograph
TE	thermal evaporation
t_b	barrier layer thickness
t_w	pore wall thickness
$TiCl_4$	titanium (IV) chloride
TMAl	trimethylaluminum
TSC	trisodium citrate
U	anodizing potential
UPS	ultraviolet photoelectron spectroscopic
UV-Vis	ultraviolet-visible spectroscopy
UTAM	ultra-thin alumina mask
XRD	X-ray diffraction
XPS	X-ray photoelectron spectroscopy
µA	micro Ampere
ρ_p	pore density
1D	one-dimensional
3D	there-dimensional

Chapter 1. Overview

1.1 Introduction

Nowadays, the global energy demands are largely dependent on the supply of fossil fuels. These demands, besides that they are huge, are also increasing. Consequently, the production rate of oil and natural gas around the world is also bound to increase. It is also well predicted that in the near future, our existing supply can no longer fulfill the peaking global energy demand.[1,2] Besides this problem on the balance of energy supply and demand, the massive use of fossil fuels would also inevitably increase the level of abundance of carbon dioxide and other pollutants that are released to the environment. The last part may significantly contribute into the overall climate change in the globe. The exhaustions of fossil fuels [3] and the continuing climate change [4] have forced the society to shift from fossil-based energy carrier into a more efficient, cleaner, and renewable energy resources. Wind and solar energies are increasingly used as the alternatives because of their nature as renewable energy.[5] Electric mobility with minimum CO_2 emission is also rapidly developed.[6] Further exploration for alternative sources of clean energy and its efficient utilization are indeed a very significant issue.

Solar energy has long been valued as an inexhaustible source for producing electricity and clean fuels; also on the scale of the magnitude of the emitted energy that can be converted.[7] Up to now, a high diversity of devices has been developed to convert this solar energy into clean fuels and electricity, where many of them include sorts of PEC water splitting cells.[8-10] However, it remains as a challenge to portably use the converted energy or store and utilize them in an electrochemical way.

Planar configuration (thin film) is a common structure found on commercial devices that are available in the current market. With the advancement of the techniques for

material preparations and device fabrications, the energy conversion efficiencies of these devices are getting closer to the theoretical value. Increasing surface-to-volume ratio and large surface area enable the rapid and extensive energy conversion. To further improve the energy conversion and storage efficiencies, the idea to utilize nanoparticles and three-dimensional micro/nanostructures was introduced.[11,12] However, realizing this idea of functional devices with thin film of micro/nano particles and nanostructures remains as the one of the most challenging issues in today's nanotechnology.

Fabrication methods can be classified into two groups. The first method is top-down approach which involves the creation of a pattern on a larger scale and its subsequent reduction into nanoscale. Lithography is one of the predominant top-down techniques. This class of techniques has a significant drawback; it suffers from high cost and low throughput. The second type is bottom-up methods where the process commences with atoms/molecules and builds up to nanostructures. As the bottom-up approach involves the addition of building blocks to obtain nanostructures,[13,14] the research presented in this thesis to develop nanostructures can be categorized into this class additive structural creation.[14b] Bottom-up methods possess high throughput as these methods generally do not need expensive equipment for the fabrication of nanostructures. Moreover, these methods also provide an excellent control towards the morphology within the micrometer/nanometer regime. The combination of various deposition techniques to obtain thin film of micro/nanoparticles and also controlling the dimension of nanostructures is found to be beneficial for achieving high energy conversion efficiency. This will be one of the main discussions of this dissertation.

1.2 Outline

This dissertation is structured as given below:

- Chapter 2 presents the fundamentals of electrodeposition to fabricate semiconductors, especially semiconductor oxides and their growth as thin films, and information regarding nanoporous anodic aluminum oxide templates. This chapter also covers the challenges of growing thin films and nanostructure arrays of metal oxides. Besides, this chapter also includes the basics of PEC water splitting and the preparation of nanoimprinted AAO templates to develop highly ordered nanostructures. The fabrication of Cu_2O, $CuBi_2O_4$, and $CuWO_4$ by electrodeposition, and $FeBiO_3$ by spin-coating for PEC water splitting application is presented as well**.**
- Chapter 3 illustrates the techniques utilized for the characterization and performance analysis of the developed photoelectrodes.
- Chapter 4 focuses on the preparation of novel p-type CBO thin films on FTO substrates. Also, the methods to improve the performance of these CBO thin films, firstly through the contact modification by Au deposition and then by the deposition of additional Pt are discussed.
- Chapter 5 discusses the preparation and characterization of p-type Cu_2O thin films. In addition, this chapter also presents a method to further enhance the performance of p-type Cu_2O thin film-based photoelectrodes through the surface treatment using TSC, and the subsequent deposition of TiO_2 thin film as a protection layer and Pt as a catalyst.
- Chapter 6 presents the development of $BiFeO_3$ ferroelectric photoelectrodes by spin coating deposition on ITO glass substrate.
- Chapter 7 and Chapter 8 discuss the extended works which are focused on the preparation of n-type $CuWO_4$ nanograin arrays and p-type Cu_2O nanowire arrays, respectively, using AAO templates.

- Chapter 9 elucidates the summary and outlook of this dissertation.

Certain chapters in this dissertation are representing one or more papers published in or submitted to SCI-indexed international scientific journals. It should also be mentioned here that some chapters are self-contained.

Chapter 2. General Background

2.1 Fundamentals of electrodeposition

In recent years, electrodeposited semiconductor nanostructures have become popular in solar cells, solar selective coating and optoelectronics applications. However, in the case of certain metal oxides, it is still very challenging to achieve nanostructures through template-based electrodeposition. [15-18] Therefore, some research groups have developed alternative techniques for the fabrication of nanostrucutres of certain metal oxides such as TiO_2,[88] HfO_2[89] and WO_3[90], etc. Prerequisites to a high efficient and stable solar energy conversion in large-scale terrestrial application, electrodeposition of PEC thin film semiconductor emerges to fulfil the need for a low production cost. Since then, solar selective coatings based on oxides of Ni, Zn, Cr, etc. have been commonly used.[19,20] Today, by the utilization of all-electrodeposited thin films and nanostructure base on oxide p-Cu_2O, p-$CuBi_2O_4$, n-$CuWO_4$, and p-CuO/n-$CuWO_4$ cells, more than 10% PEC solar conversion efficiencies have been reported.[21-23]

The preparation of thin film and microstructure/nanostructure semiconductors with electrodeposition technique has some advantages over other physical and chemical deposition techniques. The semiconductor is easier to produce, more economical and leaving less residues. Electrodeposition purifies the material in process; therefore, it is not required to have very pure starting materials. Electrodeposition is not only useful for semiconductors, cases of binary semiconductors (such as Cu, Se, Ge, etc.), intermetallic compounds such as InSb, CuTe, NiTe, PbTe, etc., or ternary semiconductors like $CuInS_2$, $CuInSe_2$, $CuInTe_2$, etc., and oxide semiconductors can also take advantage of electrodeposition in their process of device formation. Semiconductor properties such as p-type or n-type conductivity, band-gap alignment, doping, control of stoichiometry, etc.

can be controlled within a reasonable accuracy. By monitoring the applied potential, applied current and deposition time, the deposition of materials can be controlled to obtain the desired structural parameters.[24-26]

Electrodeposition approach was initially employed successfully to prepare elemental semiconductors following the promising features in preparing the thin film PEC water splitting and solar cells.[27] Since it is an isothermal process which is mainly controlled by electrical parameters like electrode voltage and current density, they are easily adjusted to control film thickness, composition, and morphology. Electrodeposition commonly carry out in low operating temperatures. Apart from the clear advantages regarding energy saving, the low deposition temperature yields sharper junctions without deleterious effects of inter diffusion, contamination, and dopant redistribution, which is typical of high temperature processes. Electrodeposition is specifically suited for fabrication of heterojunction solar energy conversion cells. By simply changing the deposition electrolyte, an n-type film can be deposited onto a p-type substrate.

In electrodeposition technique, the flexibility is attractive. The plating could be employed as one of the steps in the preparation of binary or ternary semiconductors fabrication. Electrodeposition can be combined with electrochemical and/or chemical deposition and/or anodization to obtain the desired quality material. For instance, the preparation of $CuBi_2O_4$ which is an p-type and Cu_2O which is a p-type as a compound semiconductor with a different band gap i.e. 1.6 eV and 2.2 eV, respectively. It is a direct band-gap semiconductor and was utilized as a photoelectrode material in many applications such as solar cells, optoelectronic devices, and kindly for PEC.

Lokhande *et al.* and Fulop *et al.* in their publications [32] described electrodeposition process that later we adopted for the case of oxide semiconductor. [28-29] The procedures are listed as follows:

a. Direct cathodic electrodeposition from both aqueous and non-aqueous baths.
b. Electrodeposited copper (II) oxide films have been anodized in a copper, bismuth, and tungsten containing solution to obtain Cu_2O, $CuBi_2O_4$, and $CuWO_4$, respectively.
c. Results of both electrodeposited bismuth and tungsten are heated at high temperature in air in order to form $CuBi_2O_4$ and $CuWO_4$, respectively. But not for Cu_2O.

Most of solar energy conversion selective coatings use metal oxide-based or sulfides. They have a demanded band gap and other optical properties in relations to thermal emissivity and absorption. Such oxides or sulfides are prepared by metallic deposition followed by anodization or modification of the electrodeposition bath. The desired morphology for obtaining the pursued optical properties was easily done by the electrodeposition method.

A survey of thin film electrodeposited semiconductors in addition to special report for nanostructure will be further explored in this dissertation. The elemental, binary, and ternary semiconductors with their electrodeposition and physical-chemical properties are described. PEC cells fabricated from electrodeposited semiconductors will be presented as well as their solar conversion efficiencies.

2.2 Principle of electrodeposition for semiconductor

Theoretically, thermodynamically reversible potentials can be established only if some requirements are met under specific conditions. As previously reported[31,94], first, all the processes that provide the rise of electrodeposition of metal were rapidly compared to other competing reactions. Second, all soluble intermediate species were present in the solution at equilibrium concentration. Third, the element was pure and in a well-defined phase. Fourth, the deposited crystal grains were in their equilibrium form and stable.

Fifth, the crystals size was small by modifier conducting layer. Subsequently, the Nernst equation for electrodeposition of semiconductor is indicated as follows:

$$E_M = E_M^o + \frac{RT}{nF} ln\left(\frac{a_M^{+m}}{a_M}\right) \quad (2.1)$$

where E_M is the potential of the metal electrode in a given solution, $E_M{}^0$ is the standard potential for the reduction to form, R is the gas constant, T is the absolute temperature, n is the required number of electrons for the reduction, F is the Faraday constant, and a^{+m} and a_M, are the activities of M^{+m} metal ions in the electrolyte and of metal in the deposit, respectively. Electrodeposition of metal can happen at more negative potentials than in equilibrium potential due to the negligence of interactions of the solute of M^{+m} metal ions, with the solvent, or with the complexing ligands. In the latter case, the potentials are termed as overpotentials.

The conditions described above were rarely met in practice and therefore Kroger[32] introduced the "quasi-rest potentials" concept to help explaining zero current conditions that otherwise only estimate the true thermodynamic reversibility. There are a lot of kinetic factors influencing the deposition of elemental semiconductors that include the rate of the electron transfer reaction and dissociation kinetics of solvated or complex ions.

On the other side, the co-deposition of binary or ternary or compound semiconductors is quite difficult to attain since the favourable conditions for deposition of one of the metals can be different from those necessary for the other metals or constituents. Moreover, the electrodeposition may become complicated for compounds to obtain the desired stoichiometry that usually a necessary critical. Fulop *et al.*[34] presented various factors that influence the co-deposition of binary or ternary combinations of materials at any given current density and temperatures[33-37]. And these influencing factors are (i) individual ions that affect the electrode potentials in the electrolyte, (ii) differences of cathodic polarization in deposition potentials, (iii) relative ion

concentrations in the electrolyte, (iv) dissolving tendency of the deposited material in to the electrolyte solution, and (v) the hydrogen overpotential on the deposited cathode surface. Changes in electrolysis current density and electrolyte temperature can influence the aforementioned parameters. Although the direction of the effect of each variable is often predictable, it is practically impossible to estimate the scale of the magnitude of the change if two or more conditions are varied simultaneously.

As analysed by Brenner,[248] the condition for the concurrent deposition of two dissimilar components (such as A and B) at the cathode can be stated as given below,

$$E_A + \gamma^m = E_B + \gamma^n \qquad (2.2)$$

where E_A and E_B are the equilibrium potentials for the components A and B, respectively, and χ^m and χ^n are the over-voltages of components A and B, respectively. The equilibrium potentials of the components, the stability of the resultant deposit and the activities of the ions in solution are important in electrodeposition.

The equilibrium potentials of A and B are given below:

$$E_A = E_A^o + \frac{RT}{mF} ln\left(\frac{a_A^{-m}}{a_A}\right), \text{ and} \qquad (2.3)$$

$$E_B = E_B^o + \frac{RT}{nF} ln\left(\frac{a_B^{+n}}{a_B}\right) \qquad (2.4)$$

where R is the gas constant, T is the absolute temperature, m and n is the required number of electrons for the reduction and oxidation, F is the Faraday constant, a_A^{-m} and a_A, and a_B^{+n} and a_B are the activities of A^{-m} and B^{+n} in the electrolyte and of A and B in the deposit, respectively. Activities of components in the deposit are determined by the concentrations and the thermodynamic stability of the deposit.

Interplay between the components in a deposit, generally pushed the deposition potentials to the values that are positive with respect to the potential of the less noble metal. It is essential to consider the interaction energy of the components and also to the change in the point of zero charge due to the shift of the static potential that resulting in a

change in the overall kinetics. There is a broad diversity of components phase structures and consequently, electrochemical conditions during crystallization i.e. (i) eutectic mixtures of metals, (ii) homogeneous solid solutions, (iii) inter-compounds and (iv) mixture of different components. As an example, the process of electrodeposition is illustrated in Figure 2.1. The mechanism of electrodeposition of elemental or compound semiconductors can be listed as follows[38]:

a. The aqueous or complexed metal ion is deposited or transferred as an anion that is still partly bound to the surface site. Such sites include the plane surface, edges, crevices, corners, or holes within the plane.
b. The anion diffuses at the surface until it meets a growing edge, or step where further dehydration goes on.
c. Steady transfer or diffusion steps may follow into the airflow direction or vacancy or interact with other anions, accompanied by more dehydration until it is finally coordinated with other ions (and electrons) and becomes part of the component, incorporated into the lattice.
d. Deposition of metal ions results in depletion in the solution adjacent to the surface. Replenishment of ions is necessary for continuous deposition process. This replenishment or mass transport of ions can be achieved via three methods such as ionic migration, diffusion, and convection.

Based on the aforementioned points, the electrodeposition mechanism of Cu_2O on AAO template to acquire Cu_2O NWs array, from a copper sulphate bath carrying lactic acid and NaOH. The succeeding stage includes a deposition mechanism which count on the predominant species in the electrolytic bath, latic acid as lactate acid is a mono-valent acid, and it only can release one single hydrogen which it has, as explicated be denoted as given:

$$CH_3CH(OH)COOH \rightarrow CH_3CH(OH)COO^- + H^+ \quad (2.5)$$

It indicates that the lactate anions (Lac^-) would create complexes with the Cu^{2+} ions in the electrolytic bath in the form of $Cu(II)Lac_2$, while avoiding the precipitation of insoluble products at alkaline pH values.[249] The Cu(II) reduction in the lactate complex to Cu(I) and the formation of Cu_2O in this case would occur in a two-step process given by reactions 2.6 and 2.7 below:

$$[Cu(II)Lac_2] + e^- \rightleftharpoons [Cu(I)Lac_2]^- \quad (2.6)$$

$$2[Cu(I)Lac_2]^- + 2OH^- \rightleftharpoons Cu_2O + H_2O + 4Lac^- \quad (2.7)$$

These include the reduction of Cu(II) in the $Cu(II)Lac_2$ complex to Cu(I) in a $Cu(I)Lac_2$ complex, followed by the limitation of Cu^+ ions. Being pH-dependent, reaction 2.7 would be hindered when the pH decreases. Nevertheless, it is necessary to emphasize that when the electrode potential is negative enough, copper deposition would take place, based on the reduction reaction 2.8

$$[Cu(I)Lac_2]^- + e^- \rightleftharpoons Cu + 2Lac^- \quad (2.8)$$

following from reaction 2.6.

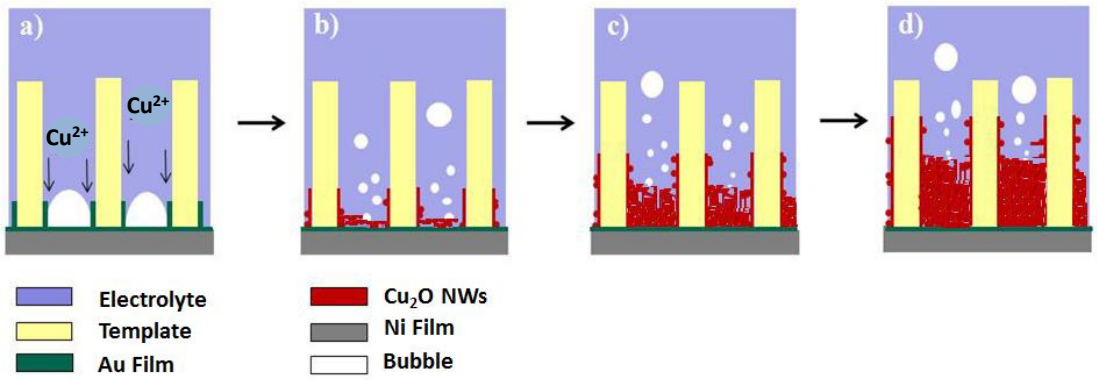

Figure 2.1 Mechanism for growth of Cu_2O NWs on AAO template with a thin layer of Au one of the sides during electrodeposition

The formation of such compound comprises the following order of necessary occurrences[90] (i) transfer of solvated cations to the cathode, resulting in a polarization accord, (ii) neutralization of a nobler ion, (iii) conversion of the cathode surface into the layer of adsorbed anions, (iv) complete depolarization of the cathode with respect to the less noble ion, (v) reduction of the less noble ion at the rate of first-order electron conductance, (vi) polarization of the cathode as the neutral character of surface is restored and (vii) building the crystal lattices and nano-macrocrystals of a compound: two or more participating elements, through repetition of polarization and depolarization steps.

2.3 PEC water splitting

In one cycle of PEC water splitting system, a single semiconductor with the appropriate band gap energy (E_g) is sufficiently large to split water, and with a conduction band-edge energy (E_{cb}) and valence band-edge energy (E_{vb}) that straddles the electrochemical potentials $E°(H^+/H_2)$ and $E°(O_2/H_2O)$, can drive the OER and HER by using electrons or holes produced under illumination. This indicates that semiconductor has to absorb radiant light with photon energies of larger than 1.23 eV and converting the energy into H_2 and O_2, where according to Nernst equation, based on $\Delta E° = 1.23$ V per electron transferred from free energy change for the conversion of one molecule of H_2O to H_2 and 1/2 O_2 under standard conditions (ΔG = 237.2 kJ/mol). For OER or HER without recombination, photo-induced free charge carriers (electrons and holes) in the semiconductor must surpass a liquid junction and the carriers must react only with solution species directly at the semiconductor surface. Otherwise, the electron-transfer processes at semiconductor/electrolyte junctions would induce energy losses due to the concentration and kinetic overpotentials, although they are needed to drive the OER and the HER.

The overpotentials needed to drive water splitting reaction ($H_2O \rightarrow ½\ O_2 + H_2$) are particularly essential for supplanting the valence-band and conduction-band edge positions of a semiconductor corresponding to the potentials for the hydrogen ($2H^+ + 2e^- \rightarrow H_2$) and oxygen ($H_2O + 2(h)^+ \rightarrow ½\ O_2 + 2H^+$) evolution reactions.[39-42] When the potential of a valence band is not high enough for water oxidation, or when its conduction band is not low enough for proton reduction, water splitting reaction can be slow or in the range of negligible value.[39-42]

Not only demonstrating an optimal band gap for solar absorption, semiconductor photoelectrodes have also shown excellent oxidative/reductive stability in its contact with aqueous electrolyte solutions. For thermodynamic stability, a semiconductor reductive and oxidative decomposition potentials must be more positive than semiconductor valence band-edge potential for water oxidation, or must be more negative than semiconductor's conduction band-edge for water reduction. Only very limited number of semiconductor materials demonstrate the necessary requirements for electrode stability in aqueous electrolyte solutions for both water oxidation and reduction simultaneously.[40] The simplification by theoretical efficiency is based on the conversion of the incident solar energy to chemical energy, as shown in the equation below:

$$\eta_s = \frac{V_{OC}|J_{SC}|FF}{P_s} \qquad (2.9)$$

Where V_{OC}, J_{SC} and FF, for closely ideal cell have been usually treated almost as independent parameters in the reference. The equation above, that could also be describe below:

$$\eta = \frac{J_g \mu_{ex} \varphi_{conv}}{S} \qquad (2.10)$$

where J_g is the absorbed photon flux, μ_{ex} is chemical overpotential generated by light absorption, ϕ_{conv} is quantum yield for the absorbed photons, and S indicates the total incident solar irradiance (mW cm^{-2}).

In order to calculate efficiencies for water splitting photoelectrode devices, an external bias to drive water electrolysis is required, equation of 2.10 can be applied (assuming there is no corrosion reaction at photoelectrodes and a Faradaic efficiency are in the close agreement in both reactions). As opposed to a three-electrode electrochemical cell, these measurements should be performed in a two-electrode configuration to obtain the true systems efficiency. The efficiency (η) is calculated from J-V data by using the following equation:

$$\eta = \frac{P_{stor}}{P_{in}} = \frac{J_{ph}}{P_{in}}\left(1 - \frac{kT}{\Delta E_{F,max}}\right)\Delta E_{stor} \qquad (2.11)$$

where ΔE_{stor} is the storable energy. If we assumed that

$$\Delta E_{F,max} \geq \Delta E_{stor} + e\eta_{ox} + e\eta_{red} \qquad (2.12)$$

and on other hand, we found $P_{stor} = 0$ for

$$\Delta E_{stor} + e\eta_{ox} + e\eta_{red} \geq \Delta E_{F,max} \qquad (2.13)$$

In the short range between $\Delta E_{F,s}$ and $\Delta E_{F,max}$ is:

$$P_{stor} = J_{ph}\left[\left(1 - \exp\frac{\Delta E_{stor} + e\eta_{ox} + e\eta_{red} - \Delta E_{F,max}}{kT}\right)\right]\Delta E_{stor} \qquad (2.14)$$

In assuming$\Delta E_{stor} = 1.23\ eV$, finally corresponding efficiency could be of use equation below:

$$\eta = \frac{J_{mp}(1.23\ V - V_{app})}{P_{in}} \qquad (2.15)$$

where J_{mp} is current density measured externally, V_{app} is applied voltage measured between oxygen-evolving photoanode and hydrogen-evolving photocathode, while P_{in} is the power density of the illumination.

From current−voltage data gathered from employing a potentiostat in an illuminated three-electrode cell, the solar conversion efficiency of individual potential photoelectrode materials that might be utilized in a multiple band gap photoelectrolysis cell to drive either the HER or OER can be measured. In order to allow the independent optimization

of the materials, it is useful to calculate efficiencies of a photoanode or photocathode apart from the other half of water splitting reaction. Characterization of individual photoelectrodes generated by the power, represents a part of the Gibbs free energy required in splitting water that is important to be acknowledged.[43-45] Therefore, open-circuit voltage (V_{oc}) and short-circuit current density (J_{sc}) are referenced to the thermodynamic potential of the water splitting reactions (H^+/H_2, O_2/H_2O) at a certain pH.

By independently characterizing photoanodes and photocathodes, the expected performance of an integrated system with no external electronics can be calculated directly. The overall water splitting efficiencies STH for photoelectrolysis cells can be estimated by overlapping the individually tested J-V data for each photocathode/anode (Figure 2.2).[39,46] The intersection of the two curves indicates the maximum operating current density (J_{op}) for the complete cell. The maximum efficiency for a p/n- PEC cell will be obtained when the two curves intersect the closest to their individual maximum power points (P_{PC} or $P_{PA} = J_{mp} \cdot V_{mp}$, maximum power for photoanode P_{PA} or photocathode P_{PC}). A theoretical p- or n-PEC photoanode/photocathode device is illustrated in Figure 2.2, describing the power produced for every cell component (shown as green shaded area) and the power generated at the maximum operating current density (shown as yellow shaded area).

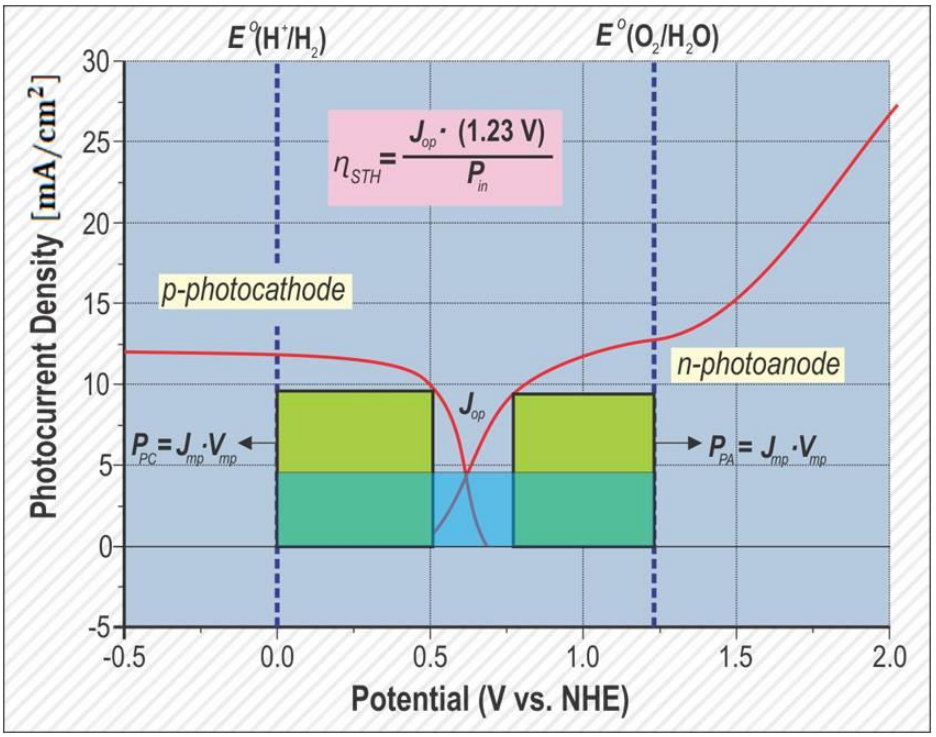

Figure 2.2 Overlaid current density-potential behavior of a p-type photocathode and an n-type photoanode, with overall efficiency projected by the power generated $P_{STH} = J_{op}$ (1.23 V) by the cell for water splitting. (Modification based on figure from ref. 46).

2.4 Applications of electrocatalysts for solar water splitting

At present, there is no shortage of available options of HER and OER catalyst. However, the specific concerns are related to the attachment of catalysts directly to semiconductor surfaces that place significant constraints on which of the known systems can, or should, be utilized.

Several considerations make the development and utilizations of catalyst materials to be used in splitting water systems, and coupling these catalysts to light-absorbers, different from catalysts utilization in standard electrolysis. One of the most significant differences is that light-coupled electrolysis needs absorbers with large areas to maximize solar flux capture. When a catalyst is directly deposited on the absorber surface, it will drastically lower the requirements for current production per unit geometric area.

Consequently, commercial electrolysis systems run at current densities as high as 1 A cm^{-2}, while approximately a hundred-fold smaller flux.

Concomitant to the reduced material performance requirements, however, a more stringent requirement on the cost of catalyst materials appears, as comparatively more mass of catalyst is likely to be required in covering the relevant area. Many of the problems with the stability of conventional metal, metal oxide electrodes, and metal composite is attributed to the requirement of running electrolyzers at high current densities, in highly caustic environments, and at elevated temperatures. In semiconductor-coupled systems, none of these are required. Thus, in these cases catalysts can be expected to be more robust.

Another method to explain this behavior is evaluating the photocurrent density required in matching the incoming solar flux in a light-coupled cell, based upon the geometrical (i.e., projected) area of the cell. Catalyst or absorber substrate which is highly structured could have an active surface area ten times larger than its projected area. It brings an implication that the coupled catalysts would only need to produce a few $mA.cm^{-2}$ of electrochemically active catalyst area. As a result, high surface-area forms of cheap, large materials, e.g. pure transparent nikel, could be sufficient to serve the catalysis needed for those types of systems.

Photoelectrolysis catalysts must not obscure a high fraction of light incident on the surface. Transition metal or conductive metal oxide catalysts will oftentimes absorb or reflect some of the light, lowering the resulting efficiency. A thick and continuous catalyst layer with an extremely high surface area like that found in industrial electrolyzers, while might be sufficiently catalytic, is practically useless for a semiconductor-coupled system. This is because the metal over layer will absorb or reflect almost all the incident light. Concerns over both light absorption/reflection and catalytic

activity can possibly be mitigated together either by developing catalysts that are TCO or by moving toward systems in which both the catalyst and the absorber are micro- or nanostructured, so as to produce a high surface area for both. Alternative choice is to actually take advantage of the optical properties of a catalyst material or an absorber so as to enhance rather than to diminish light absorption.[169]

There is another unique consideration to light-coupled water splitting systems, which is the set of restrictions on the deposition of catalysts imposed by the nature of the absorber material. Specifically, high-temperature and/or metallurgical preparation methods are not likely to be useful due to the likelihood of undesired reactions with the absorber medium under such conditions, e.g. silicide formation for metallic catalysts on common semiconductors Si at high temperatures. Solution-phase (electro and electrolyzers) and vacuum (evaporation, sputtering) deposition processes are instead necessary to protect the absorber integrity. This constraint renders many of the most active and robust dark HER and OER catalysts inaccessible, unless alternative processing methods can be developed in creating materials that have comparable catalytic activity and stability.

Another essentially unique consideration to light-coupled water splitting systems is the need for contacting semiconductor intimately with catalyst material. In the case of semiconductor/liquid junctions, for instance, it will be crucial to ensure that highly rectifying or appropriately “pinched off” contacts are taken place between metal and semiconductor. Furthermore, interfacial energy states created at metal−semiconductor contacts could enlarge interfacial recombination losses, causing inclination to decreased voltages and resulting in losses in efficiency.

2.5 Micro and nanostructure effects on the efficiency of photoelectrodes

Recently, most current interest has been addressed to the utilization of micro-nanostructured electrodes for solar energy conversion in the form of either photovoltaics or direct photoelectrolysis cells.[45,81,169] Compared to a planar system, the main advantages usually associated to a structured electrode are the decoupling of the directions of light absorption and charge-carrier collection.[38,172] At the beginning, discussing about conducting band related as a measure the potential before the distance which a minority carrier can diffuse before recombining is termed as the diffusion length (L_D) and is formulated as equation below:

$$J_{p,n} = e\mu_{n,p}\left((n,p)\mathcal{E} + \frac{kT}{e}\nabla p,n\right)$$

$$= \mu_{n,p}\left[-\nabla(E_c) + e\mu_{n,p}\frac{kT}{e}\left\{\frac{n,p}{kT}(\nabla(E_c) - \nabla(E_{F,(n,p)}\right\}\right]$$

$$= \mu_{n,p}\nabla(E_{F,(p,n)} \qquad (2.16)$$

The diffusion coefficient is proportional to the minority-carrier mobility, μ ($m^2\ V^{-1}\ s^{-1}$), by the Einstein relation, equation (2.17):

$D_n = \frac{k_B T}{e}\mu_n$ for electron, and

$D_p = \frac{k_B T}{e}\mu_p$ for holes (2.17)

Therefore, herein assume that there is in linear concentration profile over a distance which corresponds to diffusion length as defined by:

$$L_D = (D\tau)^{1/2} \qquad (2.18)$$

where τ is minority-carrier lifetime and D is the minority carrier diffusion coefficient.

The direction of light absorption in a traditional, planar solar cell is the same as that of charge-carrier collection. Therefore, to build an efficient cell, the absorber must be not only sufficiently thick to absorb all the light but also must be of sufficient electronic

quality (i.e., purity and crystallinity) such that the excited minority carriers photogenerated deep within the sample are able to diffuse to the surface, where they can be collected. This constraint requires that the absorption length $L_D \geq 1/\alpha$, with α is the absorption coefficient of the semiconductor near the band gap energy. In order to achieve sufficient diffusion lengths in a planar geometry, high purity semiconductors along with few defects that function as recombination sites in general must be employed.

The requirement in diffusion length can be decoupled from the absorption length if non-planar geometries, for example a semiconductor rod array, are implemented (Figure 2.3). As has been indicated through device physics modelling, and explained experimentally in several different configurations[38,47-51], high surface area semiconductor structures shorten the distance which minority carriers must travel, and hence enable the near-unity collection efficiencies despite short minority carrier diffusion lengths.

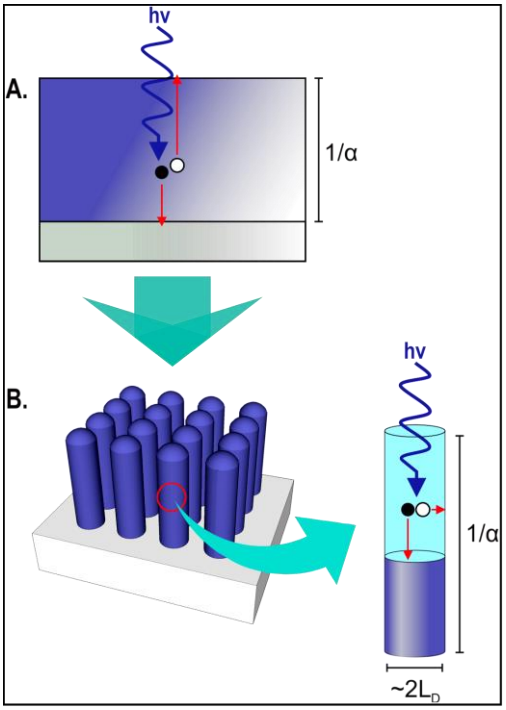

Figure 2.3 Thin film as a planar device (A), before collecting the carrier, photogenerated charge must traverse the entire thickness of the cell around ~1/α, where α is the

absorption coefficient. In a grain or wire-array cell (B), carriers must only reach the core surface before recombination. L_D is the diffusion length of the photogenerated minority carrier (open circle), (modification from ref. 46).

Increasing the junction area of a semiconductor photoelectrode via micro-nano structuring has also been demonstrated to lower the V_{oc} and in this respect is detrimental to device performance.[47,51] This behaviour is expected from an essential analysis of the dependence of V_{oc} on the dark and light currents. The phenomenon of decreased V_{oc} upon increased junction area is caused from the reduced splitting in the quasi-Fermi levels when the photogenerated charge carriers are diluted over a large junction area.[51-55] This situation holds even in the ideal case when surface recombination is negligible and recombination in the quasi-neutral of bulk region dominates the system performance. The photovoltage is predicted to decrease by around 60 mV per order of magnitude increase in junction of the semiconductor/electrolyte area.

Practically, the implication of this effect implies that the junction area should be enhanced enough to collect all the carriers radius of L_D but not more, in order to achieve the highest performance from a rod-array electrode. This analysis also suggests that unless their geometries also significantly enhance light absorption, highly nano-structured semiconductor electrodes will prone to a loss in $V_{oc,}$ thereby offsetting the loss from charge-carrier dilution.

2.6 Nanoimprinted AAO template

2.6.1 Structure of nanoimprinted AAO template

This section is elaborated the nanoimprinted AAO template as one important part of this dissertation. Figure 2.4(a) exhibits a representative schematic structure of AAO template, along with SEM images of key features of the nanoimprinted AAO template,

including top surface, barrier layer and bottom surface. Nanoimprinted AAO template has a numerous mutually honeycomb-like nanopores. Every cylindrical nanopore and its surrounding oxide composes a hexagonal cell aligned normal to the metal surface. At the metal/oxide interface, a thin barrier oxide layer with an approximately hemispherical morphology closes the nanopore. The oxide cells are self-organized to form a hexagonally close-packed structure, under proper anodization conditions. On the other hand, the surface of the aluminum after complete removal of the porous oxide layer is textured with arrays of concave features.

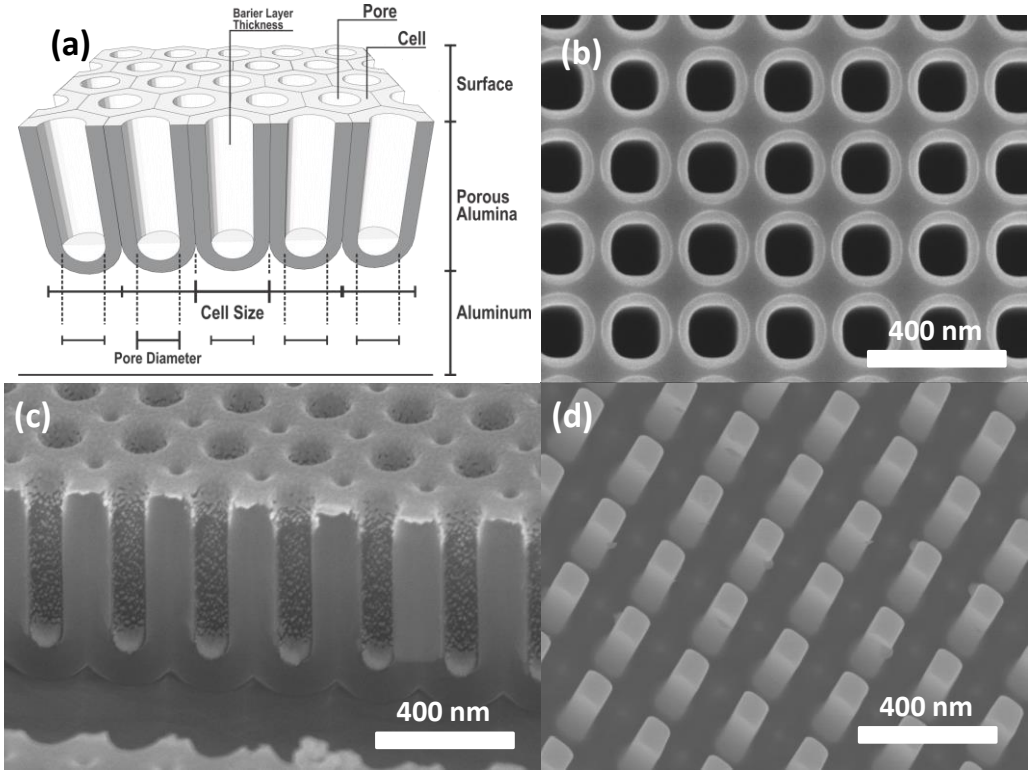

Figure 2.4(a) Schematic structure of nanoimprinted AAO template after the anodization on Al foil. SEM images of nanoimprinted AAO template: (b) top surface, (c) barrier layer, and (d) top view after removed the nanoimprinted AAO templates, respectively.

The thickness of the AAO template on aluminum is proportional to the total charge (Q_c) involved in the electrochemical oxidation. Thus, the depth of nanopores is easily

tunable about tens of nanometers aim hundreds of micrometers by controlling anodization time (t). Generally, the structure of self-ordered AAO template is frequently defined by some structural parameters, such as between pore distance (D_{int}), diameter of pore (D_p), barrier layer thickness (t_b), wall thickness of pore (t_w), pore density (ρ_p), and porosity (P). For ideally ordered porous nanoimprinted AAO template, the following relationships can be drawn by using simple geometric consideration:

$$D_{in} = D_p + 2t_w(\text{in nm}) \tag{2.19}$$

$$\rho_p = \left(\frac{2}{\sqrt{3D_{int}^2}}\right) \times 10^{14} cm^{-2} \tag{2.20}$$

$$P(\%) = \left(\frac{\pi}{2\sqrt{3}}\right)\left(\frac{D_p}{D_{int}}\right) \times 100 \tag{2.21}$$

nanoimprinted AAO template structural parameters are recognized to be dependent on the anodizing conditions: anodizing potential (U), current density (j), the type of electrolyte, temperature (T), etc. Among those conditions, anodizing potential (U) and current density (j) are the most important electrochemical parameters[72].

2.6.2 Formation of nanoimprinted AAO template

Generally, potentiostatic anodization is commonly used for fabricating self-ordered porous nanoimprinted AAO template, due to the linear dependence between the applied potential (U) and the structural parameters of the resultant nanoimprinted AAO template. Figure 2.5a and Figure 2.5b exhibit a typical current (j) − time (t) curve for constant-potential anodization, and potential (U) − time (t)

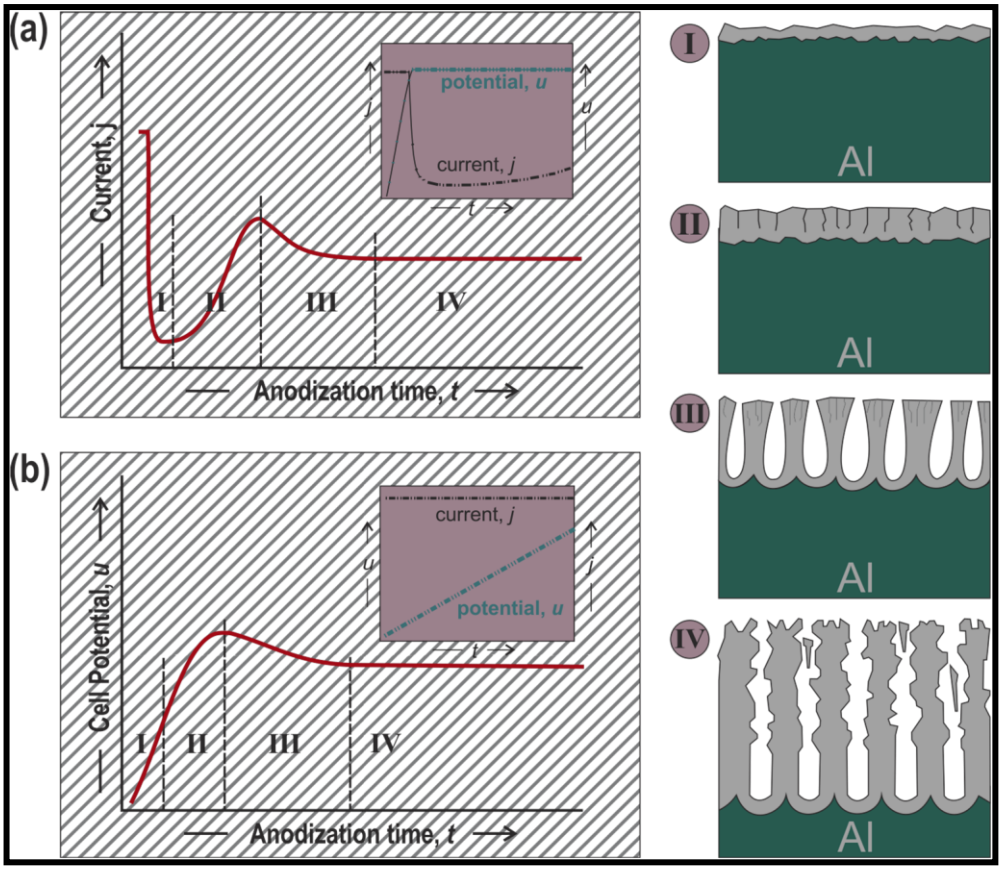

Figure 2.5 Schematic diagram of the kinetics of porous growth in potentiostatic (a): current (j) − time (t) curves, and galvanostatic (b): potential (U) − time (t) curve, together with stages of nanoimprinted AAO template development (c). (Figures are taken from ref[68]).

curve for constant current anodization, along with schematic illustrations of the stages of porous structure formation (Figure 2.5c). When a constant-potential (U) is applied, gradually compact barrier oxide starts to grow over the entire aluminum surface (stage I). Consequently, the thickening of the initial barrier oxide over time (t) resulting in an increase of series resistance (R) of the anodization circuit. Current (j) effect is initially maintained at the limiting current (j_{limit}) of the power supply and appropriately, potential ($U = jR$) increases linearly with time (t) (see the inset of Figure 2.5a). Because of the increasing thickness, which is proportional to the resistance R, the compact barrier oxide

layer reaches a particular value where current (j) decreases rapidly to hit the minimum (stage II). In this regard, O'Sullivan and Wood[68] suggested that current that concentrates on local imperfections (e.g., defects, impurity, pits) that exist on the antecedent barrier oxide, resulting in irregular oxide thickening and pore excitement at the thinner oxide areas. Thompson and co-workers [11,69-71] have proposed that local cracking of the initial barrier oxide due to accumulated tensile stress (PBR < 1) may build the paths for electrolyte penetration. Local increase in field strength at the penetration paths effectively polarizes the Al−O bonds, facilitating field-assisted oxide dissolution and eventually leads to the development of individual penetration paths into embryo pores.[76] Accordingly, further anodization leads to a gradual increase in current (j) to a local maximum because of the ready diffusion of electrolyte (stage III). Afterwards, current (j) reaches a steady state after leave an overshoot (stage IV). The arrival of current overshoot has been associated to the decrease of the initial pore density with the steady-state growth of major pores: pores increase in size by persistent merging with adjacent pores.[72-73] For a given set of anodization conditions, the potential rate increases at the first of anodization, the value of the minimum current necessary, the time anodizing current to reach a steady value and the present of the current overshoot has been known to be directly dependent on the anodizing potential (U), electrolyte pH, temperature, and lastly the initial surface state of the aluminum.[74,75]

In the case of galvanostatic anodization, a similar progression can be observed for stages I−IV, while the potential (U) changes as a function of time (Figure 2.5b). Under constant-current conditions, the oxide growth rate should be proportional to the applied current density (j) and constant according to the Faraday's law. In addition, a constant electric field ($E = U/t_b$) is required to sustain the applied constant current (j)[77-79]. Accordingly, the potential (U) increases linearly proportional to the thickness of the

growing barrier oxide (t_b) as shown in the inset of Figure 2.5b. In practice, however, the evolution of potential (U) deviates from a simple linear behavior as time increases (Figure 2.5b). But, for convenience, various mechanisms governing such a deviation have been referred to as growth instabilities, which include, for example, mechanical breakdown during zirconium anodization and surface undulation/pore initiation during aluminum anodization.[75,80] Figure 2.5b shows a gradual deceleration of potential (U) increase at stage II. A potential evolution like this could also be attributed to morphological instability, which is a transition from the stage of barrier oxide growth to the stage of porous oxide growth.

Chapter 3. Experiments, Instrumentations and Calculations

3.1 Electrochemical deposition

In general, electrochemical deposition is used for growing metals, metal oxides, and conductive polymers for the following advantages: (i) the thickness and morphology of the nanostructure can be controlled precisely by adjusting electrochemical parameters, (ii) relative uniform and compact deposits can be synthesized in template-based structures, (iii) higher deposition rates are obtained, and (iv) the equipment is inexpensive because of the absence of either a high vacuum or a high reaction temperature.[67] A simple modification in electroplating process is pulse electroplating. This process involves the swiftly alternating of the potential or current between two different values resulting in a series of pulses of equal amplitude, duration and polarity, separated by zero current. It is possible to change the composition and thickness of the deposited film and nano arrays by changing the pulse amplitude and width. All the electrochemical depositions in this dissertation are performed by using an electrochemical workstation (BioLogic, Inc.).

3.2 Atomic layer deposition (ALD)

ALD has attracted much attention as a versatile methodology for thin film deposition because of conformal and uniform deposition of thin films on substrates with complicated 3D morphology.[67, 83] In ALD, a thin film of desired material is developed in a layer-by-layer manner by repeating a reaction cycle constructed within four consecutive steps: (i) reactant A exposure, (ii) purge (or evacuation) of unreacted excess gas molecules and reaction byproducts, (iii) reactant B exposure, and (iv) subsequent purge. So far, a wide range of materials has been grown by ALD.[79,88-90] The materials encompass metals (Pt, Ru, Pd, Ir, et al.), insulators (Al_2O_3, HfO_2, et al.) and

semiconductors (ZnO, TiO_2, TiN, CuS, et al.) in both crystalline and amorphous phases. In this dissertation, five types of materials, including TiO_2, ZnO, Al_2O_3, SnO_2, and Pt, are prepared for the different purpose. All of the ALD reactions in this dissertation are carried out in Picosun SUNALETM R150 ALD System.

3.2.1 Atomic layer deposition of TiO_2

Titanium (IV) chloride ($TiCl_4$, Sigma-Aldrich) and distilled-water (H_2O) are used as the precursors of Ti and O, respectively. During the deposition process, the reactor was held at a temperature of 300 °C and the N_2 carrying gas was kept at 100 sccm. The detailed recipe for TiO_2 growth is revealed in Figure 3.1. The growth rate of TiO_2 is approximately 0.6 nm per cycle and the cycle numbers are defined by the purpose.

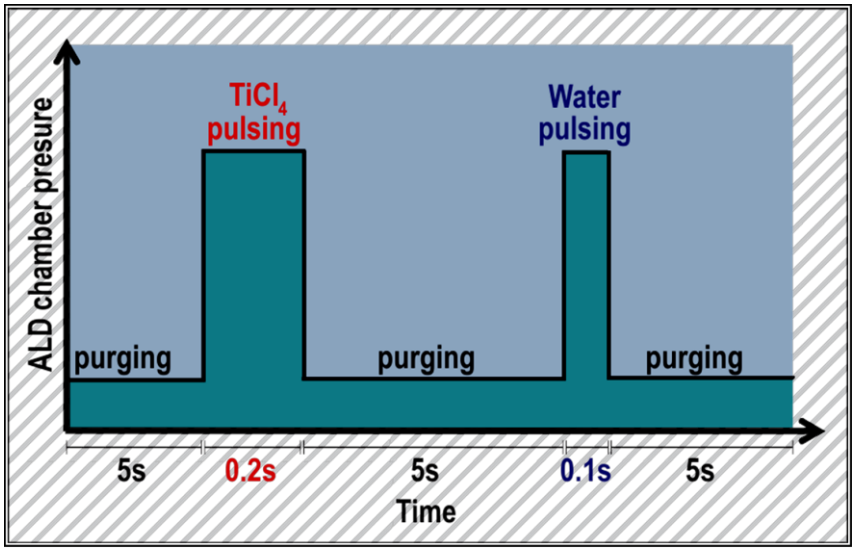

Figure 3.1 One cycle of TiO_2 growth, including the N_2 purging, $TiCl_4$ pulsing, and H_2O pulsing times.

3.2.2 Atomic layer deposition of Pt

Trimethyl (methylcyclopentadienyl) platinum(IV) ($Pt(MeCp)Me_3$, 98%, Sigma-Aldrich) and Oxygen gas (O_2) are used as the precursor of Pt. The reactor is controlled at a temperature of 300 °C, while chamber pressure varies from 8 hPa to 30 hPa under

different deposition steps. The temperature of $Pt(MeCp)Me_3$ canister was maintained at 80 °C. The N_2 carrying gas is kept at 100 sccm, during the deposition process, the pressure values for $Pt(MeCp)Me_3$ line and O_2 line was ~ 10 hPa. The innovative recipe for Pt growth is revealed in Figure 3.2. First, the N_2 carrying gas was kept at 100 sccm. Next, during the low N_2 filling period, the N_2 carrying gas was decreased to 60 sccm, the pressures for $Pt(MeCp)Me_3$ line and O_2 line in low N_2 filling period was ~ 28 hPa. One typical innovative ALD growth cycle consists of $Pt(MeCp)Me_3$ pulsing (1.0 s)–low N_2 filling (60 s)– N_2 purging (18 s)–O_2 pulsing (1.0 s)– low N_2 filling (60 s) –N_2 purging (18 s).[163]

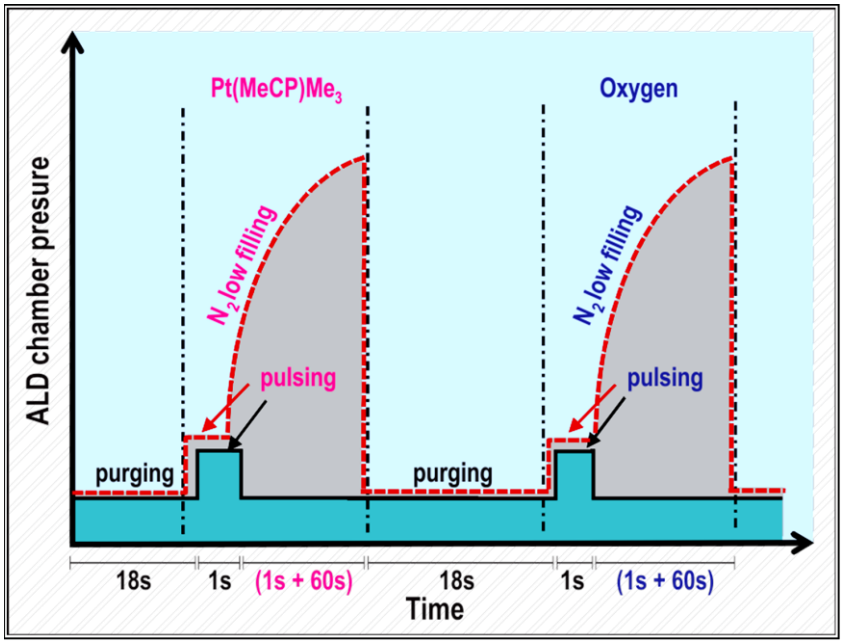

Figure 3.2 Conventional (solid line) and innovative (dot line) recipes of Pt growth (1 cycle).

3.3 Preparation of nanoimprinted AAO templates

For imprinting template we describe several points as follows:

(1) Al foil preparation: High-purity (99.99+%) aluminum foil of about 0.22 mm thickness was used as the starting material. The aluminum foil was first degreased with acetone, and then ethanol for 10 min, respectively; finally, it is electropolished in a 1:9 solution of perchloric acid and ethanol.

(2) Ni imprinting mold preparation: First, Silicon master was molded with nanohole array (400 nm and 800 nm spacing, square- and hexagon-arranged, AMO GmbH) is rinsed in Piranha solution (H_2SO_4/H_2O_2; 3:1) for 30 min with ultrasonication. After that, surface modification was carried out by treating Si master mold with 3-aminopropyltriethoxysilane (3-APTES; 1.0 vol% in CH_3CH_2OH) at 65 °C for 1h. Then, a 15 nm thick Au layer was evaporated on the surface of Si master mold by EBPVD. Au layer was used as a conductive layer for subsequent Ni film electrodepostion. Ni film electrodeposition was conducted in a Ni plating solution. The typical current density for Ni electrodeposition is 10 mA cm^{-2}. After the electrodeposition, Ni imprinting mold with ordered nanorod array is reached by stripping Ni film from Si master mold and Si master mold can be recycled many times without noticable damages.

(3) Imprinted template preparation: Ni imprinting mold is used for the imprinting process on Al foil. Typically, the imprinted Al foil was attained by applying a pressure of about 10 kN cm^{-2} for 3 min by using an oil pressing system. About 1 cm2 nearly defect-free imprinted areas have been successfully obtained, in which the formed concave pattern thereby as the initial sites to guide the template growth in the subsequent anodization. For 400 nm spacing imprinted Al, anodization was carried out under a constant voltage of 160 V in a H_3PO_4 solution (0.4 M) at 15°C, where the anodization voltage is chosen to satisfy the linear relationship between the interpore distance and the anodization voltage (2.5 nmV^{-1}). The temperatures of Al foil and

electrolyte are maintained by a homemade cooling system. After the anodization, square and hexagonal pore arrays with 400 nm spacing are obtained over the whole imprinted area. For the 800 nm spacing imprinted Al, the anodizatin is conducted under a constant voltage of 320 V in a mixture solution (2.5 mL of 1.0 wt% H_3PO_4, 1:1 v/v% of 4.0 wt% citric acid and ethylene glycol) at 15 °C.

3.4 Deposition of Ni film

Nikel (Ni) film deposition was conducted in a Ni plating solution consisting 8.41×10^{-2} M Nikel (II) chloride ($NiCl_2$, Sigma-Aldrich), 1.59 M Nikel sulfamate (II) tetrahydrate ($(Ni(SO_3NH_2)_2\cdot4H_2O$, Sigma-Aldrich), and 0.33 M Boric Acid (H_3BO_3, Sigma-Aldrich). The typical current density for the Ni electrodeposition is 10 mA cm^{-2}. Ni film is deposited with a current density of 1.0 mA cm^{-2} in the same Ni plating solution.

3.5 Electron beam physical vapor deposition

Electron beam physical vapour deposition is a form of physical vapour deposition, in which a targeted anode is bombarded with an electron beam given off by a charged tungsten filament under high vacuum.[81] The electron beam causes atoms from the target to transform into the gaseous phase. These atoms then precipitate into solid form, coating everything in the vacuum chamber (within line of sight) with a thin layer of the anode material. In this dissertation, Ti and Au depositions are performed using Kurt J. Lesker.

3.6 Electroconductivity characterization

3.6.1 X-ray photoelectron spectroscopy

X-ray photoelectron spectroscopy (XPS) is a surface-sensitive quantitative spectroscopic technique to measure the elemental composition at the parts per thousand range, empirical formula, chemical state and electronic state of the elements that exist within a material. [84,87] To obtain the spectra, a material is irradiated with a beam of X-

rays while simultaneously measuring the kinetic energy and number of electrons that escape from the top 0 to 10 nm of the material being analyzed. This requires high vacuum (P ~ 10−8 millibar) or ultra-high vacuum (UHV; P < 10^{-9} millibar) conditions, even though a current area of development is ambient-pressure XPS, where samples are analyzed at pressures of a few tens of millibar. XPS was employed to verify the chemical states of prepared samples in the whole work. All XPS measurements were recorded on a VG MultiLab 2000 system with a monochromatic Al Kα source operated at 300 W.

3.6.2 Field emission scanning electron microscopy

The field-emission scanning electron microscopy is a state-of-the-art electron microscope, which is an analytical method to investigate the morphology of specimen in micro-nanometer regime. The field-emission cathode in the electron gun of microscope provides high electron energy, while as well as narrower probing beam at low, allowing for ultra-high resolution electron imaging (>10 nm at 1 kV) for samples. Even the conductivity of the samples is not good. And it also minimizes the damage of samples. Thus, in this process, the FE-SEM images were almost employed exclusively to investigate the nanostructure morphologies of the prepared samples. All measurements were performed on an ultra-high resolution Hitachi S4800 FE-SEM and Auriga Zeiss FIB at around 5-8 nm working distance with acceleration voltages in the range of 3-15 kV, and a resolution of 1 to 2 nm. Further details on the working principle of a FE-SEM are explicated in literatures.[84,87]

3.6.3 Transmission electron microscopy experiments and methods

Transmission electron microscopy (TEM) is a microscopy technique in which a beam of electrons is transmitted through an ultra-thin specimen (the thickness is less than 200 nm), interacting with the specimen as it passes through. The interaction of electrons transmitted through the specimen formed an image. This image is magnified and focused

onto an imaging device. Owing to the small De-Broglie wavelength of electrons, TEM was capable of imaging at a much higher resolution than FE-SEM (sub-nanometer resolution and even single atom resolution). Therefore, TEM and scanning transmission electron microscopy (STEM) of JEOL JEM-2010F with an acceleration voltage of 200 kV were employed in this work to observe fine details, particularly the crystal structures of the prepared samples. The more details for the work principles of TEM are widely discussed and can be found in literatures. [84] TEM samples were prepared on a Quantifoil R 2/2 TEM grid with a Cu 400 mesh and a 12 nm thick holey carbon film (hole size 2 μm, period 4 μm). The sample with ethanol in vessel was placed into an ultrasonic bath for some minutes. Furthermore, a single drop of the solution is dispersed on a TEM grid and dried at ambient condition.

3.6.4 Energy dispersive X-ray spectroscopy

To study the chemical composition and elements distribution of samples, EDS was utilized [86-87]. EDS system on FE-SEM and TEM detects X-rays emitted from the sample as a result of the high-energy electron beam penetrating into the sample. X-ray spectra can be collected and analyzed, yielding quantitative elemental information about the sample. Most of elements could be detected at concentration on the order of around 0.1 wt%. EDS line scanning and EDS mapping were also performed in this work. The powder XRD were recorded on a Bruker D8 Advance equipped with graphite monochromatized high-intensity Cu Kα radiation (λ = 1.54178 Å). The morphologies were observed with a JEM-2100F TEM operated at an acceleration voltage of 100 kV. High-resolution transmission electron microscopy image and the corresponding selected area electron diffraction (SAED) analyses were attained at an acceleration voltage of 200 kV. The EDX mapping was obtained on S4800 HITACHI (Japan). Room–temperature UV-Vis absorption spectroscopy was measured by Varian Cary 5000 UV-Vis-NIR

spectrophotometer.[94] Ultraviolet photoelectron spectroscopy (UPS) data were obtained on a modified Physical Electronics photoemission system (Kratos Axis UtraDld) which has been incorporated into a custom-built ultrahigh vacuum (UHV) with a base pressure of 3×10^{-8}Torr. A SPECS UVS He I lamp at 21.22 eV was used as UPS source. In transient photoluminescence measurements, the specimens were optically excited by a 420 nm SHG (second harmonic generation) signal from a femtosecond Ti: sapphire laser system, with a repetition rate of 80 MHz. The photoluminescence signal from the sample was collected by a NA=0.42 lens and sent to a 0.75 m focal length spectrometer.[87] Time-integrated photoluminescence was detected by a liquid-nitrogen cooled Si-CCD, while the photoluminescence lifetime was analyzed by an avalanche photodiode together with a time-correlated single-photon counting module.

3.7 Photoelectrochemical characterization

3.7.1 Photocurrent

The photocurrent in this work was characterized by an electrochemical analyzer (*BioLogic SP-200*) under solar light irradiation. The solar light was provided by a solar simulator (*Newport* solar simulator with 300 W Xenon lamp, AM 1.5 global filter). In this work, the simulator provided a controllable indoor test facility under laboratory conditions for testing solar storage and conversion devices. In this process, it is calibrated to 100 $mW \cdot cm^{-2}$ (1 sun condition) by a Si photodiode (*Newport Model 818*). The photocurrents were measured in a standard three-electrode system with prepared samples as the working electrode, a Pt mesh as the counter electrode, and Ag/AgCl as the reference electrode. All three electrodes were placed in a quartz cell. And 0.1 M Na_2SO_4 aqueous solution was used as the electrolyte which was bubbled by high-purity N_2 thoroughly to remove the dissolved oxygen before the measurement.

3.7.2 Incident photo-to-current efficiency

The IPCE is a parameter to evaluate how efficient the device converts the incident light into electrical energy at a given wavelength. The external quantum efficiency and internal quantum efficiency are two types of efficiencies. They are the ratio between the number of collected carriers and the number of all the incident photons on the device active area, or all the absorbed photons by only the active absorber at a given wavelength, respectively. In this work, IPCE was investigated by QEPVSI-b quantum efficiency measurement system from *Newport* without the applying of bias.

3.8 Electrochemical characterization

For electrochemical characterization of photoanode and photocathode for hydrogen evolution reaction, all the measurements were carried out on a *Bio-Logic VSP* electrochemical work station in ambient condition. The three-electrode measurement system was applied during the test period, as indicated in Figure 3.4. A working electrode (prepared samples), counter electrode (1 cm^2 platinum foil) and Ag/AgCl reference electrode (3 M KCl) were included. The specific capacitance, cycle stability and impedance spectroscopy were conducted via this system. The 1.0 M Na_2SO_4 was utilized as electrolyte in testing the performance of photoanode and photovathode. Linear Sweep Voltage or Cyclic Voltammetry was performed at scan rates from 5 to 50 $mV \cdot s^{-1}$. A potential window in the range of −0.5 to 1.2 V was utilized in all measurements of photoanode and photocathode.

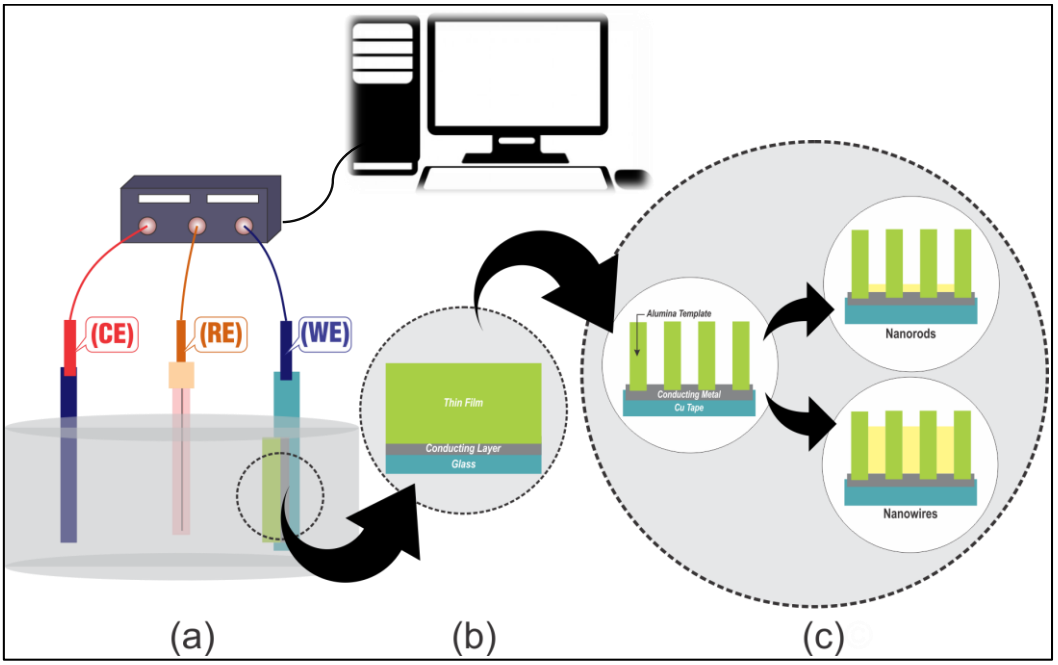

Figure 3.3 (a) The photolectrochemical characterization of photoanode and photocathode for hydrogen evolution reaction, all the measurements are done using an electrochemical work station at ambient condition for thin film (b), and nanostructure (c), respectively.

For the electrocatalytic performance of Pt as counter electrodes, 2 mg of as-prepared catalyst (or commercial Pt/C catalyst (10 wt % loading, Sigma-Aldrich)) was dispersed in 0.98 mL of isopropanol and 20 µL Nafion 117 solution (Sigma-Aldrich). Followed by sonication till well-dispersed ink, and afterward 30 µL of the catalyst ink was spin-coated on 1 cm x 1 cm carbon paper (Toray, Japan), and dried under room temperature. As the working electrode, prepared carbon paper was used. Saturated calomel electrode (SCE) and platinum plate were utilized as reference and counter electrodes, respectively. All potentials in this process were converted to that of reversible hydrogen electrode by RHE calibration explained in literatures.[85,33] In our system, $E_{RHE} = E_{SCE} + 0.272$ V.

Prior to the electrochemical measurement, the electrolyte (0.5 M H_2SO_4) was degassed by bubbling with high-purity N_2 for 30 min. The polarization curves were acquired by sweeping the potential from –0.7 to –0.2 V versus SCE, with a scan rate of 5

to 50 $mV \cdot s^{-1}$. The data were recorded after applying a number of potential sweeps until it was stable. The polarization curves were re-plotted as overpotential (η) versus log current ($log\ J$) to get Tafel plots for assessing of the HER activities of investigated catalysts. The Tafel slope (b) could be obtained by fitting the linear portion of the plots to the Tafel equation ($\eta = b\ log(j) + a$). The accelerated stability tests were carried out in N_2-saturated 0.5 M H_2SO_4 solution at room temperature by potential cycling between −0.7 to –0.2 V versus SCE at a sweep rate of 100 $mV \cdot s^{-1}$ for 1000 cycles. The resulting electrode was used at the end of the cycles for HER polarization and CV curves at a sweep rate of 5 aim 50 $mV \cdot s^{-1}$. All the polarization curves were corrected with iR-compensation.

The capacitance-potential data from the measurement all of samples were analyzed via M-S equation [3.1]:[105,151-153]

$$\frac{1}{C^2} = \frac{2}{\varepsilon_0 \varepsilon e N_A A^2}\left[-V + V_{FB} - \frac{kT}{e}\right] \quad (3.1)$$

where C is the interfacial capacitance (i.e., capacitance of the semiconductor depletion layer), ε is the dielectric constant of compartment, ε_0 is the permittivity of free space ($8.85\times10-12$ F m^{-1}), N_A is the number density (cm^{-3}) of acceptors in photocathode and photoanode. A is the electrode area, V is the bias potential, k is the Boltzmann constant (1.38×10^{-23} J K^{-1}), T is the absolute temperature (298 K) and e is the elementary charge (1.6×10^{-19} C). The intercept (V_0) of a plot of $1/C^2$ versus the bias potential (in the reverse bias regime) on the potential axis affords a value for the flat-band potential, V_{FB} after the small thermal correction, kT/e is made:

$$V_{FB} = V_0 + \frac{kT}{e} \quad (3.2)$$

The carrier concentration, N_A can be obtained from the slope (S) of the M-S plot:

$$N_A = \frac{2}{\varepsilon_0 \varepsilon e S A^2} \quad (3.3)$$

In $BiFeO_3$ photoelectrode case in this dissertation, the dark leakage current J-V characteristic of ferroelectric film was relevant to the top and bottom Schottky barrier height and the Schottky emission can be expressed as[215]:

$$J = A^* T^2 \exp\left(\frac{-q(\phi - \sqrt{\frac{qE_m}{4\pi\varepsilon_\gamma\varepsilon_0}})}{kT}\right) \quad (3.4)$$

where A^*, ϕ, ε_0 and ε_γ, are the effective Richardson constant, potential barrier height, permittivity of free space, and dynamic dielectric constant, respectively. E_m is the maximum electric field at the Schottky interface and equation (2.4) could be transformed as the following to simplify the further analyses:

$$\ln\left(\frac{J}{\tau^2}\right) = \ln(A^*) - \frac{q}{kT}\phi + \frac{q}{kT}\sqrt{\frac{qE_m}{4\pi\varepsilon_\gamma\varepsilon_0}} \quad (3.5)$$

Considering that E_m is proportional to the applied voltage V, vs $V^{1/2}$ plots should be linear at a constant T. Thus, the intercept at V=0 gives the value:

$$\Psi = ln\left(\frac{J}{\tau^2}\right)_{V\to 0} = \ln(A^*) - \frac{q}{kT}\phi \quad (3.6)$$

From equation (2.6), could be obtained easily since is linearly dependent on the 1/T. In addition, the temperature has to be selected above 400 K so that the trapped carriers are sufficiently activated and the current is stable during the measurement.[164] Plotting the Ψ vs 1/T curves, Schottky barrier height at BFO/ITO is obtained as 1.24 eV, in good agreement with the reported values.[178]

3.9 Solar simulator and quantum efficiency measurement system

A solar simulator is a device to provide illumination approximating natural sunlight. The purpose of solar simulator is to accommodate a controllable indoor test facility under

laboratory conditions, applied for the testing of PEC, plastics, sun screen, and other materials and devices.

In this dissertation, Oriel solar simulator (300 W Xe lamp, AM 1.5 global filter) was used as the light source. A Si photodiode (Model 818, Newport) calibrated the simulator to 1 sun (100 mW cm^{-2}). For different wavelength range requirement, optical filters (420 nm and 550 nm cut off) were used in front of AM 1.5G. The IPCE of the devices is measured without applying bias using QEPVSI-b Quantum Efficiency Measurement System (Newport). Chopped illumination (20 Hz) recorded the measurements and no external bias was taken place during the measurements in order to get a pure photocurrent signal. The output current signal was fed to a Merlin digital lock-in radiometry system and the output signal from the lock-in amplifier was connected into a computer held by TRACQ BASIC software.

3.10 Gas chromatography

Hydrogen production was measured under 0.2 V vs RHE with illumination of 100 mW cm^{-2} Xe lamp for the FTO/Au/CBO photoelectrode with Pt nanoparticles. In our case, the water splitting reactor was small in volume and the amount of evolved hydrogen was about μmol scale. The small amount of hydrogen created easiness to dissolve in the electrolyte solution and could not be easily detected by the gas chromatograph equipment. For the FTO/Au/CBO photoelectrode with Pt nanoparticle hydrogen production was measured under 0.2 V vs RHE with illumination of 100 mW cm^{-2} Xe lamp. In our case, the amount of evolved hydrogen was approximately μmol scale, and the water splitting reactor was low in volume. In this low amount, hydrogen was quite easy to dissolve in electrolyte solution and will not be easily detected by gas chromatograph tools.

3.11 Finite-difference time-domain simulation

FDTD solutions is a 3D Maxwell solver which is capable to analyze the interaction of UV, visible, and IR radiation with complicated structures by applying wavelength scale features.[82-84,87-90] FDTD has been acknowledged as the preferred method to conduct electromagnetic simulations for photoelectrochemical cells. In this process, to identify the light utilization of the prepared nanostructure arrays, FDTD was employed to simulate the electromagnetic field distribution and the according photo absorption of simples. It could serve as a support to the experiment results and a consultant to optimize the structure and composition. The parameters of the Cu_2O thin film, $CuBi_2O_4$ thin film, and $CuWO_4$ nanograin arrays were derived from SEM image and a sparse density of Au NPs with the size of 18 nm was used for the simulation.

Chapter 4. p-Type $CuBi_2O_4$: an Easily Accessible Photocathodic Material for High-Efficient Water Splitting

4.1 Introduction

Utilizing earth abundant and easy accessible materials to capture the solar energy and store it in chemical bonds like H_2 has been proven to be a feasible approach to address the current energy challenge.[91] According to electronic properties, the employed active materials could be divided into two types: photoanodic materials and photocathodic materials.[92] Photoanodic materials are usually n-type materials, whose interface with the aqueous electrolyte presents a band-bending beneficial for conducting photo-generated holes to the interface and driving water oxidizing reactions.[91,97–99] Photocathodic materials are always p-type materials and the according band-bending is preferential to generate hydrogen by transferring electrons at the interface.[100-102] So far, most of the efforts on the water splitting has been concentrated on the photoanodic materials, considering that n-type materials are easier to be acquired than p-type materials by low cost accessible procedures.[93] Finding an appropriate photocathodic material is still challenging yet significant, since the photocathode is the PEC electrode that produces hydrogen directly.

Conventional photocathodic materials include p-NiO,[103-104] p-Cu_2O,[100,105-106] p-GaP,[102,107] etc, yet these materials either have an inappropriate band gap structure for solar energy absorption or prone to corrosion in the applicable solution, and thus it is highly required to pursuit a suitable material for water splitting. Alternatively, p-type $CuBi_2O_4$ (CBO) possesses a band gap value from 1.5 to 1.8 eV,[109-110] which could be the right one in water splitting application. Moreover,

CBO could also be used for the oxidation of Acetaldehyde into CO_2 by constructing hetero junction with WO_3 and other environmental applications.[110–112] Though a few efforts tha have been made to employ such material in PEC research, photocurrent is still as low as 100-200 μA cm^{-a} for the bare CBO photocathode without using catalysts probably owing to the poor crystal quality of the CBO films.[108,113-114] To improve PEC performance, other efforts, including incorporating metals to the material,[122] forming hetero junction with CuO,[109] using PEC promoting catalyst,[123] have been made. The resulting efficiencies seem still far from the usage of industrial applications. To be noted, n-type $CuBi_2O_4$ has also been reported[110]and thus more details about understanding the band gap structures of CBO are still needed.

In this section, the CBO photocathodes were fabricated based on FTO and FTO/Au substrates, respectively. To be noted, the later showed an outstanding PEC performance as compared with the former. The subsequent characterizations revealed that the presence of Au layer could be beneficial for improving the crystal quality and electronic properties of the relevant material. After optimizing the structure of the photocathodes by depositing Pt nanoparticles on the surface, the photocurrent was a meliorated as high as −1.24 mA cm^{-I}. Therefore, this section provides a promising candidate to the family of photocathodic materials.

4.1 Experimental section

4.1.1 Materials and Chemicals

$Bi(NO_3)_3{\cdot}5H_2O$ (≥98.00%), $Cu(NO_3)_2{\cdot}3H_2O$ (≥99.1%), soldiumsulfate (≥99.0%), nitric acid (≥98%), acetone (≥99.8%), ethanol (≥95%), FTO-coated glass (Product Number: 735213; L×W×D: 100mm×100mm×3mm; Surface resistivity:~10 Ω/sq; Transmittance: ≥83.0% (visible)) were used as received from

Sigma-Aldrich. Insulating epoxy (EA 3450) was purchased from Loctite. Copper tape (AT528) was purchased from Advance Tapes.

4.2.2 Preparation of the CBO films

First, FTO glass was cleaned with acetone, ethanol and DI water, respectively. Then, a thin layer of Au was deposited on the cleaned and dried FTO glass as the substrate via a physical vapour deposition (Kurt J. Lesker) procedure with the rate of 0.2 Å s^{-1}. Subsequently, CBO thin films were cathodically electrodeposited from a bath solution of 8 mM $Bi(NO_3)_3 \cdot 5H_2O$ and 4 mM $Cu(NO_3)_2 \cdot 3H_2O$ in 10% nitric acid. Nitric acid was purposely used to dissolve bismuth nitrate precursor. The pH value of the bath was carefully adjusted to 12.0 by the addition of 3 M sodium hydroxide. Films were grown at a constant potential of −0.40 V vs Ag/AgCl in a normal three-electrode configuration for a nominal duration of 30 min. The temperature of the bath was controlled at 45 °C using a heating plate with an in situ temperature probe. After deposition, the samples were rinsed with DI water and dried in an air stream. A final annealing procedure at 550 °C for 120 min in air was performed to achieve better crystallinity. For comparison, we also prepared CBO thin films on FTO glass directly using the same procedure.

4.2.3 Fabrication of CBO photocathodes

A strip of conductive copper tape was stuck on the exposed FTO part of the FTO/Au/CBO and FTO/CBO to extend the conducting circuit and threaded through a glass tube and then sealed with an insulating epoxy. Electrode areas were optically measured as 0.2 cm^2.

4.2.4 Deposition of Pt nanoparticles

Pt nanoparticles on CBO was performed on PicosunSunale R150 ALD reactor with low-nitrogen-filling ALD process as we previously reported.[117] The

precursors used for Pt growth weretrimethyl (methyl cyclopentadienyl) platinum(IV) ($Pt(MeCp)Me_3$) (Sigma Aldrich) and O_2. The temperature of Pt precursor was held at 80°C. The substrate temperature was controlled at 220°C. And the typical ALD cycle consisted of $Pt(MeCp)Me_3$ pulsing (1.0 s)-lowN_2 filling (60 s)-N_2purging (30 s)-O_2 pulsing (1.0 s)-low N_2filling(30 s)-N_2purging (30 s).

4.2.5 Photoelectrochemical measurements

External quantum yield was measured with an Oriel 150 W Xe arc lamp (Newport) and a quarter-turn single-grating monochromator (Newport). Sample measurements were recorded with chopped illumination. The output current signal was connected to a Merlin digital lock-in radiometry system and the output signal from the lock–in amplifier was fed into a computer controlled by TRACQ BASIC software. Current–potential plots and impedance characterization were measured by using the digital BioLogic potentiostat (SP-200) and 0.1 M sodium sulphate aqueous solution served as the electrolyte. A Pt counter electrode and Ag/AgCl reference electrode were used during the measurements. A standard 300 W Xe lamp (Newport) served as the light source and the light intensity was characterized to 100 mW cm^{-E} by a Si photodiode (Newport). The evolution of hydrogen gas during the water splitting reaction was measured by the gas chromatography-mass spectrometer (GC-2010 plus).

4.2.6 Characterizations

The powder XRD was recorded on a Bruker D8 Advance equipped with graphite monochromatized high-intensity Cu Kα radiation (λ = 1.54178 Å). The morphologies were observed with a JEM-2100F transmission electron microscopy operated at an acceleration voltage of 100 kV. HRTEM image and the corresponding selected area electron diffraction analyses were attained at an

acceleration voltage of 200 kV. The EDX mapping was obtained on S4800 HITACHI (Japan). Room–temperature UV-Vis absorption spectroscopy was measured by Varian Cary 5000 UV-Vis-NIR spectrophotometer. The UPS data were obtained on a modified Physical Electronics photoemission system (Kratos Axis UtraDld) which has been incorporated into a custom-built ultrahigh vacuum (UHV) with a base pressure of 3 X 10^{-8}Torr. A SPECS UVS He I lamp at 21.22 eV was used as UPS source. In transient photoluminescence measurements, the specimens were optically excited by a 420 nm SHG (second harmonic generation) signal from a femtosecond Ti: sapphire laser system, with a repetition rate of 80 MHz. The photoluminescence signal from the sample was collected by a NA=0.42 lens and sent to a 0.75 m focal length spectrometer. Time-integrated photoluminescence was detected by a liquid-nitrogen cooled Si-CCD, while the photoluminescence lifetime was analyzed by an avalanche photodiode together with a time-correlated single-photon counting module.

4.3 Results and discussion

The CBO thin films was synthesized via an electrochemical approach in combination with annealing treatment.[108]Figure 4.1a1 evidences SEM image of CBO film prepared on FTO glass directly. The film was constructed by a series of nanoparticles and the profile of these nanoparticles looks irregular and blurry. The TEM image of a representative particle detached from the FTO/CBO sample is given in Figure 4.1a2, where an irregular profile of the as-grown particle could be clearly observed. Figure 4.1a3 indicates HRTEM image of the particle. The crystal lattice appears hazy, attributing to the low crystalline quality of the sample. The

average distance between the adjacent lattice planes as 0.3 nm could still be estimated, corresponding to (211) planes of the materials.[109]

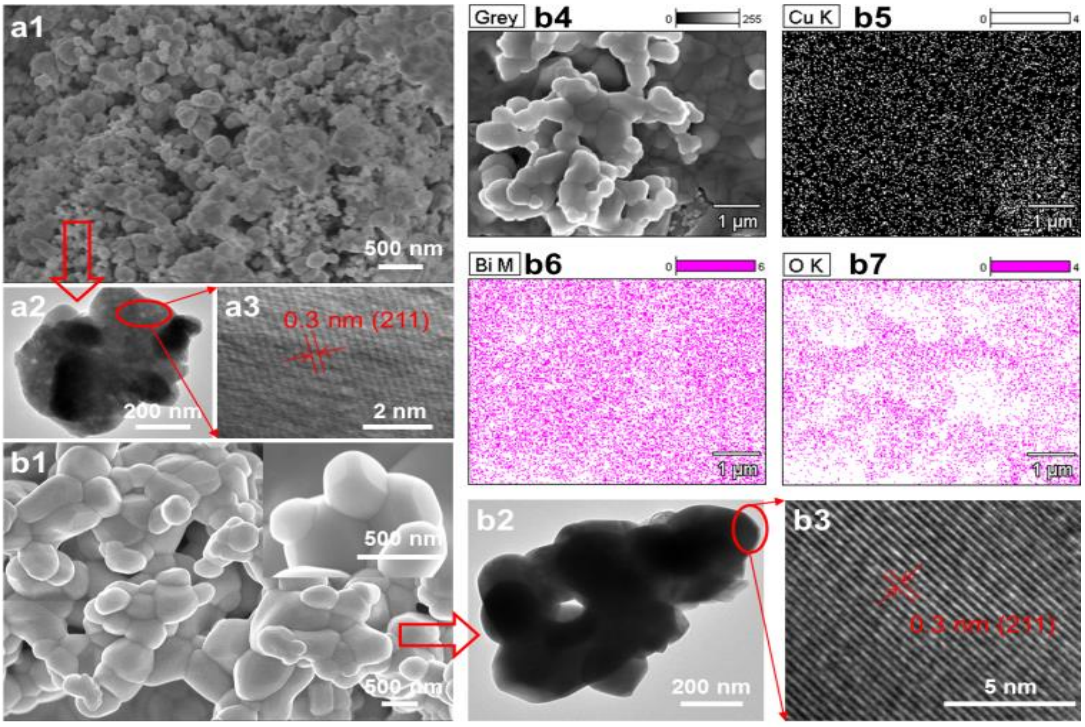

Figure 4.1 Characterizations of CBO films. (a1, b1) top view SEM images, (a2, b2) TEM images and (a3, b3) HRTEM images of CBO films grown on FTO (a) and FTO/Au (b). (b4) SEM image of CBO films on FTO/Au, and corresponding EDX mapping image for (b5) Cu element, (b6) Bi element and (b7) O element.

For the films grown on FTO/Au as shown in Figure 4.1b, the composed nanoparticles surprisingly look neat and each particle presents a polyhedral feature, indicating an improved crystalline quality in comparison with the films grown on FTO glass. Such polyhedral morphology could be superior over other morphologies in catalytic effect, like the case in Cu_2O.[108] To support such noticeable observation, the polyhedral particles were particularly characterized by TEM, as shown in Figure 4.1b2. The profile of these particles is in agreement with that measured by SEM. HRTEM image in Figure 4.1b3 illustrates a much better

crystalline quality for the CBO on FTO/Au than that on FTO only, indicating the superiority of electrochemically growing CBO film on FTO/Au substrates. For further confirming the chemical composition of the prepared film CBO on FTO/Au, EDX mapping obtained from a representative particle (shown in Figure 4.1b4) was particularly measured and the relevant images are shown in Figure 4.1b(5-7), from which signals from Cu, O and Bi were obtained. Appendix Figure 11.1a presents EDX mapping of CBO on FTO. To investigate the influence of Au on the formation of CBO, EDX measurements on the particles detached from FTO/Au/CBO and FTO/CBO were performed, respectively. The relevant spectra are given in Appendix Figure 11.1b and 1c. In comparison with the spectrum from FTO/CBO, the spectrum of the particles from FTO/Au/CBO does not show the indication in containing Au in the crystals. This implies that Au could not enter the crystal lattices of CBO as the doping element. The reason of the improved crystal quality could probably be the Au thin film that can supply a uniform distributed electric field, a lower resistance and an activation energy for the electrochemical deposition.

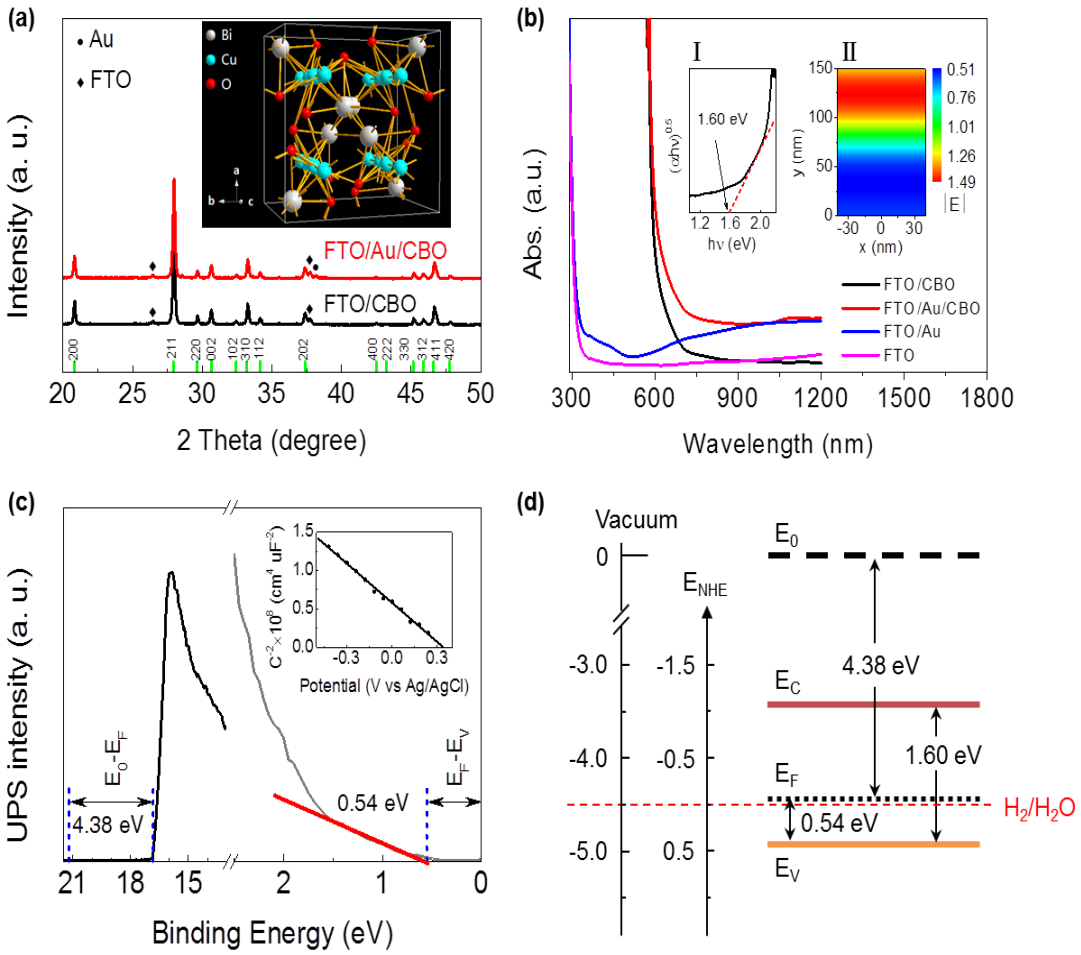

Figure 4.2 (a) XRD patterns of the two samples. (b) UV-Vis absorption spectra obtained from the CBO films and substrates (Inset Ⅰ: plot of $(\alpha h\nu)^{1/2}$ vs hν for estimating the band gap value of the film. Inset Ⅱ: spatial distribution of the electric field intensity across the FTO/Au illuminated by the photons at 800 nm. (c) UPS cut off spectra of CBO films. Left panel is the work function and right panel is the valence band region, respectively. (d) Schematic energy diagram of CBO deduced by the UPS data in c. A favorable energy level makes CBO as an ideal material for water splitting.

Figure 4.2 (a) presents the XRD patterns of these two films, where a series of diffraction peaks attributed to Kusachiite CBO phase could be clearly observed (PDF#48-1886), though the peaks of Au and FTO are unavoidable. The highest

diffraction peak belongs to the (211) facet. To describe it more visually, we present the crystal structure of CBO, as shown in the inset. The black curve in Figure 4.2 (b) indicates the absorbance spectrum of the prepared CBO on FTO substrate, which presents a broad absorption range with a threshold from 760 nm and indicates a good capability in the absorption of solar energy. To attain the optical band gap value, we plotted the curve for $(ah\nu)^{1/2}$ vs $h\nu$ as shown in the inset I. Such Tauc plot indicates a band gap value of 1.60 eV, close to the reported values.[28] This value enables the relevant material as a promising candidate in water splitting applications. For comparison, we present the absorbance spectrum of FTO/Au/CBO, as shown by the red curve in Figure 4.2 (b). Beyond the absorption range of CBO, FTO/Au/$CuBi_2O_4$ exhibits a distinct absorption capability as compared with the sample based on FTO/CBO. This could be originated from presence of Au films. As shown by the blue curve, FTO/Au possesses a clear absorption in the range of 500-1200 nm by comparing with the spectrum from FTO (the pink curve). In addition, the intensity of the blue curve quantitatively matches the intensity difference of the red curve and black curve, indicating that the presence of Au thin films also contributes to the absorption of FTO/Au/CBO. The well-known SPR effect of Au is responsible for such absorption and the large localized electric field at the surface of Au, which was simulated by FDTD Solutions and shown as the inset Ⅱ, could also promote the light absorption via band gap transitions and near band gap transitions of CBO via PRET, scattering and anti-reflection effects.[120] The corresponding simulated absorbance of FTO/Au is shown in Appendix Figure 11.2 which is in good agreement with the measured spectrum. In Appendix Figure 11.3 presents the Raman spectra of the FTO/CBO and FTO/Au/CBO and both spectra possess a

series of vibrational peaks that match the standard CBO peaks from the reported reference.[121] FTO/Au/CBO has a higher intensity than FTO/CBO, attributing to the SPR effect of Au.

To acquire more information of the band gap structure of the grown CBO films, UPS measurement was performed to determine the energy levels of the relevant material. Figure 4.2 (c) presents the standard UPS data for the CBO films. The work function that is defined as the difference of the vacuum energy level and Fermi level could be derived from the low kinetic energy cut-offs in the secondary emission features. Given that the Fermi level at the surface of CBO is considered independently, the work function is measured as $21.22 - 16.65 = 4.38$ eV with 21.22 eV being the photon energy of UV source (He I discharge). The valence band position with respect to the position of Fermi level was determined by the linear portion of the low binding energy side of the proper valence band peak to the energy axis ($E_V - E_F = 0.74$ eV) and the according value vs the vacuum energy level is attained as $4.38 + 0.74 = 5.12$ eV. In addition to the band gap values obtained from the Tauc plot, the exact band gap structure of the grown CBO films could be depicted, as shown in Figure 4.2 (d). By referring the standard reduction and oxidation potentials of water, these potentials are just in between the valence band position and conduction band position of CBO, thereby making it as an ideal material for water splitting. In addition, the short distance of Fermi level to the valence band position indicates a p-type feature of the as-grown CBO. The inset in Figure 4.2 (c) presents a standard Mott-Schottky plot of the PEC electrode based on FTO/CBO. The linear profile and the negative slope yield a typical p-type feature of the prepared material, in consistence with the UPS analysis. The band gap value estimated herein is a little lower than that from reported values which

could be attributed to the defects in the material.[122] The energy level positions are determined in a vacuum condition with surface defects removed by ion milling procedures. This causes the difference from the band gap positons measured by the electrochemical technique.

Figure 4.3 (a) exhibits representative current density-potential curves from standard photoelectrochemical measurements, performed in a 0.1 M $NaSO_4$ aqueous solution (pH = 6.8) with CBO photocathode as the working electrode, Pt plate as the counter electrode and Ag/AgCl as the reference electrode. To make the curve fit for the water splitting analysis, the reference potential from Ag/AgCl to the reversible hydrogen electrode (RHE) were converted by the following Nernst equation：

$$E_{RHE} = E_{Ag/AgCl} + E°_{Ag/AgCl} + 0.059\ V \times pH \quad (4.1)$$

Where E_{RHE} is the converted potential versus RHE, $E_{Ag/AgCl}$ is the external potential measured against the Ag/AgCl reference electrode, and $E°_{Ag/AgCl}$ is the standard potential of Ag/AgCl at 25°C (0.1976 V).

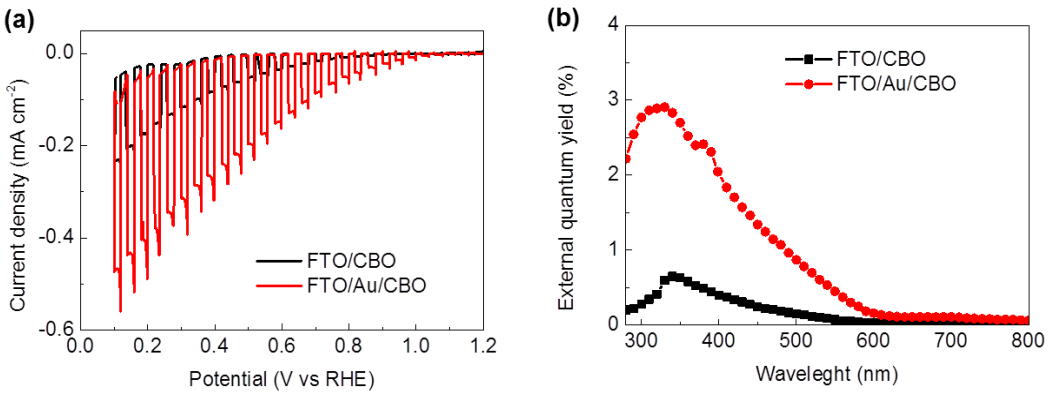

Figure 4.3 Photoelectrochemical performance of CBO films photocathodes. (a) Current density–potential characteristics in 0.1 MNa_2SO_4 solution, under chopped AM1.5 light illumination for the electrodes of CBO films grown on FTO and FTO/Au. (b)

Wavelength-dependent external quantum yield spectra of two samples, the spectra were measured in a two-electrode configuration without any external bias.

For the photocathode based on FTO substrates, photocurrent was attained more than −0.2 mA cm^{-2}, which is almost the highest value for the pure CBO photoelectrode.[108-109,115,119] The photocathode on the basis of FTO/Au substrates presents an even higher photocurrent than the PEC electrode based on FTO glass. The photocurrent for FTO/Au/CBO is realized as high as −0.5 mA cm^{-2}, being more than two folds higher than that from the electrode without Au films. In addition, both curves have an open circuit potential close to 1 V vs RHE which could make the water reducing reactions occur without external bias.[93] Figure 4.3 (b) shows the EQY spectra of the two relevant photocathodes. Both of the spectra have an EQY onset from 600 nm and the profiles of these spectra match the profiles of the according absorbance spectra, indicating that the photocurrent is from the charges generated in CBO. In consistence with analysis on J−V curves, the photocathode based on FTO/Au possesses a higher EQY value than the electrode based on FTO. These data points out that the CBO films prepared on FTO/Au is superior over the films grown on FTO. To investigate it more deeply, a series of systematical characterizations were carried out.

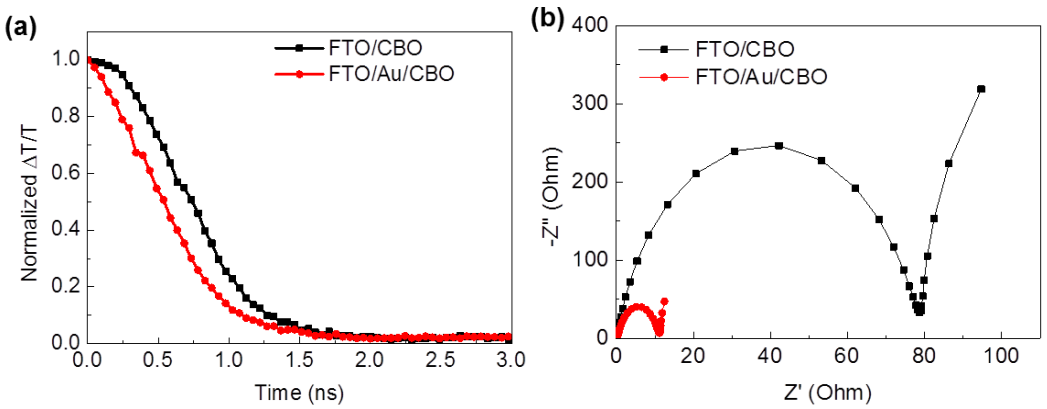

Figure 4.4 (a) Time-resolved photoluminescence decay curves (excitation: 450 nm) and (b) Nyquist plots of CBO photocathodes with/without Au thin layer.

Transient photoluminescence decays for the two sets of photocathodes were measured by the excitation at 450 nm. As shown in Figure 4.4 (a), the PEC electrode made by FTO/Au/CBO presents a faster PL decay by comparing with the sample based on FTO/CBO. Using the customarily single exponential model, transient PL lifetimes of the relevant CBO films are acquired as 0.54 ns and 0.68 ns, respectively. The promoted PL decay for the CBO electrode on FTO/Au suggests an efficient separation for photo-generated charges, which is helpful for the water splitting applications. The physical reason could be attributed to the better crystal quality of the CBO on FTO/Au, for which the low density of defects would provide an efficient route for charge dissociation.

Nyquist plots measured in the frequency range of 10^5 Hz - 1 Hz at the bias of 0.2 vs RHE for the two sets of PEC electrodes are shown in Figure 4.4 (b). Given that the semicircle in a Nyquist plot at high frequencies is characteristic of the charge transfer process and the diameter of the semicircle is estimated to be equal to the charge transfer resistance,[106,123] the charge transfer resistance of the system is prominently decreased by the usage of Au thin layer. The reduced charge transfer

resistance, which should result from the high conductivity of Au film and the high crystal quality of CBO on FTO/Au, indicates a higher utilizing efficiency of photo-generated charges in the system of FTO/Au/CBO.

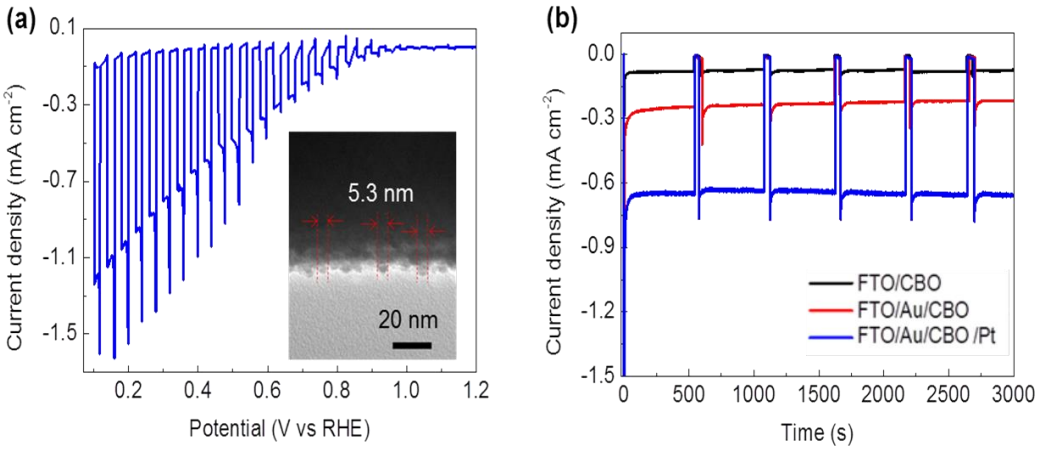

Figure 4.5 (a) Current density–potential curve of FTO/Au/CBO device with Pt nanoparticles under chopped AM1.5 light illumination, the inset shows TEM of Pt nanoparticles on the surface of CBO. (b)Curves of the time-dependent photocurrent measured for the FTO/CBO and FTO/Au/CBO photoelectrode without/with Pt nanoparticles at 0.4 V vs RHE under AM1.5G light illumination.

To promote the PEC performance of the FTO/Au/CBO device, Pt nanoparticles were deposited on the film surface as the catalyst via an atomic layer deposition procedure. The inset of Figure 4.5a shows the TEM image of the prepared catalyst on CBO, where the size of the particles could be gauged as 5.3 nm. The J-V curve of the advanced photocathode is provided in Figure 4.5 (a). By comparing with the bare electrodes, the one equipped with Pt catalyst has a positive shifted open circuit potential with a value close to 1.1 V vs RHE. The plateau photocurrent is amplified to -1.2 mA cm^{-2} by modifying the FTO/Au/CBO surface with Pt nanoparticles, and the photocathode with Pt catalyst also has a higher EQY value than the one

without Pt nanoparticles (see Figure Appendix 11.4), thus showing a great potential of applying CBO in water reduction. The evolution of hydrogen gas during the water splitting reaction was measured by gas chromatography-mass spectrometer (GC-2010 plus) and the result is shown in Figure Appendix 11.5. The Faradic efficiency was calculated as 84.49% for the water splitting reactor during 80 min.

Though it is well reported that Cu_2O has long been considered as an ideal p-type material for water reduction, such material is prone to corrosion when soaked in the aqueous solution for PEC measurements.[100] To investigate the stability of the CBO PEC system, the photocurrent at fixed potential was measured and the transient curves are shown in Figure 4.5 (b). At the initial stage after the illumination is on, the photocurrents show a fast decaying feature, which is normal for the PEC system. After 50 s, however, these photocurrents for the three sets of electrodes, FTO/CBO, FTO/Au/CBO and FTO/Au/CBO/Pt, are quite stable even the measuring time is prolonged over 3000 s. Furthermore, the FTO/CBO before and after PEC measurement was investigated by SEM (see Appendix Figure 11.6), which shows that the structure of materials has no changed after PEC. These results suggest that as-grown CBO possesses a good property in PEC stability, making it advantageous in comparison with Cu_2O.[100] Osterloh has reported a valuable experiment by dissolving the prepared p-type CBO nanoparticles into the KI contained solution and investigating hydrogen evolution.[122] A H_2 generation rate of 16 μmol h^{-1} was realized, though the system showed rate deterioration after working for 6 h. In our system, due to the using of neutral solution without any other redox couples, we did not find the deterioration. This indicates that a

systematic work on the stability of CBO towards pH values and redox couples of the electrolyte is still needed in future.

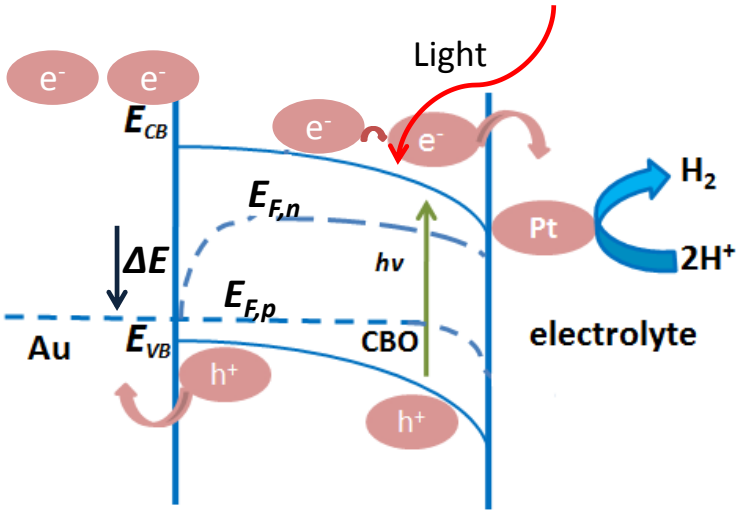

Figure 4.6 Schematic energy alignment illustrating the paths of charge carrier in Au/CBO/Pt/electrolyte under solar light irradiation.

It should be mentioned that the contact of Au with CBO plays a key role in our advantageous PEC performance. The work function of Au is 5.2 eV vs vacuum and the Fermi level of CBO is measured as 4.38 eV vs vacuum. The photocathode is represented by difference of quasi-Fermi level of electron ($E_{F,n}$) in Figure 4.6 and hole ($E_{F,p}$), yielding the achievable free energy of the system near maximum power point and state must exist at proper energy in electrolyte for injection of carrier; the redox potential related to the CBO band so that the donor level exist in electrolyte at an energy equal to or above the valance band edge and hole quasi-Fermi level. Which is, these results in a downward band bending (from Au to CBO) that is preferential for the collection of photo-excited holes by FTO/Au and promoting the transfer of electrons to the interface with electrolyte to drive PEC reactions. Thus, an accelerated PL decay rate and a reduction of the resistance of the system have been observed. Pt nanoparticles on CBO surface behave as the efficient catalysts

for hydrogen generation by providing a large amount of site for absorbing the reactants and reducing the PEC reaction potentials. The energy alignment is given in Figure 4.6.

Chapter 5. Facile Surface Treatment on Cu_2O Photocathodes for Enhancing the Photoelectrochemical Response

5.1 Introduction

Harvesting solar energy and storing it in chemical bonds, particularly in the simplest chemical bond like H_2, could be a highly feasible approach to solve world-wide energy challenge. While p-type Cu_2O has long been considered as an attractive candidate for water splitting due to the favourable band gap position and high abundance of elements,[99,124–125] concomitant surface defects like reconstructions, uncoordinated atoms and even the CuO or Cu phases generated in the synthesizing or measuring procedures, adversely impact the device efficiency and stability.[126,127] Specifically, the presence of Cu(II) or Cu(0) sites on the surface severely deteriorates the device performance and it is highly required to prepare Cu_2O photocathode with high crystal quality to avoid the formation of such surface impurities.[128,129] An advantageous approach for electrodepositing Cu_2O is depositing the material on FTO/Au substrates rather than on FTO or FTO/Cu substrates. The existence of Au thin film helps to improve the crystal quality and performance reproducibility for the grown Cu_2O film.[124,130] Even in this case, the electronic properties of the resulting material could not be optimized for the PEC performance.

While the utilization of thin oxide layers can protect Cu_2O from corrosion during measurements,[124,127] it is still difficult to change electronic properties of Cu_2O only by using post-solid-state treatment. Herein, we report an effective surface treatment method for attaining a high PEC performance on Cu_2O based photocathodes. Surface treatment was conducted by soaking the as-grown films in a TSC aqueous solution and the subsequent electrochemical characterizations illustrated that the doping level of the Cu_2O

films was impressively enhanced along with an enlarged band bending at the interface of Cu_2O/electrolyte. Accordingly, the photocurrent of the corresponding PEC electrodes with the subsequent protection layer (TiO_2/Pt) was ameliorated around two times. Aspects relevant to the charge transfer dynamics were particularly investigated by transient photoluminescence spectroscopy.

5.2. Experimental

5.2.1. Preparation of the Cu_2O films

First, FTO glass was cleaned with acetone, ethanol and DI water, respectively. Then, a thin layer of Au (25 nm) was deposited on the cleaned and dried FTO glass as the substrate via a physical vapour deposition procedure. Subsequently, Cu_2O thin films were cathodically electrodeposited from a 0.4 M copper sulphate bath containing 3 M lactic acid. The pH value of the bath was carefully adjusted to 12.0 by the addition of 3 M sodium hydroxide. Films were grown at a constant potential of −0.40 V vs Ag/AgCl in a normal three-electrode configuration for a nominal duration of 30 min. The temperature of the bath was controlled at 45°C using a heating plate with an in situ temperature probe. For comparison, we also prepared Cu_2O thin films on FTO glass directly using the same procedure. Finally, the prepared Cu_2O films were purposely soaked in an aqueous solution containing 1 M TSC for 30 min and dried by N_2.

5.2.2. Deposition of TiO_2 and Pt nanoparticles

The samples were put in an atomic layer deposition (PicosunSunale R150) chamber for depositing the protection layer of TiO_2 and Pt catalyst. Titanium dioxide was deposited using titanium (IV) chloride ($TiCl_4$), and distilled-water (H_2O) as the Ti and O precursors, respectively. The TiO_2 deposition was then carried out at 200 °C and one typical cycle consists of: $TiCl_4$-N_2 purge-H_2O-N_2 purge (1 cycle). The growth rate of

TiO_2 is about 0.6 nm per cycle. Deposition of Pt nanoparticles was performed on the reactor with low-nitrogen-filling ALD process as we previously reported.[9] The precursors used for Pt growth were trimethyl (methyl cyclopentadienyl) platinum (IV) ($Pt(MeCp)Me_3$) and O_2. The temperature of Pt precursor was held at 80 °C. The substrate temperature was controlled at 220 °C. And the typical ALD cycle consisted of $Pt(MeCp)Me_3$ pulsing (1.0 s)-low N_2 filling (60 s)-N_2 purging (30 s)-O_2 pulsing (1.0 s)-low N_2 filling (30 s)-N_2 purging (30 s).

5.2.3. Fabrication of Cu_2O photocathodes

A strip of conductive copper tape was stuck on the exposed FTO part of the specimens to extend the conducting circuit and threaded through a glass tube and then sealed with an insulating epoxy. Electrode areas were optically measured as 0.2 cm^2.

5.2.4. Photoelectrochemical measurements

EQY was measured with an Oriel 150 W Xe arc lamp (Newport) and a quarter-turn single-grating monochromator (Newport). Sample measurements were recorded with chopped illumination. The output current signal was connected to a Merlin digital lock-in radiometry system and the output signal from the lock-in amplifier was fed into a computer controlled by TRACQ BASIC software. Current-potential plots and impedance characterization were measured using the digital BioLogicpotentiostat (SP-200) and 0.1 M sodium sulphate aqueous solution served as the electrolyte. A Pt counter electrode and Ag/AgCl reference electrode were used during the measurements. A standard 300 W Xe lamp (Newport) served as the light source and the light intensity was characterized to 100 mW cm^{-2} by a Si photodiode (Newport).

5.2.5. Characterizations

XRD pattern was recorded on Bruker D8 Advance equipped with graphite monochromatized high-intensity Cu Kα radiation (λ = 1.54178 Å). The SEM images were obtained by S4800 HITACHI (Japan) scanning electron microscope. Room-temperature UV-Vis absorption spectroscopy was measured using Varian Cary 5000 UV-Vis-NIR spectrophotometer. XPS experiments were carried out on an Axis Ultra DLD system (Shimadzu) using Al Kα radiation (*hv*=1486.6 eV). The whole spectra (0-1200 eV) and the narrow spectra of all the elements with high resolution were both recorded by using the RBD 147 interface (RBD Enterprises, USA) through the Auger Scan 3.21 software. Binding energies were calibrated by using the containment carbon (C1s=284.6 eV). FTIR spectra were recorded at room temperature using FTS-60V FTIR spectrophotometer. In transient photoluminescence measurements, the specimens were optically excited by a 420 nm SHG (second harmonic generation) signal from a femtosecond Ti: sapphire laser system, with a repetition rate of 80 MHz. The photoluminescence signal from the sample was collected by a NA=0.42 lens and sent to a 0.75 m focal length spectrometer. Time-integrated photoluminescence was detected by a liquid-nitrogen cooled Si-CCD, while the photoluminescence lifetime was analysed by an avalanche photodiode together with a time-correlated single-photon counting module.

5.3. Results and discussion

The electrodeposition for Cu_2O was performed in a copper sulphate bath containing 3 M lactic acid. The bath pH value was carefully adjusted to 12.0 by precisely controlled addition of 3 M NaOH. Herein, the use of pH buffer was intentionally avoided to preclude interferences from the buffer components with the interfacial behaviour. The deposition potential was set as −0.40 V vs Ag/AgCl according to the cyclic voltammetry test shown in Appendix Figure 11.7, where the reduction peak of Cu^{2+} to Cu^{+} at −0.40 V

vs Ag/AgCl could be clearly observed. Figure 5.1a portrays the representative SEM images of the prepared films on FTO/Au substrates. The films are constructed by continuously distributing polyhedral particles. The size of these particles is gauged as 1−3 μm. For the films grown on FTO glass, however, the size of the composed particles becomes bigger and the configuration turns out to be cuboid, as demonstrated in Figure 5.1b. Though it is well reported that the morphology of Cu_2O nanoparticles can be determined by the pH values, surface ligands and profiles of the growing seeds,[142,143] these data point out that the morphology could also be influenced by the choice of depositing substrates, which contributes another factor to manipulate the morphology of the Cu_2O nanoparticles. The XRD pattern of the Cu_2O films is given in Figure 5.1c, where the diffraction peaks at 29.6^o, 36.5^o, 42.4^o, 61.4^o and 73.6^o can be doubtlessly ascribed to the diffraction of (110), (111), (200), (220) and (311) planes of Cu_2O (JCPDS card No. 05-0667).[126] The crystalline structure is depicted as the inset of Figure 5.1c. Diffraction peaks of CuO and Cu are not discernible, implying a pure Cu_2O structure in the films. In addition, being consistent with the reported values,[134–136] the band gap of the synthesized Cu_2O is characterized as 2.09 eV by the absorption analyses shown in Figure 5.1d and inset I. Such suitable value qualifies the resultant as a good material in solar energy conversion. The absorption spectrum of Au thin film that exhibits a slight absorption capability in the range of 400-800 nm is also presented. To investigate the absorption capability of the photocathodes furthermore, finite difference time domain (FDTD) simulation was performed for the structure, FTO/Au/Cu_2O. Inset II in Figure 5.1d shows the relevant spatial distribution of the electric field intensity across the structure illuminated by the photons at 500 nm and the polyhedral feature of the particles in the film strengthens the absorption efficiency by the scattering effect. Appendix Figure 11.8 shows the calculated absorption efficiency in accordance with the thickness of Cu_2O

on FTO/Au. As we tune the thickness from 500 nm to 2000 nm, the absorption efficiencies show a close value below 500 nm, due to the high absorption coefficient of Cu_2O. In the longer wavelength region, the thickness begins to impact the absorption by increasing the intensity and the interference effect attributing to the surface nanostructure could also be influential.

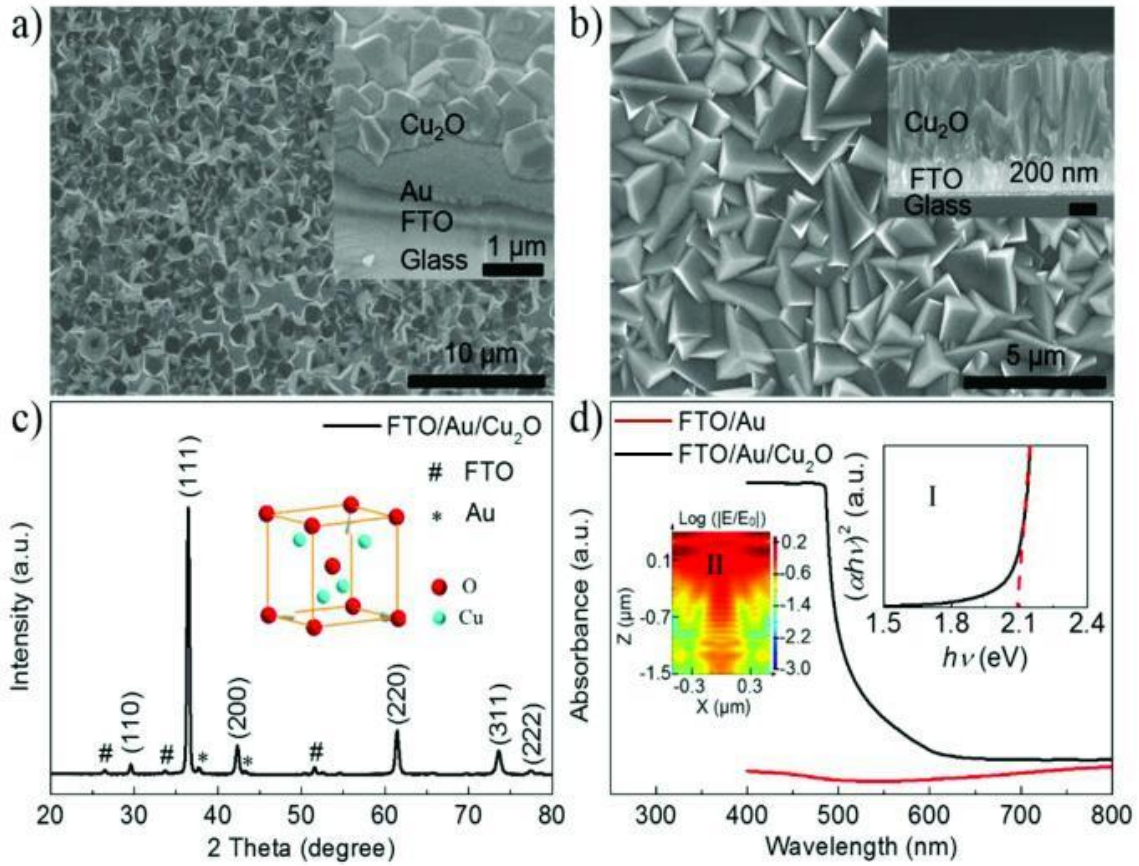

Figure 5.1 a,b) SEM images of the prepared Cu_2O films on FTO/Au and FTO substrates, the insets show the cross-sectional SEM images. c) XRD pattern of the Cu_2O films on FTO/Au substrates. The inset presents the crystal structure of the material. d) Absorption spectroscopic measurements of the samples. Inset I: plot of $(\alpha h\nu)^2$ vs $h\nu$ for estimating the band gap value of the film. Inset II: spatial distribution of the electric field intensity across the photocathodes illuminated by the photons at 500 nm.

Though XRD pattern of the prepared Cu_2O films presents a pure Cu_2O phase, it is still hard to exclude the existence of Cu (II) and Cu (0) impurities on the surface. To characterize it more convincingly, XPS was specifically studied. As shown in Figure 5.2a, the Cu 2p peaks are resolved and the main peaks at 932.5 and 952.6 eV correspond to the Cu $2p_{3/2}$ and Cu $2p_{1/2}$, respectively, assigning to the Cu^+.[128,139] In the Cu 2p spectrum, Cu^{2+} is identified by the emergence of a main signal at 933.6 eV along with a series of shakeup satellites between 932.5 and 952.6 eV.[138] For the sample without any surface treatments, the satellite peaks are quite prominent and only slightly lower than the Cu $2p_{1/2}$ peak, being indicative of the presence of Cu^{2+} on the surface. These shakeup satellite peaks are characteristic of Cu^{2+} that has a partially filled Cu $3d^9$ shell configuration in the ground state,[126,139] which usually deteriorates p-type feature of Cu_2O.

To fix the Cu^{2+} related impurities on the prepared Cu_2O films and to stabilize the photocathodes, a post-solid-state surface treatment was carried out by soaking the Cu_2O films in a 1 M TSC aqueous solution for 30 minute. TSC that is well known as the chelating agent in the synthesis of Cu_2O nanoparticles could help to avoid the formation of $Cu(OH)_2$ and CuO in the reducing reactions of Cu^{2+}.[133,140] In addition, the reducing capability of TSC could also probably influence the Cu $3d^9$ shell configuration by making it more filled. As displayed in Figure 5.2a, after surface treatment, the two main peaks become much more outstanding as compared with the peaks from the same films without surface treatment. To be highlighted, the satellite peaks turn out to be ignorable, indicative of the feasibility for this peculiar treatment. The absence of sharp satellite features for Cu_2O is rationalized on the basis of a full Cu $3d^{10}$ shell that inhibits screening via charge transfer involving d states.[126] Figure 5.2b exhibits the O 1s spectra of the sample before and after the surface treating procedure. The main peak signal at 530.5 eV is a clear oxygen signature associated with Cu_2O[126] and the treatment in TSC solution is

beneficial for eliminating the impurity peaks around O 1s main peak, yielding an efficient platform for charge transfer. Regarding the C 1s spectra given in Figure 5.2c, the peaks for C=C-C and O=C-O [141] are both amplified by soaking the Cu_2O films in the solution, demonstrative of that the TSC molecules are linked on the Cu_2O surface and could protect the films from deterioration in the subsequent measuring procedures. To describe this statement straightforwardly, we present the schematic for the TSC modified Cu_2O surface, as shown in Figure 5.2d. The FTIR spectra further verify the adsorption of TSC on the surface of Cu_2O, as shown in Appendix Figure 11. 9. Compared to the naked FTO/Au/Cu_2O sample, FTIR spectrum of the FTO/Au/Cu_2O/TSC exhibits the characteristic absorption peaks of carboxyl group of sodium citrate, such as 1600 cm^{-1} and 1392 cm^{-1} due to the –COO– symmetric and anti-symmetric stretching respectively.[152]

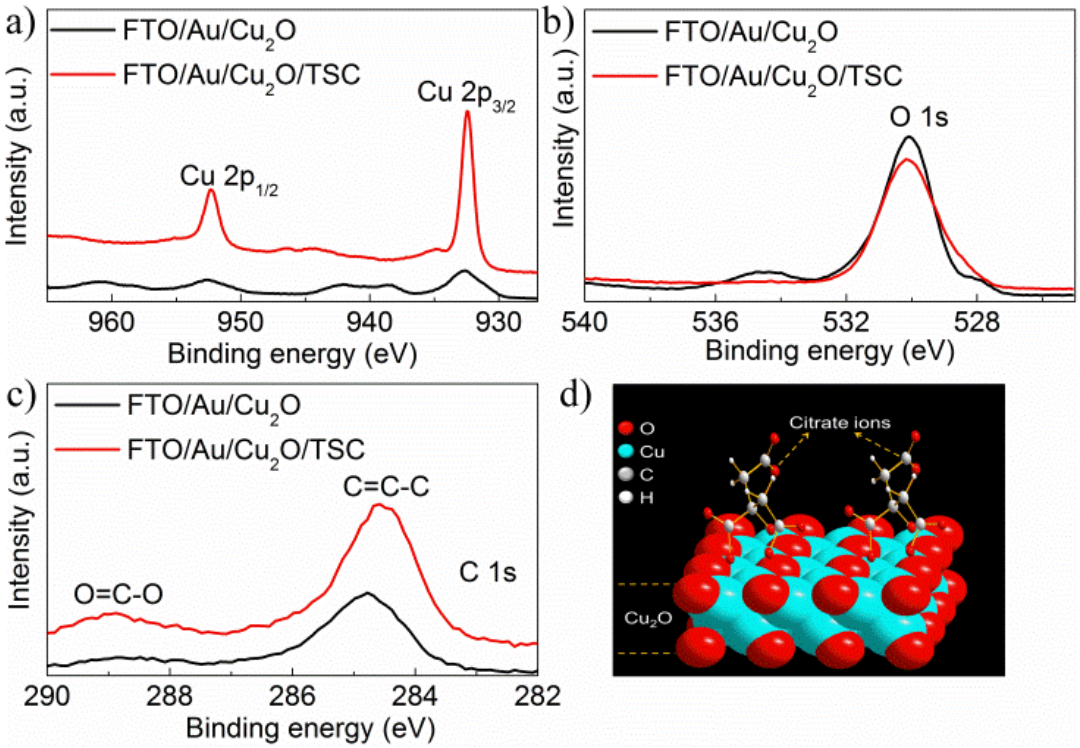

Figure 5.2 a-c) XPS spectra of the as-prepared Cu_2O thin films with different surface conditions. The spectra display the resolved peaks of Cu 2p, O 1s and C 1s, respectively. d) Schematic of the TSC modified Cu_2O surface.

Electronically, such surface modification could also positively impact the doping levels of the Cu_2O films and band bending of the photocathodes when contacting with the electrolyte. Electrochemical impedance investigations were performed by soaking the FTO/Au/Cu_2O electrode in a 0.1 M Na_2SO_4 aqueous solution as the working electrode. A Pt counter electrode and Ag/AgCl reference electrode were used during the measurements. Figure 5.3a shows Mott-Schottky plots at a fixed frequency of 1 kHz for the electrodes with different surface conditions, where a typical p-type feature could be obviously observed. Note worthily, these plots yield apparent flat band potentials of 0.20 V and 0.15 V vs Ag/AgCl for the same photocathode before and after experiencing the surface treatment, respectively. The treatment shifts the flat band potentials negatively and thus results in a strengthened band bending at Cu_2O/electrolyte interface that is profitable for transferring the photo-generated electrons to the surface. Using slopes of the plots, acceptor densities were calculated as 1.06×10^{19} cm^{-3} and 1.53×10^{19} cm^{-3}, respectively (the details of the relative calculation can be found in experiment section). The surface treatment enhances the doping levels and thus the resistance of the system can be accordingly reduced. As exhibited in the inset of Figure 5.3a, the Nyquist plots covering the frequency of 10^5 Hz - 1 Hz at the bias of −0.6 V vs Ag/AgCl demonstrate that charge transfer resistance of the system is prominently decreased by the usage of TSC, given that the semicircle in a Nyquist plot at high frequencies is characteristic of the charge transfer process and the diameter of the semicircle is estimated to be equal to the charge transfer resistance.[105,122] This series of electrochemical measurements illustrate that modification of Cu_2O with TSC is able to positively impact the electronic properties of Cu_2O by increasing the doping density and enlarging the band bending at the interface with electrolyte. These are beneficial for promoting the separation and transfer of the photo-generated charge carriers.

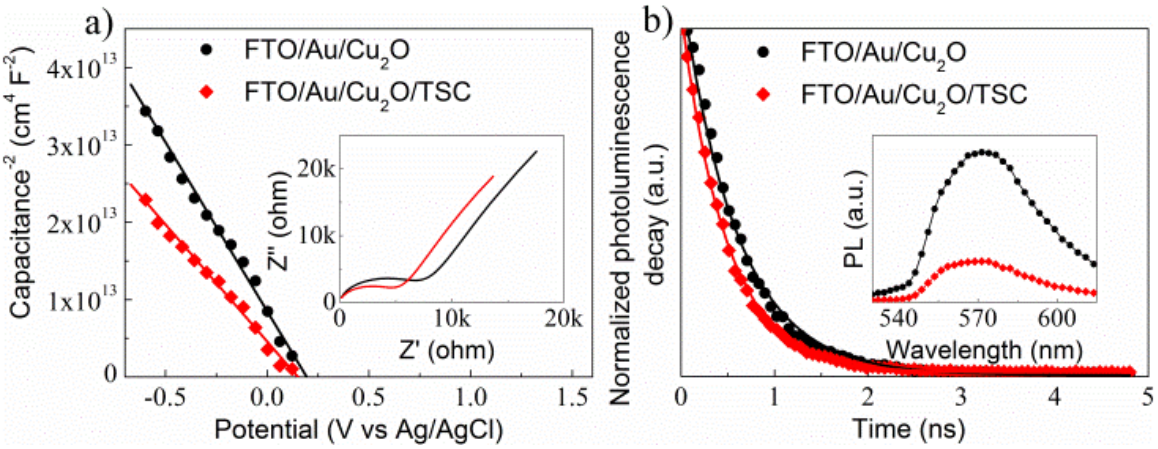

Figure 5.3 a) Mott-Schottky plots with Nyquist plots as the inset. b) Time-resolved photoluminescence decay curves (excitation: 420 nm), the inset shows the steady state photoluminescence spectra (excitation: 420 nm).

Moreover, ascribing to the reduction of Cu (II) impurities, the transfer of photo-generated charges could be facilitated, since impurities have a negative effect on charge transfer and transport. Figure 5.3b shows two representative time-resolved photoluminescence decays after pulsed excitation at λ = 420 nm. Obviously, both of the curves present a rapid decay feature in nanosecond scale, which is in agreement with the reports.[145,146] To be noteworthy, the samples that experienced surface treatment yield a faster decay time as compared with the intrinsic samples, indicating an accelerated charge transfer mechanism induced by the modification of TSC. Using the conventional single exponential model to fit the curves, lifetimes of 0.59 ns and 0.48 ns for the same sample before and after surface treatment were acquired. Table 11.1 in Appendix provides all the fitting parameters. The accelerated charge transfer is bound to enhance the possibility for photo-generated charges contributing to the photocurrent, instead of making them recombine. The steady state photoluminescence spectra are shown in the inset of Figure 5.3b. The peak located at around 570 nm is associated with the near band emission.[147,148] By comparing the two spectra, the photoluminescence intensity of the Cu_2O film is

markedly reduced to its 30% after the surface treatment, which illustrates that the radiative recombination of the photo-generated charges is efficaciously inhibited. The normalized PL spectra are given in Appendix Figure 11.10, which shows that these two peaks have a close broadness. The result indicates that the treatment with TSC could only quench the PL intensity and the intrinsic optical property is nearly influential.

The above analyses point out a great potential to apply this surface treatment for improving the PEC response of Cu_2O based photocathodes. First, by following the conventional photocathode structure for Cu_2O, we fabricated the FTO/Au/Cu_2O/TSC/TiO_2/Pt electrodes. The according SEM image and XRD pattern for FTO/Au/Cu_2O/TSC/TiO_2 are given in Appendix Figure 11.11 and these data evidence the presence of compact TiO_2 layer on Cu_2O, which can protect the layer from electrochemical deterioration. The Pt layer behaves as the catalyst for hydrogen generation. The current density-potential (J-V) characteristics of these electrodes under 100 mW cm^{-2} of solar simulated light are shown in Figure 5.4a. All these J-V curves exhibit a cathodic photocurrent and indicate a distinct p-type feature of the prepared Cu_2O films, being consistent with the Mott-Schottky measurements. FTO/Au/Cu_2O/TSC/TiO_2/Pt electrode delivers an increase of around two times in photocurrent by comparing with the electrode without surface treatment. The photocurrent is realized as high as 3.8 mA cm^{-2} at −0.6 V vs Ag/AgCl. The EQY (%) spectra shown as the inset of Figure 5.4a present the same tendency with that in the J-V analysis. The profiles of these spectra are in agreement with the absorption spectrum of the materials, supporting that the photocurrent is from the charges generated in Cu_2O. Curves of photocurrent vs time curve under interval on-off light irradiation of the FTO/Au/Cu_2O/TiO_2/Pt and FTO/Au/Cu_2O/TSC/TiO_2/Pt electrodes are given in Appendix

Figure 11.12. The data demonstrate a fast photoelectrochemical response of the electrodes.

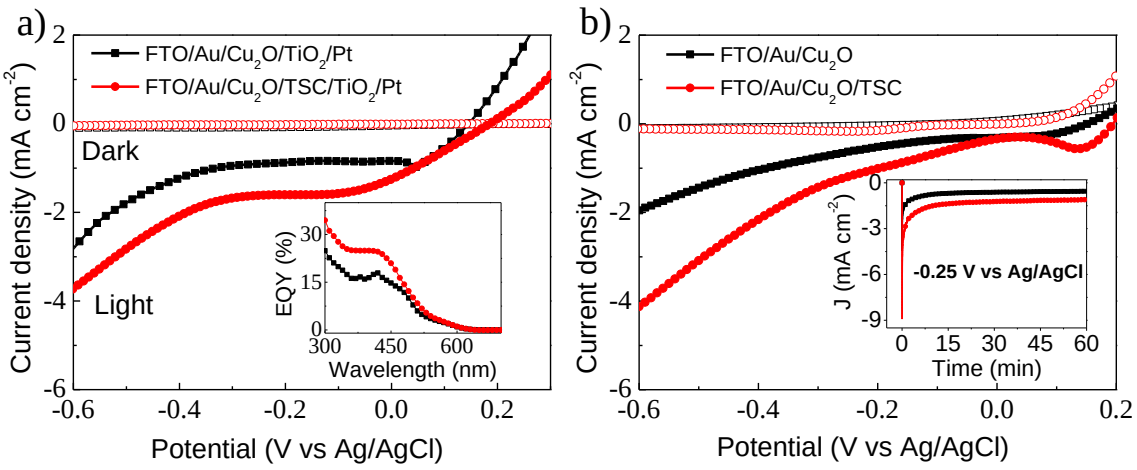

Figure 5.4 a) and b) Current density-potential curves of the Cu_2O based photocathodes with different surface conditions. Inset of (a): EQY spectra of the FTO/Au/Cu_2O/TiO_2/Pt photoelectrode with and without TSC; Inset of (b): Curves of the time-dependent photocurrent measured for the FTO/Au/Cu_2O photoelectrode without/with TSC under AM1.5G (100 mW cm^2) illumination.

Meanwhile, we also checked the PEC performance of the electrodes without the passivation layer of TiO_2 and the relevant results are given in Figure 5.4b. As we expect, the photocurrent of bare FTO/Au/Cu_2O electrodes could also be enhanced dramatically by the surface treatment. The according photocurrent is obtained as 4.2 mA cm^{-2} at -0.6 V vs Ag/AgCl, being even better than that from the FTO/Au/Cu_2O/TSC/TiO_2/Pt electrode. To check the stability of the photocathodes, we measured the photocurrent at a fixed potential and the transient curves are shown in the inset. Though these curves present a decay feature at the initial period after light illumination, the photocurrents are quite stable after 30 s and can be maintained more than one hour. To be noted, photocurrent of the FTO/Au/Cu_2O photoelectrode treated by TSC is always higher than that from the

corresponding bare sample. Such observation confirms that the benefit of TSC to improve the PEC performance of Cu_2O is sustainable and the presence of the molecule on the surface could also be possible to improve the device stability. For checking the stability of the Cu_2O surface after TSC modification even after PEC measurement, atomic force microscopic (AFM) measurement was performed. As shown in Appendix Figure 11.13, we cannot observe obvious changes of morphology. This indicates that increase of photocurrent is not from the change in surface area and the surface is stable even after PEC measurement. Raman spectra in Appendix Figure 11.14 can further prove this conclusion. To check the feasibility of such surface treatment to other Cu_2O involved systems, we also fabricated Cu_2O electrodes on FTO directly without the Au thin layer. As shown in Appendix Figure 11.15, the corresponding J-V curves and EQY spectra exhibit the same trend as that in FTO/Au/Cu_2O electrodes, though the performance is lower. As reported by Zhang *et al.*,[149] the multi-facet Cu_2O nanoparticles have a superior photocatalytic property over the cubic counterparts and our observations support their points.

Collectively, we could reach a conclusion for the benefits of Au layer to the improvement of PEC performance. First, the highly conductive nature has two contributions. First is that it is good for the realization of the highly crystalline Cu_2O film with photocatalytic active polyhedral morphology, which is favorable for collecting the photo-generated electrons efficiently. Second, the surface plasmon effect of the Au layer contributes to the absorption of solar energy and the resulting excited energy could promote the PEC reactions by hot charge or energy transfer to Cu_2O and then to the electrolyte. Third, the scattering effect of Au layer is beneficial for enhancing the solar energy absorption by Cu_2O.

These data indicate that this peculiar surface modification procedure is able to fix the impurities on Cu_2O surface and thereby strengthen the p-type feature of the corresponding Cu_2O film. Accordingly, the PEC performance is dramatically improved via this convenient and cost-less treatment. Regarding that there is a large variety of molecules with multiple functions, our methodology provides a feasible means to optimize the solar energy conversion efficiency of the Cu_2O involved devices from the aspects of ameliorating the surface quality of Cu_2O, protecting the films from deterioration, extending the photon absorption range beyond the absorption threshold of Cu_2O, and even promoting the PEC energy conversion reactions by introducing catalytic effects.[126,150,151]

Chapter 6. Switchable Charge Transfer In The Photoelectrochemical Energy Conversion Process Of Ferroelectric $BiFeO_3$ Photoelectrodes

6.1 Introduction

As the only active materials in the photovoltaic and photoelectrochemical cells for solar-energy conversion, conventional semiconductors have been studied thoroughly for the past several decades.[105,152–155] The aim of technologies in semiconductor device fabrication is to attain energy-conversion efficiency close to the theoretical values based on the band gap analysis of the semiconductors.[156,157] The current approach for energy-conversion devices with traditional semiconductors, however, has two limits: 1) the photovoltage of the devices is limited by the band gap of the semiconductors employed; 2) the charge-transfer direction is confined and fixed by the junctions of the semiconductor/semiconductor, semiconductor/metal or semiconductor/electrolyte.

An alternative approach to overcome the limits of the common semiconductors is to fabricate solar-energy conversion devices with ferroelectric materials. Ferroelectric materials, typically $BiFeO_3$ (BFO)[159–163] and $Pb(Zr,Ti)O_3$ (PZT),[164–165] have a large, stable and tunable remnant ferroelectric polarization which produces a depolarization (internal) electric field extending over the whole film volume, giving the resulting devices high efficiency in separating photo-generated charges and switching charge-transfer directions. Therefore, Walsh et. al.[167] claimed that the excellent performance of Perovskite solar cells based on $CH_3NH_3PbI_3$ originated from the presence of ferroelectric domains in the Perovskite structure. Ferroelectric materials also exhibit unique abnormal photovoltaic effects. By controlling the conductivity of the ferroelectric domain walls, the detected open-circuit potential (V_{oc}) for a standard ferroelectric material, BFO, has been as high as 50 V[162], more than 50-fold larger than that from regular Si solar cells,

indicative of that a huge V_{oc} from ferroelectric materials is achievable even without considering the band-gap limit. In addition, the orientation and intensities of the internal field could be manipulated by external applied voltages and the ferroelectric materials can theoretically maintain the remnant polarization permanently in an inert condition,[168–171] implying that a single ferroelectric photoelectrode could be treated as both a photocathode and a photoanode depending on the orientations of the internal field. Consequently, it is highly realizable that a ferroelectric photoelectrode with an appropriate band gap can serve to drive both water reduction and oxidation reactions just by tuning the remnant polarization directions, which is extremely important in photoelectrochemistry. Moreover, by getting rid of the top Schottky barrier at the contact between the ferroelectric material and metal that generally exists in the ferroelectric photovoltaic devices,[160, 164] the ferroelectric photoelectrochemical electrodes have a better capability in extracting the photo-excited charges and are compatible with other promising photo-active materials, unlike the solid-state counterpart.

To date most of the efforts on the application of ferroelectric materials to solar-energy conversion are confined to solid-state solar cells and few reports concern the photoelectrochemical performance of the ferroelectric materials.[166, 172,173] A systematic study of this area is thus indispensable to promote the evolution of photoelectrochemical energy conversion/storage. Instead of using PZT (band gap: 3.5 eV[164, 165]) as the photoelectrode, herein, we choose another typical ferroelectric material, BFO (band gap: 2.2 eV[163, 174]). The lower band gap of BFO makes it possible to form a good band-gap alignment with surface modifiers that could inject excited charges to the BFO photoelectrodes. Surprisingly, we found that the charge transfer from the bare BFO to the electrolyte and from the surface modifiers to BFO could be manipulated by the poling pretreatment. A series of surface modifiers, such as molecular dyes and CdSe quantum

dots, was investigated and provides strong support that ferroelectric photoelectrodes are the right candidates for the next generation photoelectrochemical electrodes.

6.2 Experimental section

Materials and Chemicals: $Bi(NO_3)_3 \cdot 5H_2O$ (≥ 98.0%), $Fe(NO_3)_3 \cdot 9H_2O$ (≥ 98.0%), 2-methoxyethanol (99.8%), citric acid monohydrate (≥ 99.0%), acetic acid (≥ 99.7%), lead(II) acetate(≥ 99.5%), titanium(IV) isopropoxide(≥ 98.0%),zirconium(IV) isopropoxide(≥ 99.0%), Rhodamine B (≥ 95.0%), Rose Bengal (95.0%), Brilliant Green (95.0%), selenium powder (≥ 99.5%), 1–octadecene (≥ 99.5%), cadmium acetate dehydrate (≥ 98%), oleic acid (≥ 99.0%), hexanes (≥ 99.5%), methanol (99.8%) and acetone (99.8%) were used as received from Sigma Aldrich. Insulating epoxy (3430) was purchased from Loctite.CEC020P ITO/glass (thickness: 150 nm/1.1 mm; sheet resistivity: ≤20 Ω/□; transmissivity: 88.9%for wavelength 400nm) was purchased from PGO Glass.

Preparation of polycrystalline BFO films: BFO thin films were prepared on ITO/glass substrates following the modified spin-coating procedure reported where else.[175] The precursor solution was prepared by dissolving $Bi(NO_3)_3 \cdot 5H_2O$ (0.2 M) and $Fe(NO_3)_3 \cdot 9H_2O$ (0.2 M) in 2-methoxyethanol. Citric acid was added sequently as the chelating agent while the solution was stirred continuously for approximately 1h. Then, the BFO films were obtained by spin coating at 4000 rpm for 30 s and pyrolyzed at 400 °C for 10 min in ambient air. These steps were repeated several times to increase the film thickness. A final annealing at 550 °C for 120 min in air was performed to achieve better crystallinity and the resultant film thickness was about 300 nm for the film spin-coated 9 cycles.

Preparation of polycrystalline PZT films: The PZT films with a stoichiometry $Pb(Zr_{0.20}Ti_{0.80})O_3$ were deposited on ITO/glass by a sol-gel method. The precursor solution for the coating was prepared by dissolving appropriate amount of lead acetate ($Pb(CH_3COO)_2 \cdot 5H_2O$) in acetic acid at room temperature in air. A stoichiometric amount

of titanium isopropoxide ($Ti((CH_3)_2CHO)_4$) and zirconium isopropoxide ($Zr((CH_3)_2CHO)_4$) was slowly added to the precursor solution. Then 2-methoxyethanol was added to adjust the concentration until a clear yellow sol with a molar concentration of 0.2 mol/L was obtained. A 10 mol% excess amount of lead acetate was used to compensate the Pb evaporation during annealing. The wet films were dried at 150 °C for 5 min in air and annealed at 400 °C for 10 min. The thicknesses of all prepared films were controlled to be about 300 nm. Finally, the films were crystallized in air atmosphere under 550 ºC for two hours.

Fabrication of BFO and PZT photoelectrodes: A strip of conductive copper tape was stuck on the exposed ITO part of the BFO (PZT)/ITO to extent the conducting circuit and threaded through a glass tube and then sealed with an insulating epoxy. Electrode areas were optically measured as 0.5 cm^2. For measuring the hysteresisloop of BFO and PZT films and evaluating the Schottky barrier at BFO/ITO, about 40 nm thick Au dots with diameters of 0.28 mm were deposited onto the BFO and PZT films by using physical vapor deposition, respectively.

Syndissertation of CdSe quantum dots: A 50 ml three-necked round-bottom flask with 0.047g Se powder and 7.092 g ODE was purged under N_2 flow with constant stirring for 30 min, then heated to 280 ^oC by using a heating mantle until the Se powder was completely dissolved and a pale yellow solution was formed. In parallel, for the cadmium precursor, a 25 ml Erlenmeyer flask containing 0.1596 g $Cd(CH_3CO_2)_2$ and 3 ml OA was purged under N_2 flow with constant stirring and maintained at ~120 ^oC for injection. Then, the hot Cd precursor solution was quickly injected to the Se hot pale yellow solution and the temperature dropped to ~260 ^{o} C immediately. Within 2-3 min after injection, the solution turned orange indicating the formation of quantum dots and the color deepened with increasing reaction time. To obtain different sized quantum dots,

aliquots were taken out at different time intervals. After cooling to room temperature, the quantum dots were washed with methanol and centrifuged 3 times and then were precipitated and washed with acetone for another 3 times. Finally, the purified quantum dots were dispersed in hexanes for further use. This procedure was modified from the procedure reported elsewhere.[183]

Modifying monolayer CdSe quantum dots on BFO electrodes: BFO photoelectrodes were first immersed in a CdSe quantum dot suspension in hexanes for 20 min. After removed from the solution, the photoelectrodes were thoroughly rinsed with neat hexane and soaked in neat hexane for 20 min to remove loosely physisorbed materials. Subsequently, the quantum dots sensitized BFO electrodes were soaked in 10% v/v EDA methanol solution 10 min for ligand exchange before being used for photoelectrochemical measurements.

Photoelectrochemical measurements: Poling pretreatment was conducted in a quartz electrochemical cell with BFO photoelectrode as the working electrode and Pt plate as the counter electrode, respectively. Due to the large electrochemical windows, propylene carbonate solution containing 0.1 M $LiClO_4$ was chosen as the electrolyte for poling. The poling bias was controlled in range of +8V to –8V and the poling time was selected as 10 s. External quantum yield was measured with an Oriel 150 W Xe arc lamp (Newport) and a quarter-turn single-grating monochromator (Newport). Sample measurements were recorded with chopped illumination (20 Hz) and no external bias was applied during the measurements to get a pure photocurrent signal. The output current signal was connected to a Merlin digital lock-in radiometry system and the output signal from the lock-in amplifier was fed into a computer controlled by TRACQ BASIC software. Current-potential plots were measured using the digital BioLogic potentiostat (SP-200) and 0.1 M KCl aqueous solution served as the electrolyte. A Pt counter electrode and a Ag/AgCl

reference electrode were used during the measurements and standard 300 W Xe lamp (Newport) served as the light source which was characterized to 100 mW/cm^2 by a Si photodiode (Newport). Investigation of charge injection from molecular dyes to BFO films was performed by dissolving each dye in the electrolyte with a 0.05 mM concentration.

Characterizations: Powder XRD was recorded on Bruker D8 Advance equipped with graphite monochromatized high-intensity Cu Kα radiation (λ = 1.54178 Å). The SEM images were obtained by Auriga Zeiss FIB scanning electron microscope. Room-temperature UV-Vis absorption spectroscopy was carried out on Varian Cary 5000 UV-VIS–NIR spectrophotometer. Polarization-Electric (*P-E*) hysteresis loops were examined using a precision ferroelectric analyzer from Radiant Technology. The dark leakage current J–V characteristic of Au/BFO/ITO was recorded by Keithley 4200.

6.3 Result and Discussion

Rather than growing BFO films epitaxially by radio frequency (RF) magnetron sputtering or pulsed-laser deposition (PLD),[160,162] we adopted a cost-advantageous technology, spin-coating, to obtain high-quality BFO films on ITO/glass.[176] Preparation details and a description of the methods employed for data collection are provided in the Supporting Information. Figure 6.1a presents the XRD pattern of the polycrystalline BFO films on ITO-coated glass substrate, where the diffraction peaks at 2θ values of 22.48,31.89, and 39.18 could be indisputably ascribed to the reflection of (100), (110), and (111) planes of BFO (JCPDS card No.72-2112), respectively. No diffraction signatures of $Bi_2Fe_4O_9$ and Bi_2O_3/Fe_2O_3 are observed, suggesting that the as-prepared BFO films possess a pure Perovskite structure. Additionally, being consistent with other reports,[163, 174] the energy band gap of the BFO film was characterized as 2.14 eV by the

absorption spectroscopy shown in Appendix Figure 11.16, indicating that it is a superior material for photoelectrochemistry than its counterparts, such as PZT and BaTiO3.[174, 177]

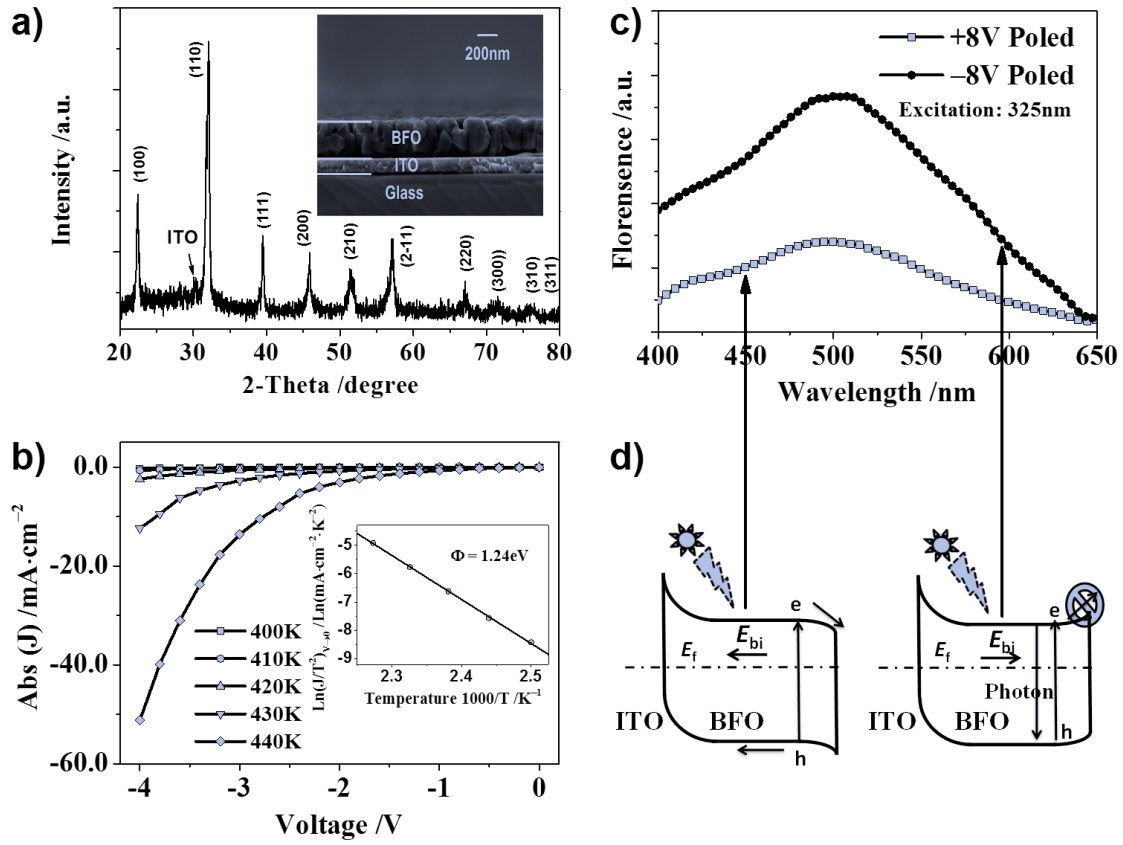

Figure 6.1 a) XRD pattern of the BFO films (inset: cross-sectional SEM). b) Dark J-V plots of the structure: Au/BFO/ITO. c) The fluorescence spectra and d) schematics of energy band gap alignment of the BFO/ITO undergone the poling of +8V and −8V, respectively.

Figure 6.1a inset image displays the representative cross−sectional SEM of the spin-coated BFO thin film on ITO/glass allows the thicknesses of BFO and ITO to be gauged as about 300 nm and 100 nm, respectively (Figure 6.1a). The BFO/ITO interface is of high prominence visually, suggesting that this electronic junction should probably play a significant role in the photoelectrochemical performance. Thus, the BFO/ITO junction was investigated and the relevant data are illustrated in Figure 6.1b. On the basis of the dark J-V analyses of the Au/BFO/ITO devices under various temperatures and the fitting

of Schottky-Simmons equation (Figure 6.1b), it is demonstrated that the BFO/ITO contact is a typical Schottky junction and the electronic barrier height for BFO/ITO is estimated to be around 1.24 eV, being in agreement with reported values.[178] The measurement and analytical details can be found in the Chapter 3. Yang et al. and Schafranek et al.[178, 179] reported that the Schottky height in the metal/ferroelectric film was mainly determined by the interfacial charge percentage, which is related to interfacial defects such as oxygen vacancies generated in the annealing procedures. Accordingly, such a Schottky barrier could not be changed reversely by poling treatments, thus we can focus on the contact between the BFO and the electrolyte.

Though the ferroelectric properties of the spin-coated BFO thin films are not comparable with the films prepared by high-vacuum techniques, a set of P-E hysteresis loops as a function of test voltages is shown in Appendix Figure 11.17. It is still clearly indicates the existence of the ferroelectric hysteresis in the samples, providing us with a cost-efficient platform to tune the internal electric field induced by the remnant polarization and thus to manipulate the charge transfers of the photoelectrochemistry. Steady-state fluorescence spectroscopy is a convenient methodology to analyze photo-generated charge-transfer dynamics. Before fluorescent measurements, the BFO electrodes were pretreated electrochemically in a propylene carbonate solution by applying external biases for 10 s. The details of the discussion on the poling pretreatment method, particularly the choice of –8 V for poling, are presented in the Appendix Additional data for chapter 6. As shown in Figure 6.1c, after –8 V poling, the BFO electrode has a higher fluorescence intensity than the same electrode that has experienced +8 V pretreatment, revealing that the fluorescent recombination of the photo-generated charges is initiated by the –8 V poling. Poling potentials, particularly the potentials with an exact value larger than the coercive field, re-orientate the distribution of the

ferroelectric domains that were differently poled and the direction of internal field is correspondingly tuned.[161, 163] As a consequence, the internal field in BFO films points to the BFO surface after being poled by –8 V and a downward band bending is formed at the BFO/air interface or the BFO/electrolyte interface (Figure 6.1d, right). In combination with the electron barrier at the ITO/BFO contact, the photo-generated electrons can only be trapped in the bulk of the BFO films and thus recombination with the holes in the valence band becomes the sole way to release the excited energy. On the other hand, a positive pretreatment potential switches the internal field so that it points towards the ITO electrode and gives an upward band bending (Figure 6.1d; left) which promotes the photo-generated electrons to move to the surface. Considering that the Schottky barrier at BFO/ITO is favorable to drive photo-generated holes efficiently to ITO, the possibility of electron–hole recombination is greatly reduced in this case because of the separation of the charges.

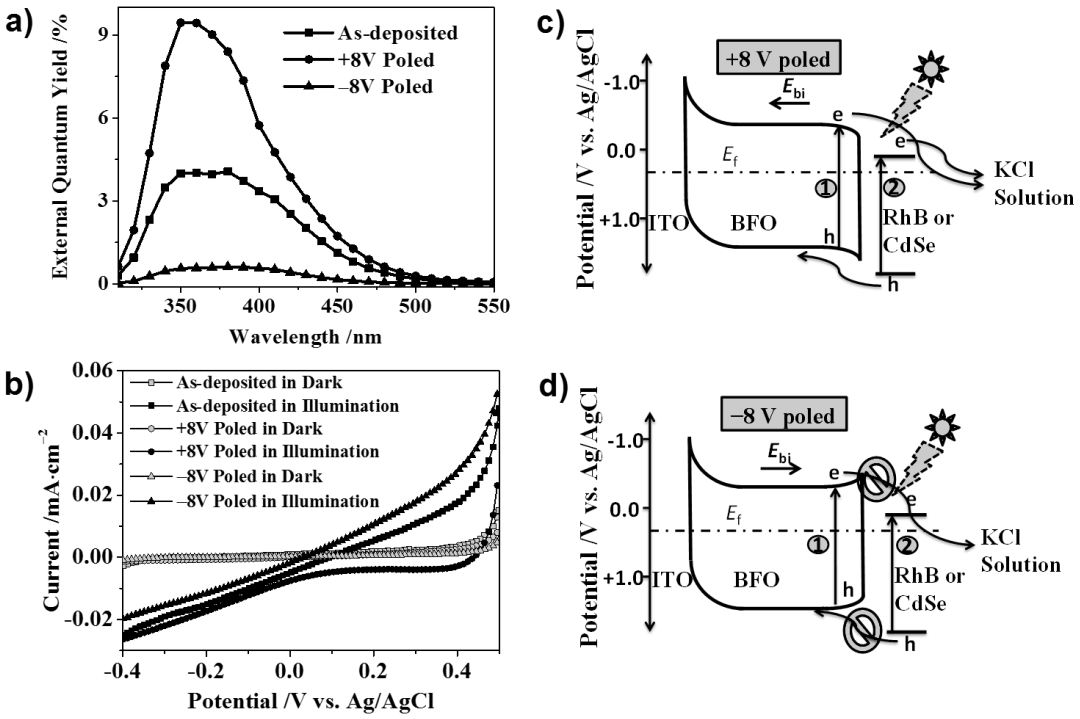

Figure 6.2 a) External quantum yield spectra measured for BFO electrodes before poling and after +8 V and −8 V poling. b) Photocurrent−potential characteristics of relevant

photoelectrodes with different polarization states. Schematics of the mechanisms in photo-excited charge transfer from BFO films to the electrolyte (1) and excited surface modifiers to the BFO films after the BFO films (2) were positively c) and negatively d) poled, respectively.

Figure 6.2a and 6.2b show the representative steady-state photoelectrochemical data for the BFO/ITO photoelectrodes that have undergone poling pretreatments (+8 V or –8 V) and been immersed in an aqueous solution (0.1M KCl) for measurements. The wavelength-dependent external quantum yield spectra measured without any external bias undoubtedly demonstrate that the polarization states in the ferroelectric films determine the corresponding solar-energy conversion efficiencies. In accordance with the fluorescent analysis, the +8 V poling treatment results in the highest external quantum efficiency owning to the lowest charge recombination rate in comparison with the same electrode experienced no poling or –8 V poling. The external quantum yield of the intrinsic sample is higher than the same sample with –8 V polling treatment, implying that the ferroelectric domains in the as grown polycrystalline BFO films are randomly distributed and not optimized. Correspondingly, the photocurrent–potential plots of the as-prepared sample show intermediate results between the positively and negatively poling conditions as illustrated in Figure 6. 2b. To simplify the discussion, we just focus on the investigation of the samples under positively or negatively poling conditions. The external quantum yield of the +8 V poled electrode is almost 10-fold larger than the same sample that underwent –8 V poling, illustrative of an excellent capability for tuning the photocurrent in BFO photoelectrodes. The external quantum yield of the photoelectrode with –8 V poling is lower than 1%. This negligible value is probably from the photo-generated charges at the BFO surface, since the downwards band bending caused by the –8 V poling prevents the electrons from transferring to surface. The profile of these

external quantum yield spectra qualitatively matches the absorption spectrum of the BFO films with the value threshold at 500 nm (Appendix Figure 11.19), suggesting that the photo-generated charges in BFO contribute solely to the photocurrent in this case.

The photocurrent–potential plots of the poled BFO photoelectrodes as shown in Figure 6.2b reveal two distinct features. First, the electrodes both positively and negatively poled, exhibit a cathodic photocurrent, meaning that the photocurrent is formed by the transfer of photo-generated holes rather than the electrons to the ITO/glass. The existence of the 1.24 eV Schottky barrier at BFO/ITO interface is mainly responsible for this feature. Such a barrier obstructs electron but boosts hole transfer to the ITO electrode so that only a cathodic photocurrent is obtained, no matter how the BFO films are poled. Second, the parameters for characterizing the photo response of the BFO electrodes show that they have an impressive tunable capability. At 0 V vs Ag/ AgCl, the photocurrent could be switched from around 0 mA cm^{-2} to 10 mA cm^{-2} and V_{oc} also has a good variability with the value change from 33 mV to 440 mV, after the poling bias of the ferroelectric electrode is manipulated from –8 V to +8 V. As the scanning potential increases negatively, the photocurrent of the –8 V poled electrode also changes accordingly, that is, becomes more negative. Although the negative scanning potential is smaller than the coercive field and cannot switch the orientation of the remnant polarization, it can still raise the Fermi level of the BFO films, reduce the electron barrier induced by the –8 V poling at the BFO/electrolyte interface and thus cause the leaking of current to the electrolyte. In the whole scanning range, the photocurrent of the –8 V poled electrode is always lower than the same electrode after +8 V poling, indicating that the band bending at the BFO/electrolyte interface induced by poling treatment is crucial to the tuning capability of the ferroelectric electrode. The mechanism of the photo-generated

charge transfer in BFO is schematically shown as the procedure (1) in Figure 6.2c and 6.2d.

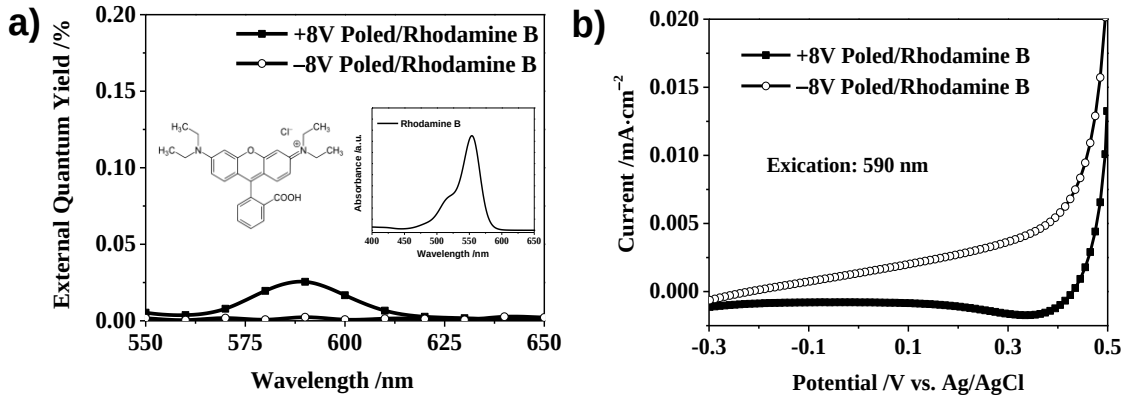

Figure 6.3 a) External quantum yield spectra of the BFO electrodes measured with 50 μM Rhodamine B and the absorption spectrum of Rhodamine B in water (inset). b) Photocurrent−potential measurements under a 590 nm illumination (~1mW/cm^2) from a monochromator.

The poling treatment could not only adjust the photogenerated charge transfer in BFO films, but could also be of use in tuning the excited charge transfer from the surface modifiers. Separate investigations were carried out to assess how the poling treatment impacted the charge transfer. The steady-state photoelectrochemical data were collected by immersing the ferroelectric photoelectrode in an aqueous solution with 0.1M KCl as the supporting electrolyte and 50 μM Rhodamine B as the modifier. As presented in Figure 6.3a, the external quantum yield spectra demonstrate that the +8 V poled electrode exhibits a prominent peak at 590 nm and the profile of this peak is in agreement with the absorption spectrum of Rhodamine B (Figure 6.3a, inset), a result which is strongly indicative that the photocurrent signal measured at wavelengths longer than the band-gap energy of BFO is from the photo-excited hole injection of Rhodamine B. When the ferroelectric photoelectrode is poled at –8 V, the external quantum yield peak from Rhodamine B disappears. To support this observation, photocurrent–potential

measurements were conducted under 590 nm illumination (ca. 1 $mWcm^{-2}$) from a Newport monochromator. Consistent with the external quantum yield measurements, the +8 V poled electrode shows an clear cathodic photocurrent while no cathodic photocurrent is observed for the same electrode with –8 V poling (Figure 6.3b). The position of the BFO valence band is reported to be around 1.5 V vs the normal hydrogen electrode (NHE),[180, 181] higher than the highest occupied molecular orbital (HOMO) position of Rhodamine B.[156] As shown in Figure 6.2c,d, the consequent band gap alignment for BFO/Rhodamine B is favorable for the excited hole injection from Rhodamine B to BFO films. Once the excited holes are captured at the surface of the BFO films, the poling-induced band bending determines the transfer of the injected holes. The upward band bending by +8 V poling drives the holes to the bulk of the BFO films and forms a sensitization photocurrent collected by the ITO electrode. The downward band bending by –8 V poling, however, inhibits the movement of the holes to the bulk of the BFO film and the holes could only be trapped at the BFO films surface thus no sensitization photocurrent is observed. This novel charge-transfer switching ability is also occurs for other triphenylmethane dyes, such as Rose Bengal and Brilliant Green as demonstrated in Appendix Figure 11.20.

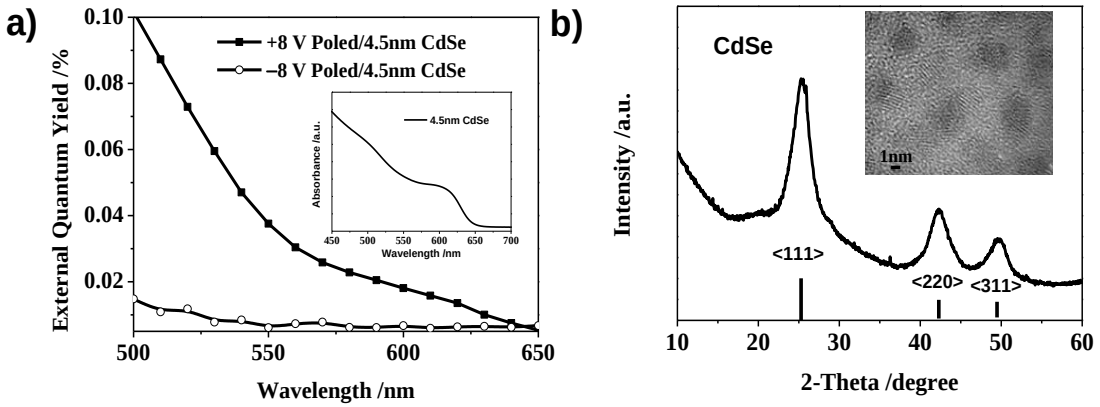

Figure 6.4 a) External quantum yield spectra of the BFO electrodes sensitized with CdSe quantum dots and absorption spectroscopic measurements of CdSe quantum dots in hexanes (inset). b) XRD pattern and TEM image (inset) of CdSe quantum dots.

Figure 6.4a illustrates the representative external quantum yield spectra of the BFO electrodes sensitized with CdSe quantum dots and measured in an aqueous solution with 0.1m KCl. The XRD pattern and TEM image in Figure 4b confirm that the prepared nanoparticles are 4.5 nm CdSe quantum dots. To adsorb quantum dots, the BFO electrodes were soaked in a hexanes solution with 10 $mgmL^{-1}$ oleic acid capped CdSe quantum dots for 10 min, rinsed with hexanes, immersed in a methanol solution with excess ethylenediamine for ligand exchange, and finally placed in the aqueous test electrolyte for analysis. In Figure 6.4a, the +8 V poled BFO/ CdSe exhibits a pronounced photocurrent signal unlike the –8 V poled counterpart beyond the absorption threshold of BFO. The well matched profile of the external quantum yield spectrum with the absorption spectrum of the 4.5 nm CdSe quantum dots (Figure 6.4a), suggests that the photo-excited hole injection from CdSe quantum dots contributes to the increased external quantum yield. For the –8 V poled BFO/CdSe, no photocurrent beyond the BFO absorption threshold is observed, confirming that the charge injection from quantum dots could also be switched by the poling pretreatment of the ferroelectric electrodes. Considering the large depolarization electric field across the ferroelectric film, the

observation of the excited hole injection from inorganic quantum dots to positively poled BFO films supports the idea that ferroelectric photoelectrodes could be alternative platforms to extract multiple holes (electrons) generated from one absorbed photon or hot holes (electrons) in quantum dots without losing any photovoltage, though more research needs to be made.

The cumulative experimental results illustrate an alternative design strategy for constructing smart photoelectrochemical systems with a good switchable capability for charge transfer. Specifically, the BFO photoelectrodes offer advantages that differ from those of conventional semiconductor photoelectrodes. The switchable band bending at the surface of the ferroelectric electrodes could be utilized to drive both reduction and oxidation reactions according to the orientation of the remnant polarization. Additionally, such reactions are not limited to the photon assisted reactions such as water splitting, but common electrochemical reactions could also be tuned by the poling treatments of the ferroelectric electrodes.[182] With regards to the photoelectrochemical energy conversion, the tunability of the charge transfer in the ferroelectric photoelectrode broadens the possibility to design a complete photoelectrochemical cell with only ferroelectric electrodes that behave as photoanodes or photocathodes relying on the choice of poling biases. Although it was not a primary focus of this study, these data also imply that the BFO photoelectrodes still have a pounced external quantum efficiency by considering the relatively poor ferroelectric performance in comparison with single crystalline BFO films.[160] Additional progress in the spin-coating technique for improving the ferroelectric performance of BFO should be made, to utilize the orientation of the ferroelectric domains maximally and to harvest the excited charges or even hot charges from quantum dots-efficiently.

Chapter 7. Nanoarrays: First Optimation Of Space Effect In-Between $CuWO_4$ Nanograin Arrays For Supreme Performance of Photoanode Water Splitting

7.1 Introduction

The need for energy is continuously increasing and will remain same in the future as well. Unfortunately, the availability of fossil fuels, which are currently the most prominent source of energy, will decrease in the next few decades. This issue evoked researchers to develop new and renewable energy sources which are environmentally-friendly. In 1972, Fujisima and Honda set an important foundation on affordable environmentally-friendly TiO_2-based[91] renewable energy technology which effectively utilizes solar energy. Afterwards, the explorations and exploitations of various other materials[189], structure improvisation[190], and fabrication technic[191] are endeavoured to improve the quality and performance of various solar energy conversion devices. One of the interesting research objectives is hydrogen fuel production through the process of photoelectrochemical water splitting, which has been proved to be economic and environmentally-friendly. Gratzel et. al.[99] and some other researchers[192-194] managed to realize the materials such as Cu-I-S, Cu-O, Fe-O, Cu-Bi-O, Cu-W-O, and some others in the form of multi-tier thin film for PEC application. The presence of numerous layers in a multi-tier thin film hinders the achievement of high effectiveness in PEC as it not only has to fit the band gap (from effective range of 3.2 eV to 1.6 eV) but also the fabrication technic and material deposition one another within the multi-layer will significantly determine the quality and final result of mobility, density electron (n-type), and hole (p-type), optical absorption, as well as adequate resistance.

Tungstate oxide (WO_3) is an attractive material to be observed and analysed as it has a high potentials in the fields of optic, optolectronic, diamagnetic, photocatalyst, and sensor.[194-196] A specific example for a tungstate is copper tungstate oxide ($CuWO_4$). Hitherto, most of the previous reports are focused on the development of $CuWO_4$ thin film with a band gap in the ranges of 1.8 eV to 2.4 eV by employing various deposition methods. Martin et. al.[202] reported the comparison of result of WO_4 and Cu. Nevertheless, there is no report demonstrating at least half of the theoretical efficiency (13%) of $CuWO_4$. The fabrication of thicker electrodes by sol-gel process or by electrodeposition results in a low external quantum efficiency.[195] Furthermore, the rational construction of $CuWO_4$ nanostructure is expected to improve light absorption efficiency as well as broaden the contact surface area, which in turn improves the performance of PEC. Despite the ability of nanostructure in transferring the holes at mineral/electrolyte interface efficiently via diffusing across axial direction of the nanostructures, the minimum mobility of electrons within $CuWO_4$ remains an obstruction since they have to transport along the radial direction to culminate to the current collector.[1961 In the case of nanoarrays, the core functions as a conductive path, it potentially becomes a perfect candidate to both facilitate the electrons separation and also simultaneously the transportation in the axial direction.[216] Additionally, new approaches are required to develop $CuWO_4$-based nanostructures to efficiently utilize the visible light absorption capability as well as good stability of $CuWO_4$. Moreover, multistep fabrication processes are challenging because of their complex structure, which complicates the quantitative optimization of the charge carrier collection.[225]

In this work, the fabrication of $CuWO_4$ nanograin arrays *via* controlled electrodeposition of $CuWO_4$ into nanoimprinted AAO template at an applied current of -0.4 mA/cm^2 and subsequent removal of the nanoimprinted AAO template. [197-200] This

work also analyses the influence of the in-between space of $CuWO_4$ nanograins in the array on the performance of PEC tested using a solar simulator which operates at 100 mW/cm^2. As a result, the realization of electrodes based on $CuWO_4$ nanograin arrays proof enhances the performance optimization for electrode application towards PEC.

7.2 Result and Discussion

To present, nanoimprinted AAO template technique has been one of favourite technologies proven to significantly contribute to good fabrication of nanostructure arrays, perfect structure manipulation, as well as low-cost and relatively easy production.[200-201] As depicted in Figure 7.1, simple schematic steps of $CuWO_4$ nanograin arrays fabrication is described in details which chronologically explains it step by step. The basic principle of this fabrication is ordering nickel (Ni) as self-support on aluminium which has been polished as Step 1, anodization for 30 minute on 4 ^oC temperature and soaked in H_3PO_4 (5 wt%) solution to control pore of 50 nm to 200 nm. Figure 7.1 from AAO template is an illustration of the distance between two axis (Step II) which entirely depends on the soaking time on H_3PO_4 (5 wt%), continued with TiO_2 dan Au (Step III) deposition, electrodeposition using 3 electrodes with apply bias −0.4 mA Vs Ag/Agcl and is heated at 550 ^oC temperature for 2 hours in the air (Step IV), plating-nickel (Step V), eliminating the back-side AAO (Step VI), and is finished by eliminating the template by using H_3PO_4 (5 wt %) solution for 3 hours in 30 ^oC temperature, and the layer protection TiO_2 5 nm with ALD is added to all samples.

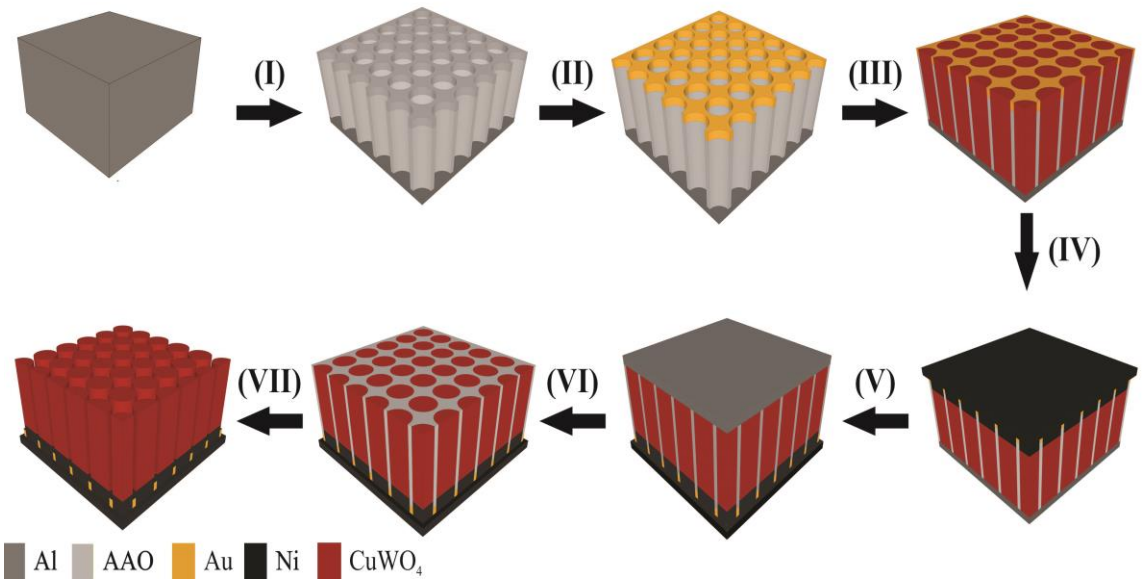

Figure 7.1 Schematic illustration of fabrication process of $CuWO_4$ nanograin arrays using nanoimprinted AAO template technique.

The nanograin arrays acquired from nanoimprinted AAO template are shown in Figure 7.2(a-a1, a2), and we can see that morphology of $CuWO_4$ nanograin arrays is well-organized in large good order due to high nanoimprinted AAO template structure control. With relatively equal length of nanograin arrays about 1 to 1.7 µm, and relatively wide in-between space is around 50 nm aim 200 nm. When the electrolyte penetration will conveniently work on $CuWO_4$ nanograin arrays without any barriers, and it consequently will impact on high electron and hole mobility. To add more advantage of this nanoimprinted AAO template, low impurity effect can be added even though it is heated above 550 ^{o}C temperature along with $CuWO_4$ in the air. SEM image in Figure 7.2 (b-e) clearly describes the effect of nanoimprinted AAO template, and the invisibility of nanoimprinted AAO template trace gives another proof that this technology is highly effective for the fabrication, especially for controlling in-between space of $CuWO_4$ 50 nm, 100 nm, 150 nm, and 200 nm, respectively.

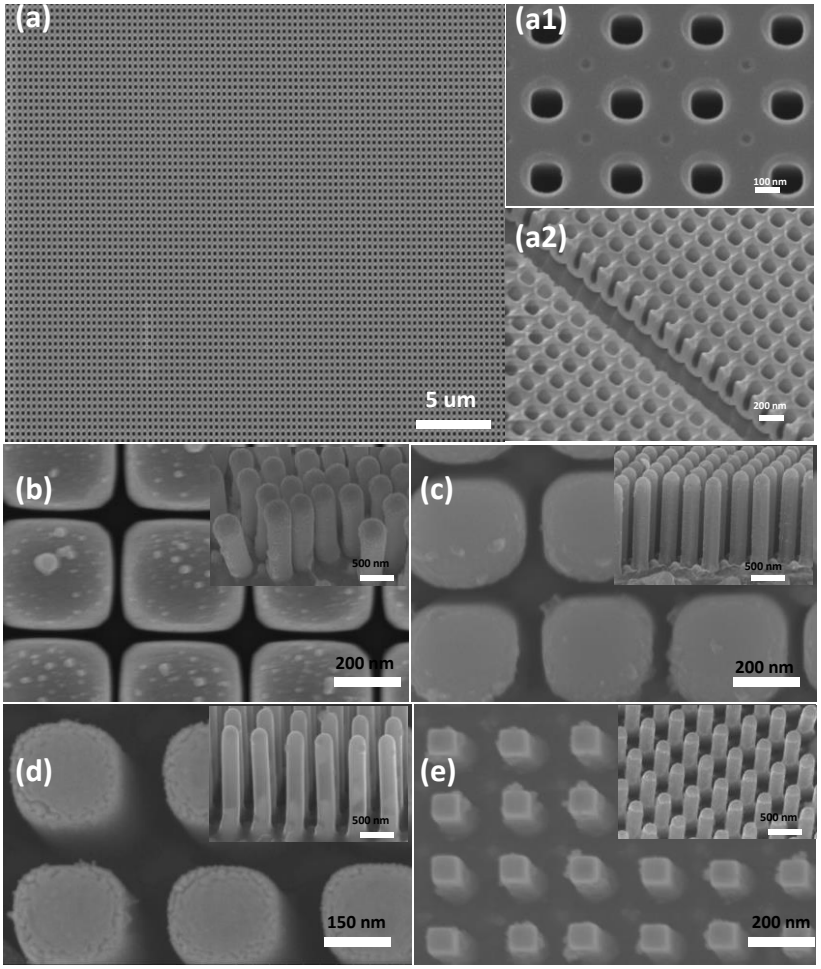

Figure 7.2 SEM images of the nanoimprinted AAO template show in large area (a), top view which shows the pores of the template (a1), and cross-sectional view nanoimprinted AAO template (a2). SEM of the $CuWO_4$ nanograin arrays different in-between space (b-e) of the 50 nm, 100 nm, 150 nm, and 200 nm (Insert: cross-section), respectively.

Figure 7.3 shows the HRTEM of a $CuWO_4$ nanograin. From this analysis, nanograin structure with diameter of 200 nm is formed (the figure is not shown here), which distinguished from $CuWO_4$ thin film previously reported. This becomes the critical foundation to propose a hypothesis that the electron-irradiation process will easily enable the penetration into compartment with broader width on surface, and contributes to hydrogen evolution reaction on counter electrode, when simultaneously the process of oxygen evolution reaction on $CuWO_4$ nanograin arrays is occurring, compared to the

$CuWO_4$ thin films. High resolution image of electron microscopy transmission and selection of the corresponding selected area electron diffraction pattern are shown in Figure 7.3 (a-b). To strengthen results, electron diffraction tomography (EDT) $CuWO_4$ is used to obtain the standard form with a space symmetric group *Cmcm* and parameters unit per cell a = 3.72 Å, b = 5.51 Å, and c = 3.98 Å, as shown in detail in Figure 7.3 (b). From the image, high quality single-crystal appears as shown in the previous structure. Furthermore, as also shown in Figure 7.3a, the results of transmission electron microscopy scan with aberration corrector on the sample which is a projection to the crystalline quality of the sample indicates that the average distance of 0.22 nm between the adjacent lattice planes could still be estimated, corresponding to the (-110) plane of the materials. It also provides information of high-crystallinity consistency, structure, and distribution of Cu and W in $CuWO_4$ nanograin arrays. This is also a complement to the information on bright element clearly shown from the simulation fast Fourier transform (FFT), in which the atomic column O is distributed randomly in the structure. Meanwhile, XRD pattern on this electrode is demonstrated in Figure 7.3 (c) along with Millner index of crystal single structure. As a comparison, we conducted a measurement on thin film and nanograin arrays in which both were heated in the air at 550 ^oC for 2 hours, since in $CuWO_4$ was heated at below 550 ^oC temperature, the XRD pattern was not constructed.[203-204] The (001) on angular position of 24.21^o was seen, and (002) as the reflexion of angular position was 33.27^o. To further confirm the chemical composition of the prepared $CuWO_4$ nanograin arrays, energy-dispersive EDX mapping of a representative particle was carried out and the relevant images are shown in Figure 7.3, where we could definitely obtain signals from Cu, W and O. The reason for the improved crystal quality is probably be that the very thin TiO_2 on template can supply a uniformly distributed electric field and activation energy for the electrochemical deposition to form

nanograin arrays, and notably lower resistance. The composition of this prepared material is also identified by the scanning result of XPS spectra as depicted in Appendix Figure 11.21. The identified peak of energy is W (5d $_{7/2}$) and W (5d $_{5/2}$) where each is 35.05 eV and 37.06 eV as exemplified in Appendix Figure 11.21 is the peak of standard energy of W^{6+}.[202] Spectra region Cu(2p) is shown by the peak of Cu(2p $_{3/2}$) dan the peak of Cu(2p $_{1/2}$) at 933.8 eV dan 954.9 eV, which are recognized as the energy peaks of Cu^{2+}.[203] The last one is O(1s) area which is depicted by one peak (1s) is the lattice oxide domain, and generally describes the hydroxide surface on metal oxide surface.

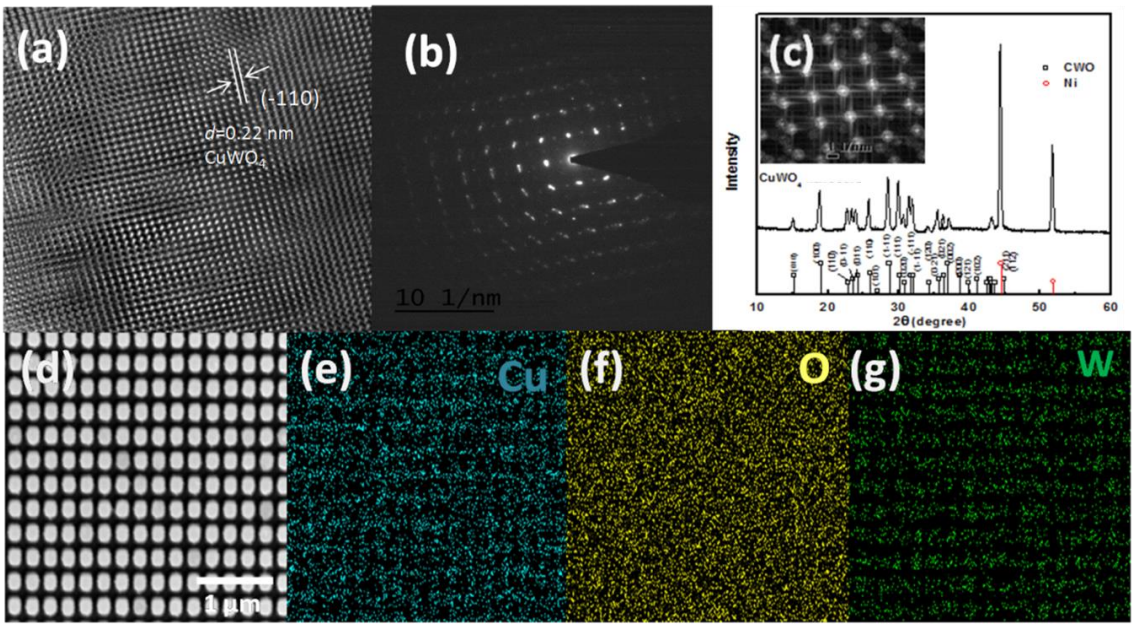

Figure 7.3 (a) High-resolution transmission electron microscopy image of a $CuWO_4$ nanograin obtained arrays during sample preparation, (b) Corresponding selected area electron diffraction pattern acquired from the nanograin, (c) XRD pattern of sample 150 nm in between (inset: Simulated cells inverse FFT of $CuWO_4$). (d) SEM image corresponding EDX mapping 150 nm in-between space for (e) Cu element, (f) O element, (g) W element and the $CuWO_4$ nanograin arrays were prepared by a electrodeposition and annealing in 550 ^{o}C.

The relevant in-between space distribution of the $CuWO_4$ nanograin arrays for 50, 100, 150 and 200 nm is respectively exhibited in Figure 7.4 (a1-a4). The space in between for $CuWO_4$ nanograin 50 nm is limited, ranging from 48 to 54 nm (Figure 7.4 a1). Meanwhile, for 100 nm, $CuWO_4$ nanograin arrays the distribution in between space is 94-102 nm, and for 150 nm is in the range of 148-152 nm, and the in-between space of $CuWO_4$ nanograin arrays in Figure 7.3 (a) is respectively limited to 198-202 nm. That means nanoimprinted AAO templates it really effective-technology to controlled the $CuWO_4$ as nanostructure as not reported before. The measurement of light absorber was conducted by using UV Vis spectrophotometric with in-between distance, but with the same deposition and heating parameters towards $CuWO_4$ nanograin arrays, as shown in Figure 7.4 (b). Hereby we present the optimum condition reached by each compartment as the foundation to recognize the improvement in PEC performance. The differences in-between spaces in CuWO4 nanograin arrays provide a good opportunity to optimize the light absorption capability. The absorption spectra of the prepared samples demonstrated in Figure 7.4 (b) is measured in the diffuse reflectance mode. If we compare to $CuWO_4$ nanograin arrays one another, there is a distinct absorption enhancement exhibited in the range of 300-620 nm, attributed to the anti-reflection characteristics owned by the $CuWO_4$ nanograin arrays structure. Additionally, in Figure 7.4b, the absorption spectra of $CuWO_4$ nanograin arrays included present the pronounced absorption in the visible area. The inclination of absorption occurs at around 500 nm for $CuWO_4$ nanograin arrays with in-between space 50 nm, and at 620 nm for $CuWO_4$ nanograin arrays with 150 nm in-between spaces, which indicates that absorptions range are originated from $CuWO_4$.

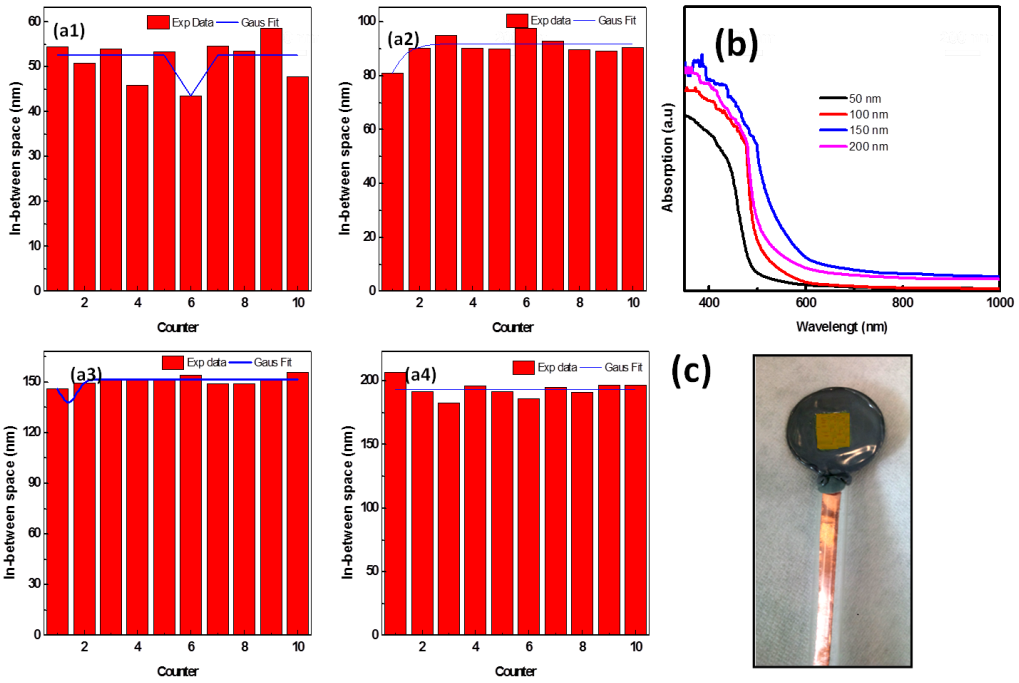

Figure 7.4 The relevant in-between space distributions of the $CuWO_4$ after the annealing treatment for different space: 50 nm (No. a1), 100 nm (No. a2), 150 nm (No. a3), and 200 nm (No. a4). b) Diffused reflectance UV-vis spectra of the 50 nm, 100 nm, 150 nm, and 200 nm, respectively. c) The photograph of the corresponding one sample 150 nm in-between space.

In order to find the maximum photogenerated carrier and minimum recombination carrier in $CuWO_4$ nanograin arrays for all samples with different in-between space, PEC measurement is conducted in photoanode $CuWO_4$ nanograin arrays as shown in Figure 7.4c. Measurement in working electrode $CuWO_4$ nanograin arrays is executed by determining three electrodes with Ag/AgCl as the reference electrodes, and Pt plate as counter electrode. As a note, all these measurements were conducted in 0.1 Na_2SO_4 (pH 6.8) neutral solution in which nitrogen gas was flowed-in for one hour before being utilized. This procedure was performed in order to minimize the effect of external bubble which is possible to occur during the measurement because of irradiation process. Figure

7.5a explicates the characteristics of the irradiation current density versus bias voltage interval (J-V) was measured at 20 mV/s between −0.2 V and 1.4 V versus Ag/AgCl, in dark and irradiation (AM 1.5G, 100 mW/cm^2) to $CuWO_4$ electrode on the sample with different in-between space and diameter inside (depicted with SEM Figure 7.2). From this illustration, it is clear that irradiation current increases in bias voltage positive measurement area, indicating that is n-type. As a comparison given in Appendix Figure 11.22, all measured samples showed the same behavior in positive areas. The fundamental difference can be seen from this measurement is the density magnitude of irradiation current at interval of 0 V to 0.4 V versus Ag/AgCl.

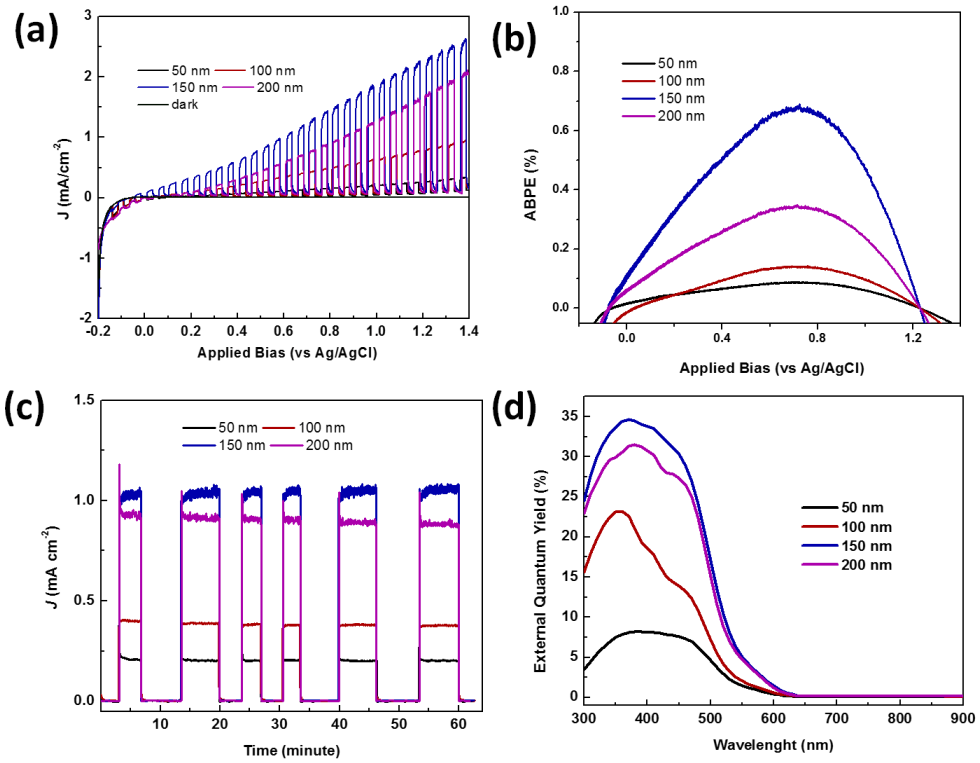

Figure 7.5 (a) Chopped light LSV of a CuWO4 photoanode in a three-electrode configuration described in the text and under AM 1.5G sunlight. The scans are collected from −0.2 to 1.4 V versus Ag/AgCl. (b) ABPEs of the relevant electrodes (a), (c) Amperometric J-t curves of the electrodes measured at 0.7 V versus Ag/AgCl with

chopped on–off cycles under AM 1.5G, (d) EQY of the electrodes measured without applying an applied bias.

As explicated before that the in-between space difference is predicted as the cause $CuWO_4$ nanograin arrays with wider space will make the charge carrier easier to do the transfer and recombination. This also can be seen from the value of irradiation current density on dynamic bias voltage. On Figure 7.5 (c), it can be clearly demonstrated that the irradiation current density highly depends on the in-between space. Where the peak of irradiation current density occurs at 0.22, 0.41, 1.02 and 0.88 mA/cm^2 (vs Ag/AgCl) , for 50 nm, 100 nm, 150 nm and 200 nm, respectively, is measured at thermodynamic bias voltage, which is on 60 minutes of deposition duration which in-between space 150 nm. The reason we can provide here is because after that there was a decrease in irradiation current density because $CuWO_4$ particle resulted from deposition has exceeded the nanoimprinted AAO template height, therefore at the end will be tangent or the membrane which become the carrier recombination barrier will appear. Optically, in this membrane density, part of incoming irradiation light was not absorbed but was reflected, or in other words the membrane creates an interface which minimize the efficiency of incoming irradiation light mode.[198]

Another possibility is the coupling between one $CuWO_4$ nanograin arrays particle to another, providing a transient drift effect between standing part current direction and membrane, which caused the decrease in irradiation current density. In other part, the additional TiO_2 (E_{gap} 3.2 eV) protection layer with atomic layer deposition [206] is aimed to increase the absorption capacity of light spectrum in $CuWO_4$ nanograin arrays, even though the reachable maximum value by using this mineral to convert solar irradiation into hydrogen is only up to 3%[206] due to the wide energy gap between these both materials. Nonetheless, Au nanoparticles integrated inside contributes an effect of surface

plasmon resonance (SPR), as found by Hales et. al. that magnitude of SPR effect depends on the size, morphology, and density of Au nanoparticle itself. Au nanoparticle was also used as conductor for Au nanoparticle deposition in the beginning of preparation (please refer to scheme in Figure 7.1). As a comparison, Appendix Figure 11.22 is displayed to show the value of photogenerate in thin film $CuWO_4$. The thin film of $CuWO_4$ deposited to FTO glass with valid mechanism is equal to the growth method in nanograin arrays. As the measurement of photogenerate in $CuWO_4$, thin film is conducted in the same electrolyte in addition to range limitation of applied bias. It is clearly demonstrated in the Figure Appendix Figure 11.22 that the maximum irradiation current at bias voltage density on thermodynamic applied bias (0.74 mA/cm^2), that is lower than the same measurement to nanograin arrays compartment because of hole injection on $CuWO_4$-electrolyte thin films, as well as the weak carrier current which enables to make this $CuWO_4$ thin film to have smaller performance towards PEC measurement.

From the discussion of the irradiation current density, theoretically we can measure the degree of efficiency of η irradiation conversion (applied bias photon to current efficiency, ABPE as show in Figure 7.5 (b) from $CuWO_4$ nanograin arrays electrode with bias voltage by using equation[206,207] $\eta = J(1.23 - V_{app})/ P_{light}$ where V_{app} applied bias Vs Ag/AgCl, J is external current measurement density, dan P_{light} is irradiation power density. The measurement result is presented in Figure 7.5 (b). with space in-between of 50 nm, 100 nm, 150 nm, and 200 nm each is 6.81 V s Ag/AgCl), 6.83 Vs Ag/AgCl), 7.12 Vs Ag/AgCl), and 7.11 Vs Ag/AgCl), organized in sequence. Moreover, from the figure, it can be clearly explicated that electrode optimum space is at 150 nm. This result also consistently occurred to samples with protection layer deposition. As consequence, the $CuWO_4$ nanograin arrays have wider surface and in direct contact with electrolyte as an electron conductor easily from interface, and will immediately do the charge transfer.

Nevertheless, too close or too far distance of space between two diamagnetic (mix of Cu-O and WO_3) $CuWO_4$ nanograin arrays will significantly influence the generated electric field.[208] Hence, optimum in-between distance has a significant impact on diamagnetic material. Qualitatively it can be interpreted that polarization through induction and non-barrier current within the magnetic field orbit will influence the efficiency of irradiation conversion. As seen from Figure 7.5 (c), the characteristic of chopped under AM 1.5G irradiation towards $CuWO_4$ nanograin arrays appears to be relatively stable in 60 minutes and in dark condition. Where this irradiation current shows mA/cm^2 1.02 mA/cm^2 at 0.7 V Vs Ag/AgCl, the highest result present as compared to previous report as show in Appendix Table 11.2 as the comparison displays the result values of irradiation current measurement for $CuWO_4$ thin films. This verifies our hypothesis that photoanode $CuWO_4$ nanograin arrays provide significant effect towards photogenerate. This indicates that the $CuWO_4$ present the photon absorption and collection via the band gap transitions of between electrodes. The highest value comes from the in-between space 150 nm electrode, in consistent with the highest absorption curve in Figure 7.4 (b).

The spectrum as the result of EQY (%) towards $CuWO_4$ nanograin arrays electrode in every sample was conducted without applied bias voltage as shown in Figure 7.5 (d). Around wavelength of 410 nm, the peak of photon-to-current efficiency appears for all samples, yet as explained previously that the influence of in-between space of two $CuWO_4$ nanograin arrays seems to be real. Too close the in-between space distance also significantly contributes to the decrease of the efficiency measurement. From this point, photon absorption on electrode is effective in relatively wide wavelength interval in visible area, which is from 300 nm to 620 nm. This is agreed well with the result indicated in Figure 7.5 (b). The two spectra possess an absorption onset at 300 nm.

Therefore, one of the ways to improve the efficiency on this mineral is by minimizing the polycrystalline.

To explain further on the electronic structure of this composite, Mott-Schottky (M-S) equation is relevant in this work by applying electrochemical impedance at frequency 1 Hz aim 1 MHz on voltage interval −0.4 V to +0.7 V (vs Ag/AgCl). The capacitance value of this measurement, which is calculated at 1 kHz as presented in Figure 7.6a, and show us the Mott–Schottky plot of the PEC electrode based on $CuWO_4$ nanograin arrays. The linear profile and the positive slope yield a typical n-type feature of the prepared material. This data is then used in M-S relation. The typical of potential of flat-band V_{FB} is between 0.2 V Vs Ag/AgCl to −0.19 Vs Ag/AgCl, correspond to the previous report.[207,214] From the result, we retrieved each flat band voltage with different values [203-204,208] on open-voltage series below 1.5G illumination −0.16 V (vs Ag/AgCl), −0.14 V (vs Ag/AgCl), −0.104 V (vs Ag/AgCl) and 0.46 V(vs Ag/AgCl), for 50 nm, 100 nm, 150, and 200 nm, respectively, in sequence for each electrode with in-between space difference. Afterwards, the density of majority carrier is calculated from the slope by using equation $d(C_{sc}^{-2})/dE = 2/ e\varepsilon_o\varepsilon N_D$ (using dielectric constant 83[207] for $CuWO_4$ and the effective mass of electron 70). From the mentioned calculation, there are 0.84 $x10^{20}$ cm^{-3}, 0.97 $x10^{20}$ cm^{-3}, 2.86 $x10^{20}$ cm^{-3}, and 1.35 $x10^{20}$ cm^{-3}, respectively, each in sequence. Noted that the value of the charge-majority carrier is higher than the reported before.[206,207]. The figure also clearly explicated that this $CuWO_4$ nanograin arrays has behavior from n-type conductivity and highest value from charge-majority carrier is the sample with in-between distance of 150 nm. As exhibited in the inset of Figure 7.6a, Nyquist plots measured in the frequency range of 10^6 Hz to 1 mHz at the bias of 0 V vs. Ag/AgCl for the two sets of PEC electrodes are shown insert, given that the semicircle in a Nyquist plot at high frequencies is characteristic of the charge transfer process. And the diameter

of the semicircle is estimated to be equal to the charge transfer resistance.[222] This series of electrochemical measurements illustrates that modification of nanograin arrays is able to positively impact the electronic properties of $CuWO_4$, by increasing the doping density and enlarging the band bending at the interface with electrolyte. The reduced charge transfer resistance are beneficial for promoting the separation and transfer of the photo-generated charge carriers, indicates a higher efficiency for the utilization of photo-generated charges in $CuWO_4$ nanograin arrays than thin films.

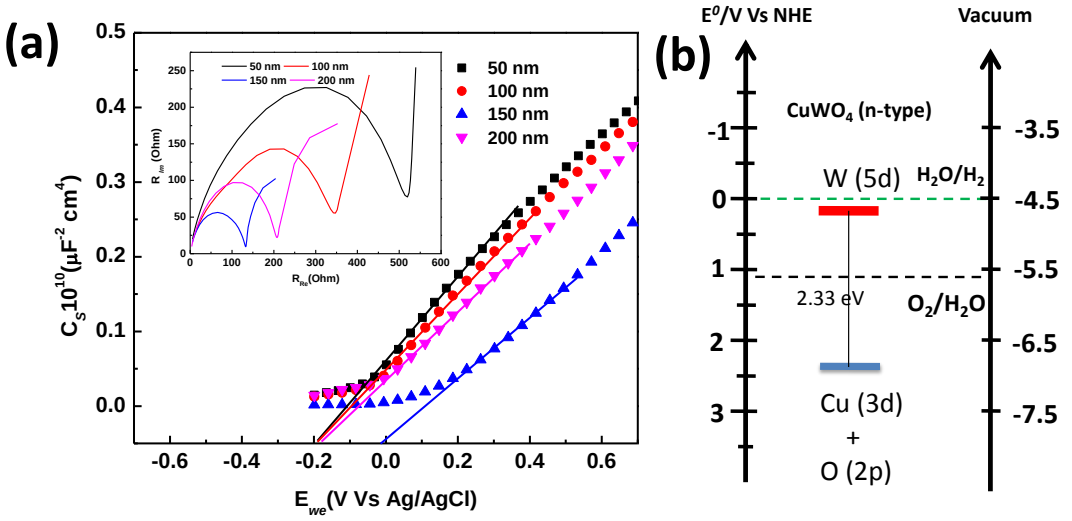

Figure 7.6 (a) Mott−Schottky plots obtained from SPEIS measurements with Nyquist plots as the inset, (b) Energy level schematic of $CuWO_4$

Additionally, the precise band gap structure of the grown $CuWO_4$ nanograin arrays to the band gap values derived from the Tauc plot are demonstrated in Figure 7.6 (b). Referring to the standard reduction as well as oxidation potentials of water splitting reaction, as those potentials are just in between the valence band position and conduction band position of $CuWO_4$ nanograin arrays, make it an ideal material for water splitting. Practically, the short distance between the Fermi level and the valence band position indicates a n-type feature of the as-grown $CuWO_4$ nanograin arrays. The estimated band

gap value herein is slightly lower that of reported values, which can be attributed to the material's defects.[216] Meanwhile, the positions of energy power are determined under vacuum conditions with surface defects removed by ion milling procedures. These create a difference compared to the band gap positions measured by the electrochemical technique.

The result from this efficiency spectrum is in accordance to the result of absorption spectrum in this $CuWO_4$ nanograin arrays electrode. For another side, in order to comprehend more thoroughly on the interaction between photon and $CuWO_4$ nanograin arrays, simulation from FDTD) is exhibited in Figure 7.7. This simulation is specified to find out electric field distribution around top view-sectional nanostructure appearance when sample is irradiated by photon with wavelength of 410 nm. It is observed when in-between space of nanograin is narrower; the near-field coupling oscillation strength creates a robust confinement of the local electric field that intensifies the spectroscopic signals. This impact, resulted from the distribution of the nanograin, is in concordance with the observation on nano-metal particle arrays. As explicated by Jain et. al.[226] that within the dipolar coupling model, the distance decay of plasmon coupling was independent of the metal type, the nanoparticle shape, and the medium of dielectric constant. To analysis further, the near-field intensity enhancements demonstrate a fast decay with the gap inclination of the nanograin. It indicates that when the nanograin distribution is tuned sparse, the coupling of the electric field is getting weak. This weakened coupling could be the reason for the corresponding band gap shift of $CuWO_4$ nanograin arrays. Likewise the band gap shift of $CuWO_4$ nanograin arrays, claimed that such band gap shift could be realized by adjusting the in-between space $CuWO_4$ nanograin in the range of 150 nm to 200 nm, as based on the conventional quantum confinement effect. Nevertheless, our results indicate that the band gap shift can also be

obtained only by adjusting the diameters and the in-between space of $CuWO_4$ nanograin arrays; these parameters are even larger than the Bohr radius of $CuWO_4$ nanograin arrays. Our results also indicate that because the thicknesses of these $CuWO_4$ nanograin arrays are equal, quantum effects and thus not responsible for this observation. This specific optical band gap shift is attributed to the interaction of the incident radiations with the highly ordered nanostructure arrays, and the tenability of the band gap is correlated to the strength of the near field enhancement of light. This section exists to widen the tuning range of optical properties of nanostructure arrays and the possibilities of photoelectronic applications. This can explain the influence of photon interaction and $CuWO_4$ nanograin arrays with different sample geometric in-between space parameter by identifying the intensity of electric field to measure optimum in-between space which influences electric field distribution of $CuWO_4$ nanograin arrays. Furthermore, this observation involved top view-section dimension in-between two $CuWO_4$ nanograin arrays, antianode distribution spectrum indicated along the diagonal section which splits the $CuWO_4$ nanograin arrays structure, where the wider the in-between space of two $CuWO_4$ nanograin array, the weaker the electric field. Conversely, the closer the in-between distance between two $CuWO_4$ nanograin arrays, the stronger the electric field will be. However, it needs to be understood that the distance of electric field generated from two nanograin will influence the magnetic field which also impacts on the electrolyte penetration as the electron carrier, thus it is necessary to have an adequate in-between distance in accordance to the band gap which enable to improve PEC performance. Therefore, based on the observation from irradiation current and the EQY (%) characteristics, it can be concluded that the in-between space in $CuWO_4$ nanograin arrays explains that there is a significant increase occurs between $CuWO_4$ nanograin arrays towards $CuWO_4$ photoanode of thin films.

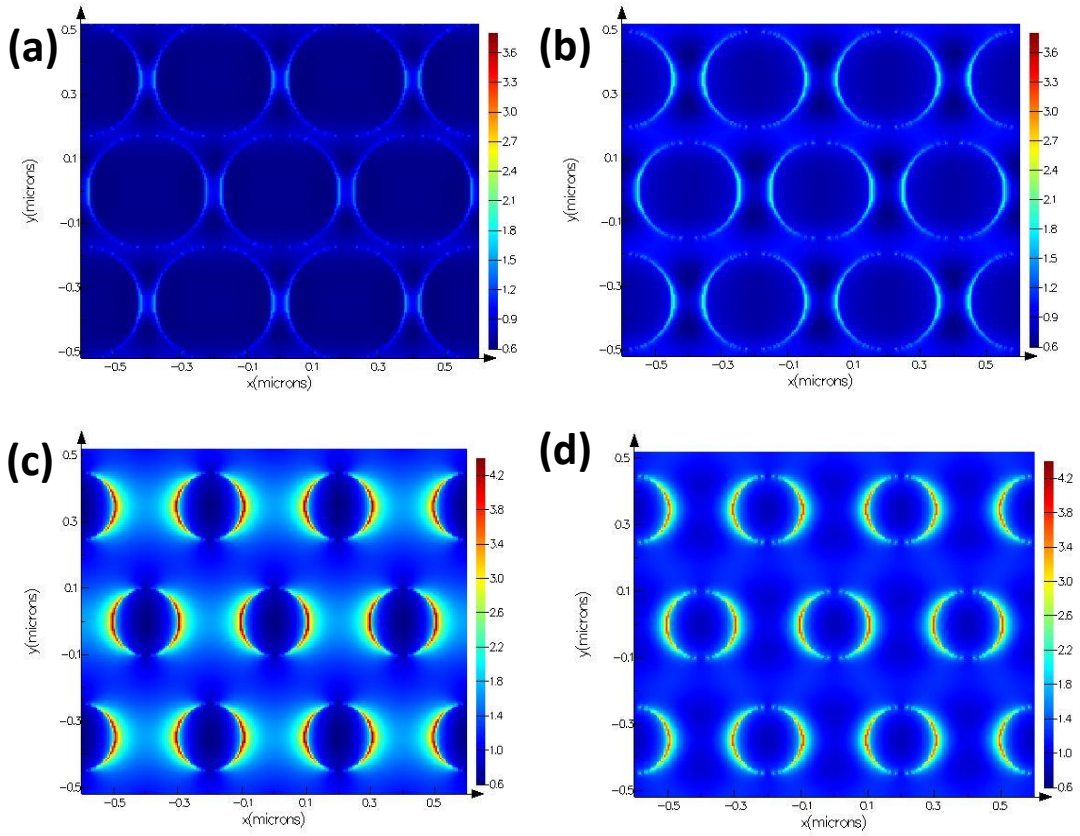

Figure 7.7 Simulated cross-sectional EM wave distributions of the $CuWO_4$ nanograin arrays at the wavelength 420 nm of in-between space (a) 50 nm, (b) 100 nm, (c) 150 nm, and (d) 200 nm, respectively.

Chapter 8. Nanoarrays: Realizing Super-long Cu_2O Nanowires Arrays for High-efficient Water Splitting Applications with a Convenient Approach

8.1 Introduction

Fujishima and Honda reported hydrogen generation in a PEC water splitting cell using a TiO_2 electrode in 1972.[91] The conversion of solar energy to chemical fuels like H_2 is a highly feasible approach to solve world-wide sustainable energy challenges. However, as frequently discussed, until now, the reported efficiencies remain too low to be practical.[46,227–230] To solve this problem, building novel morphologies has been an effective method in fundamentally improving the performance of solar water splitting, on the basis of their unique geometry and size- and shape-dependent characteristics. Nanowire, as a typical nano-structure, has been successfully manufactured in various semiconductors for enhancing the PEC performances, such as TiO_2, ZnO.[231]

Cu_2O, with a direct band gap of ~2.1 eV, has long been regarded as an attractive candidate for solar energy conversion, with a theoretical maximum photocurrent of 15 mA cm^{-2} and 18% solar-to-hydrogen conversion efficiency under AM 1.5 illumination.[99,125,164,230,232] In addition to the p-type materials, copper is abundant and the material can be processed by industrially proven, low-cost methods.[164] Recently, the highly active photocathode of Cu_2O thin films, which can reach the high photocurrents of ~7.6 mA cm^{-2} at a potential of 0 V vs. RHE and maintained active for 1 h of testing, was proposed.[99] In our previous work, we reported an efficient surface treatment for Cu_2O photocathodes using trisodium citrate to realize an impressive PEC performance.[100] These results demonstrate the significant potential for Cu_2O in PEC water splitting. In particular, for efficiency improvement, various Cu_2O nanostructures with high surface-to-volume ratio and short diffusion lengths for charge carrier transport compared with bulk materials, have been successfully fabricated, including nanorods, nanowires (NWs),

nanotubes, nanocubes, and nanospheres.[233–236] However, super-long Cu_2O NWs arrays, have been not well reported, for PEC water decomposition. In this work, we synthesize successfully super-long Cu_2O NWs arrays by the convenient and low-cost anodic alumina oxide (AAO) template technology. In comparison with the photocathode based on Cu_2O films, the super-long Cu_2O NWs photocathode presents a remarkable improvement in photocurrent, from 1.00 mA cm^{-2} to 2.75 mA cm^{-2} at 0.8 V vs Ag/AgCl. After optimizing the photoelectrochemical system by depositing Pt NPs with atomic layer deposition on the Cu_2O NWs, the plateau photocurrent has been improved to 7.00 mA cm^{-2} at 0.8 V vs Ag/AgCl and the EQY is up to 34% at 410 nm. The results from this study provide a low-cost, naturally abundant nanowire material for use in photoelectrochemical cells.

8.2 Experimental

Growth of Cu_2O NWs and films: AAO templates were synthesized from high purity aluminum foils by a two-step anodization process at 40 V in 0.3 M oxalic acid with a 8 h time first and 1 h second anodization time.[237,238] The AAO pores were widened in a 5 wt% H_3PO_4 solution for 50 min at 30 °C. Subsequently, a thin layer of gold (25 nm) was deposited by PVD. After that, thick Ni film was deposited on the upper surface of AAO with a current density of 5 mA cm^{-2}. The Ni plating solution contains $NiSO_4$ (0.38 M), $NiCl_2$ (0.12 M), and H_3BO_3 (0.5 M). The gold coated AAO template was used as the working electrode, and Ni foil was the counter electrode. Then, backside alumina was removed with $CuCl_2$ solution, and Ni layer with AAO was obtained. Then, the sample was kept in H_3PO_4 (5%) during 30 minute in 60 °C to remove barrier layer before deposition Cu_2O. Finally, Cu_2O NWs were cathodically electrodeposited from a 0.4 M copper sulphate bath containing 3 M lactic acid. The pH value of the bath was carefully adjusted to 12.0 by the addition of 3 M sodium hydroxide. Cu_2O NWs were grown at a constant potential of −0.40 V vs Ag/AgCl in a normal three-electrode configuration for a

nominal duration of 60 minute. The temperature of the bath was controlled at 45 °C using a heating plate with an in situ temperature probe. After deposition, the AAO ordered pore skeleton was removed by immersion in 0.1 M NaOH aqueous solution aim time 1 hours and Cu_2O ordered nanowires were thus obtained. For comparison, we also prepared Cu_2O thin films on FTO/Au directly using the same procedure.

Fabrication of Cu_2O NWs and films photocathodes: A strip of conductive copper tape was stuck on the exposed Ni and FTO part of the Ni/Cu_2O NWs and FTO/Au/Cu_2O, respectively, which is to extend the conducting circuit. The copper tape was then threaded through a glass tube and then sealed with an insulating epoxy. Electrode areas were optically measured as 0.2 cm^2.

Photoelectrochemical measurements: External quantum yield was measured with an Oriel 150 W Xe arc lamp (Newport) and a quarter-turn single-grating monochromator (Newport). Sample measurements were recorded with chopped illumination. The output current signal was connected to a Merlin digital lock-in radiometry system and the output signal from the lock–in amplifier was fed into a computer controlled by TRACQ BASIC software. Current–potential plots and impedance characterization were measured using the digital BioLogic potentiostat (SP-200) and 0.1 M sodium sulphate aqueous solution served as the electrolyte. A Pt counter electrode and Ag/AgCl reference electrode were used during the measurements. A standard 300 W Xe lamp (Newport) served as the light source and the light intensity was characterized to 100 mW cm^{-2} by a Si photodiode (Newport).

Characterizations: Powder X-ray diffraction (XRD) pattern was recorded on Bruker D8 Advance equipped with graphite monochromatized high-intensity Cu Kα radiation (λ = 1.54178 Å). The scanning electron microscopy (SEM) images were obtained by S4800

HITACHI (Japan) scanning electron microscope. Room–temperature UV-Vis absorption spectroscopy was measured using Varian Cary 5000 UV-Vis-NIR spectrophotometer.

8.3 Results and discussion

The strategy for the growth of the Cu_2O NWs can be divided into five detailed procedures that are illustrated schematically in Figure 8.1, where the colors of the imprinted AAO template, Al, Au, Ni and Cu_2O are described as blue, gray, yellow, black and orange, respectively. The process includes gold layer deposition (I), Ni electrodeposition (II), aluminum and barrier layer removal (III), Cu_2O growth (IV), and template removal (V). The imprinted AAO template was adopted as the master templates in the preparation process because of its attractive advantages, including uniform and highly oriented nanoporous structures, tunable structural parameters, large area, low cost, and excellent thermal and mechanical stability.[236–239]

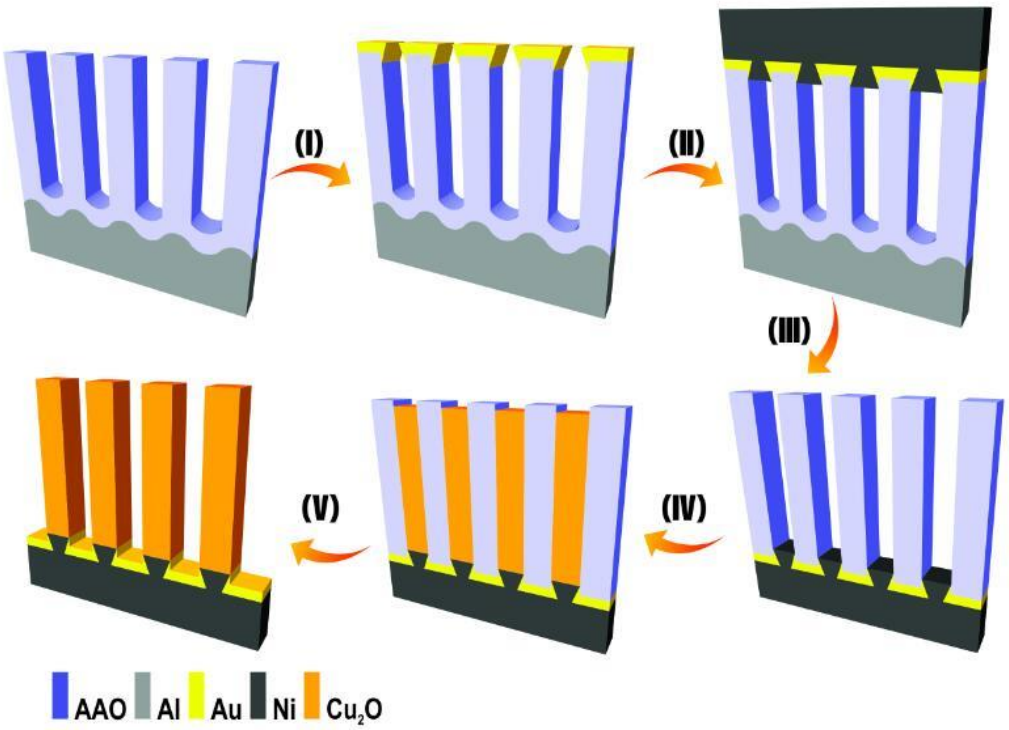

Figure 8.1 Schematic illustration of the fabrication process of Cu_2O NWs with AAO template: gold layer deposition (I), Ni electrodeposition (II), aluminum and barrier layer removal (III), Cu_2O growth (IV), and template removal (V).

Figure 8.2 (a) clearly illustrates that the bare AAO template, which was fabricated with two times oxidization,[237,238] presents quite well-distributed nanopores with a diameter of around 20 nm and a length of around 5 um. The electrodeposition for Cu_2O NWs and films were both performed in a copper sulphate bath containing 3 M lactic acid, by following the previously reported processes.[100] Figure 8.2 (b) shows the representative scanning electron microscopic images of the prepared nanowires on nano-Ni substrates. The nanowires are vertically well aligned on the substrate. The size of these nanowires is gauged as ~ 4.5 μm in length and ~ 85 nm in diameter, respectively. The films grown on Au/FTO glass are constructed by continuously distributed polyhedral particles, and the configuration turns out to be cuboid, as shown in Figure 8.2c.[100] In addition, consistent with the reported values,[100] the band gap of the grown Cu_2O films on

Au/FTO glass is characterized as 2.1 eV by the absorption analyses shown in experiment Chapter 2.

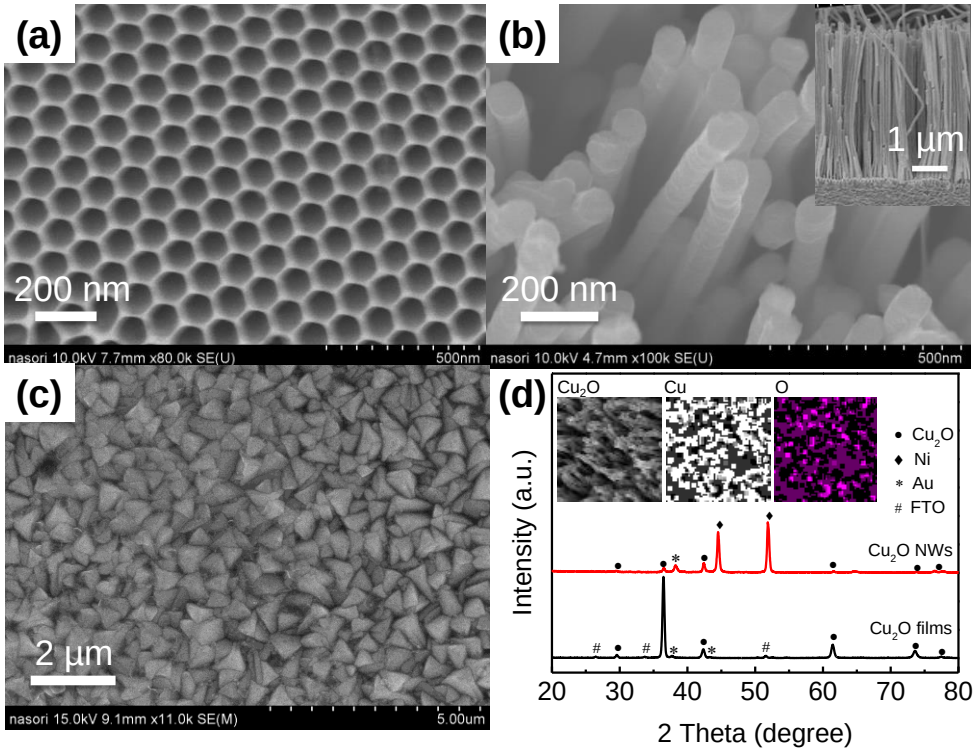

Figure 8.2 Top view SEM images of the prepared AAO template (a), Cu_2O NWs (b) (inset is cross-sectional SEM image of Cu_2O NWs) and Cu_2O films (c). (d) XRD patterns of Cu_2O NWs and films (inset is mapping of Cu_2O NWs).

The XRD patterns of the Cu_2O NWs and thin films are given in Figure 8.2 (d), where the diffraction peaks at 29.6^o, 36.5^o, 42.4^o, 61.4^o and 73.6^o can be doubtlessly ascribed to the reflection of (110), (111), (200), (220) and (311) planes of Cu_2O (JCPDS card No. 05-0667).[126] Phases of CuO and Cu are not discernible, implying a pure Cu_2O structure in the nanowires and films. In order to further determine the composition of the material elements, we characterized the mapping of Cu_2O NWs with SEM, as shown inset of Figure 8.2 (d), which confirms that only Cu and O elements are present in the nanowires.

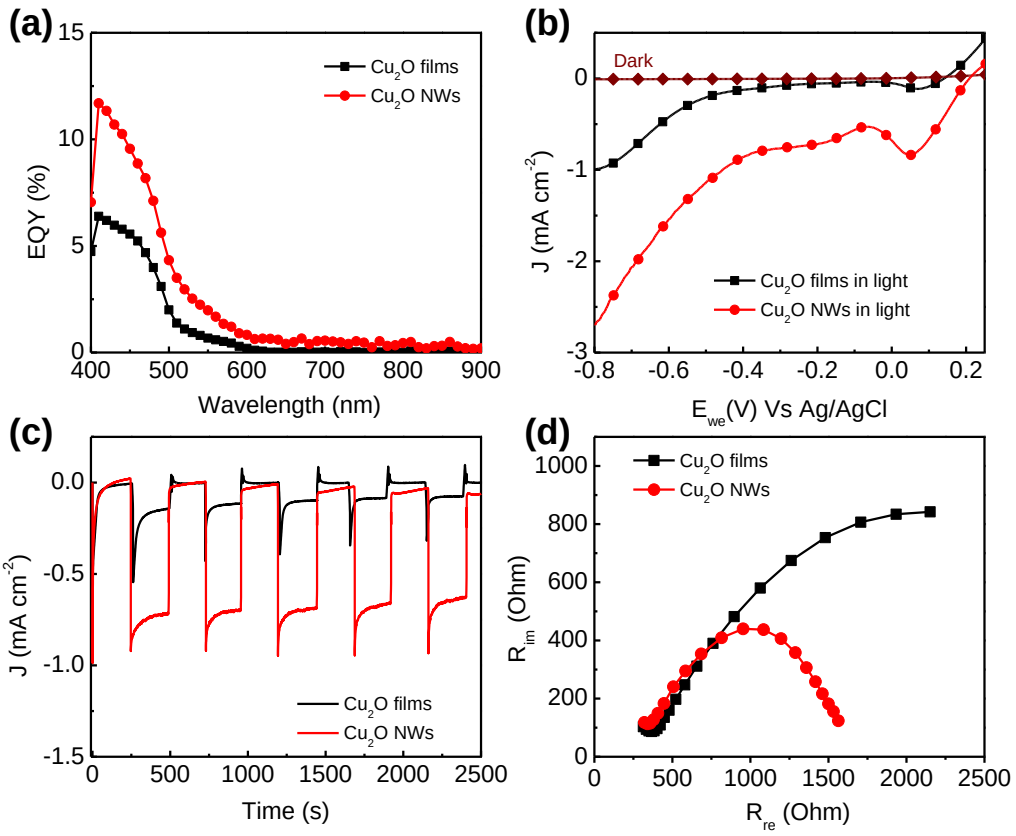

Figure 8.3 (a) EQY (%) spectra, (b) photocurrent-potential profiles, (c) time-dependent photocurrent density spectra and (d) Impedance spectra of the Cu_2O NWs and films photoelectrode.

Figure 8.3 (a) demonstrates the representative steady-state EQY spectra of PEC electrodes of Cu_2O NWs and films. Comparing to Cu_2O thin film photoelectrode, the Cu_2O NWs photoelectrode on the nano-Ni exhibits an increscent EQY below the absorption threshold of Cu_2O (600 nm). An enhancement of 2-fold is obtained, indicating that Cu_2O NWs based electrode has a larger photo-to-current efficiency than that with Cu_2O thin films. This result is consistent with those reported in recent studies that have focused on the outstanding optical and electrical properties of nanowires and improvement in photocatalytic performance of semiconductor nanowires.[240,241]

Photocurrent−potential profiles were tested by soaking the photoelectrodes into 0.1 M Na_2SO_4 aqueous solutions, with Ag/AgCl as the reference electrode and a Pt wire as the counter electrode. Each plot represents a typical photo-response obtained under white-light illumination (AM1.5G, 100 mW cm^{-2}), as illustrated in Figure 8.3 (b). These J-V curves exhibit a cathodic photocurrent and indicate a distinct p-type feature of both prepared Cu_2O NWs and films, being consistent with our previous report.[100] In the system, photo-induced electrons move from films and nanowires to electrolyte to drive PEC reactions, and the corresponding holes transport from films and nanowires to ITO electrode during the PEC measurement. Compared to the Cu_2O films electrode, the photocathode of Cu_2O NWs possesses a remarkable improvement in PEC performance, being in good agreement with EQY measurement. To be noted, both Cu_2O films and NWs photoelectrode have the photoreduction peak at 0 V vs Ag/AgCl, owing to the weak chemical stabilization of Cu_2O, which is consistent with other literature reported.[100]

As illustrated in Figure 8.3 (c), to investigate the samples PEC performance and stability under visible light, the time-dependent photocurrent density was carried out on the Cu_2O NWs and films during repeated on–off visible light illumination cycles at -0.3 V vs. Ag/AgCl. The results show that both samples exhibit fast and reproducible photocurrent responses upon each illumination. The plateau photocurrent density of the Cu_2O films electrode was 0.11 mA cm^{-2}, while that of the Cu_2O NWs was 0.71 mA cm^{-2}, which represents a more than 500% increase from the Cu_2O films. The result demonstrates that nanostructure of materials can achieve the improvement of the photoelectric conversion, due to the capability of offering large surface area and more reaction sites, decoupling light absorption and charge carrier collection, shorting carrier diffusion distance compared to the bulk structures.[242,243]

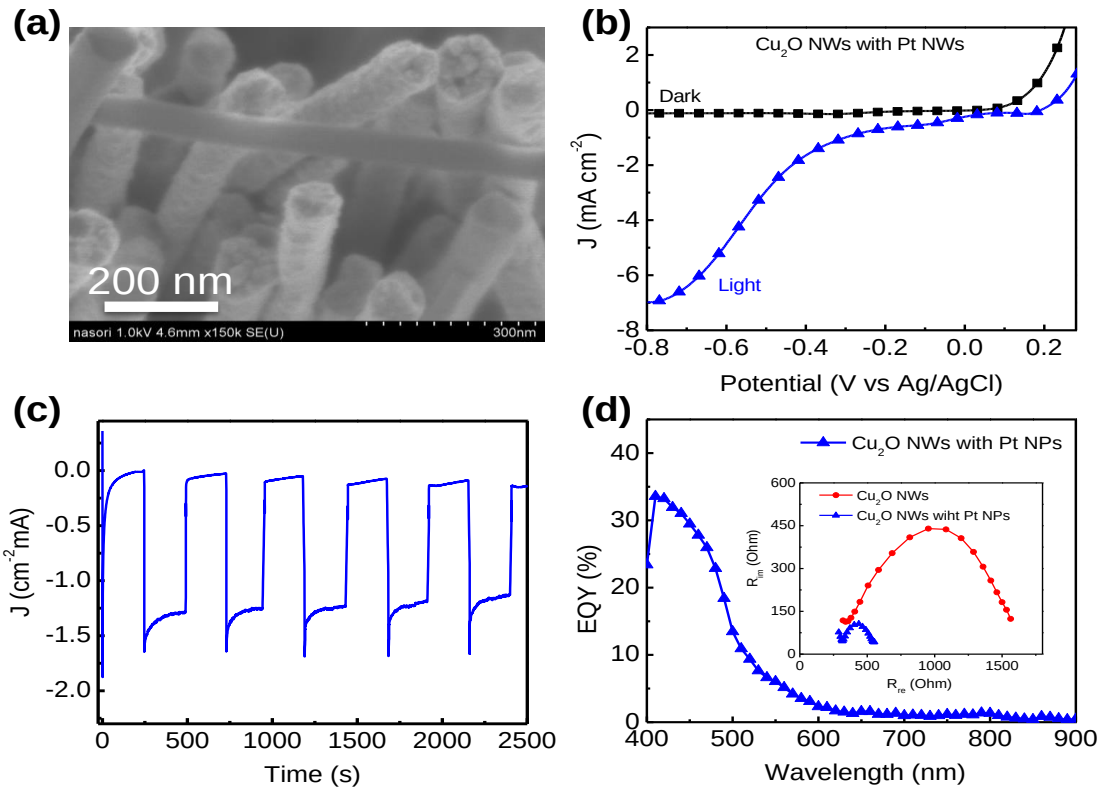

Figure 8.4 (a) Top view SEM image of Cu_2O NWs with Pt NPs, (b) photocurrent-potential curves (inset is the photocurrent-time profile of the photoelectrode and (c) Curves of the time-dependent photocurrent measured for Cu_2O NWs with Pt NPs (applied −0,3 V Vs Ag/AgCl) (d) EQY spectra of the photoelectrode (inset is impedance spectra).

To elucidate the strong correlation between nanostructures and the enhanced photocurrent and EQY values, electrochemical impedance measurement was carried out. Figure 8.3 (d) shows Nyquist Impedance spectra of Cu_2O NWs and films at DC frequency from 200 kHz to 200 Hz, which was performed at open circuit voltage. Charge transfer resistance (R_{ct}) from the photoelectrodes to redox species in the electrolyte can be calculated by fitting the semi-arc in the 1 kHz region.[122,123,] Smaller circular radius represents a lower electron transport resistance and higher separation efficiency of the photo-generated electrons and holes. As can be seen from Figure 8.3 (d), the R_{ct} of Cu_2O NWs electrode is much smaller than that of Cu_2O film sample, indicating a much smaller

electron transport resistance and a larger photo response, leading to a larger photocurrent in Cu_2O NWs electrode.

To further promote the PEC performance of the Cu_2O nano-device, Pt NPs were deposited on the nanowire surroundings as the catalyst via an atomic layer deposition procedure.[245,246] Figure 8.4 (a) shows the top view SEM image of the prepared catalyst on Cu_2O NWs, where the size of the particles could be gauged as 5 aim 10 nm, and Pt NPs on the surface of Cu_2O NWs are of high density. The photocurrent-potential curves of the advanced photocathode are given in Figure 8.4(b). By comparing with the bare Cu_2O NWs electrode, the one equipped with Pt catalyst has a positive improvement in photocurrent, which is amplified to 7 mA cm^{-2}. Moreover, the photocurrent-time profile of the photoelectrode at −0.3 V vs Ag/AgCl (Figure 8.4 (c)) shows that there is no obvious decline in the current density after several light–dark cycles within a time span of about 2500 s. It is surprising that, by modifying the Cu_2O NWs surface with Pt NPs, the EQY is amplified to 34%, which is 2-fold of the bare Cu_2O NWs and 4-fold of Cu_2O films, thus showing a great potential of applying Cu_2O in water reduction, as shown in Figure 8.4 (c).

To shed light on the enhancement mechanism of PEC performance in Cu_2O NWs with Pt NPs, the schematic illustration of Cu_2O NWs/Pt photoelectrode and the whole band energy diagram of the Cu_2O/Pt/electrolyte structure are schematically proposed in Figure 8.5. The band bending of Cu_2O/Pt/electrolyte is similar to the case for p-Si/Pt/ electrolyte contact in a photoelectrochemical cell[242], in which Fermi level is split into quasi-Fermi level $E_{F,n}$ and $E_{F,p}$ by photogeneration of excess carriers and by forward bias. There is the reaction products are withdrawn from the cell to be marked elsewhere to provide electrical power. Such a cell might be operated at short-circuit or a small applied bias to provide the necessary potential within the electrolyte. In here, that was assuming

all the absorption in the Cu_2O NWs for the moment in quasi-neutral region. Photon absorbed by Cu_2O NWs generates minority carrier (electron), which drifts to semiconductor/electrolyte interface where water was decomposed ($H_3O^+ \rightarrow H_2$). The Pt NPs, which maximize the surface area and specific activity of the precious metal catalyst,[247] function as an electrocatalyst for the photocathodic reaction (H_2 generation).

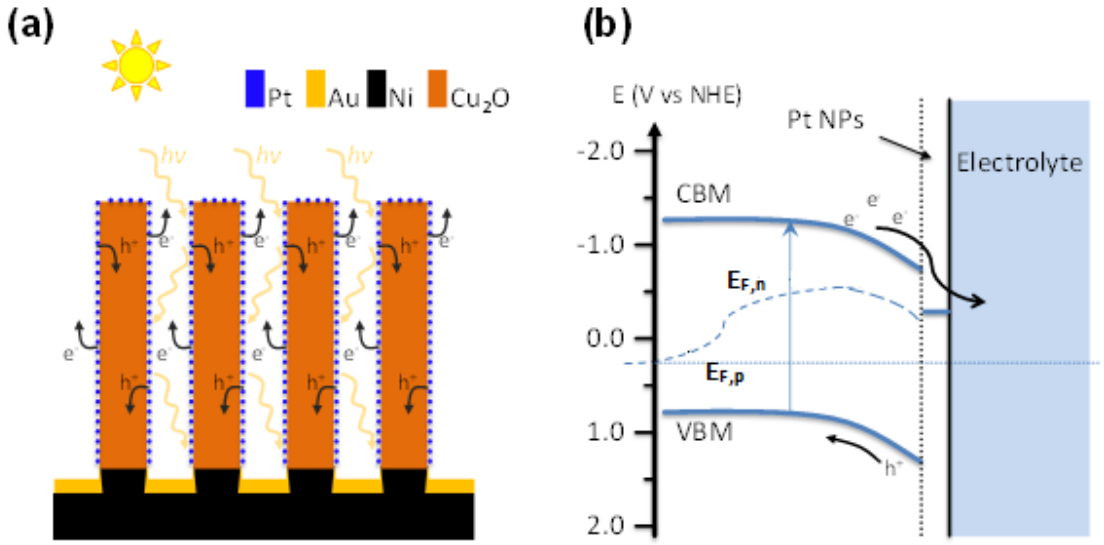

Figure 8.5 (a) Schematic illustration of Cu_2O NWs/Pt photoelectrode, (b) schematic representation of energy band-gap alignment of the Cu_2O NWs with/without Pt NPs

Chapter 9. Summary and Outlook

In order to enhance the efficiency of PECs, this dissertation proposed new methodologies for the development of very efficient photoeelctrodes based on metal oxides. Firstly, an effective method is demonstrated to synthesize advanced CBO thin films on FTO/Au substrates. Through a series of systematical investigations, it has been revealed that the presence of Au is beneficial for improving the crystal quality of material, promoting the separation of photo-generated charges and reducing the resistance of the system. Consequently, the plateau photocurrent has been enhanced dramatically from −0.23 mA cm^{-2} to −0.50 mA cm^{-2}, which is more than two times higher than the reported values. By modifying these advanced films with Pt catalyst, the photocurrent can be further amplified to reach a value that is over −1.2 mA cm^{-2}.

Secondly, a simple surface treatment approach was developed for Cu_2O based photocathodes to enhance PEC performance. The adopted TSC is beneficial for fixing Cu (II) impurities, hence increasing the doping density of Cu_2O films and conducting the photo-generated charge carriers to the interface with electrolyte. Accordingly, a great improvement in photocurrent and EQY is achieved. Thus, this part offers a cost-effective methodology to optimize the overall efficiency of solar energy conversion systems that utilize Cu_2O as light-harvesting component.

Thirdly, polycrystalline BFO photoelectrodes fabricated using typical spin-coating technology. Due to the distinct ferroelectric performance, orientations of BFO band bending at BFO/electrolyte could be switched from upwards to downwards by poling pretreatments. Subsequently, charge transfer directions of photo-exited charges either generated in the BFO or in the surface modifiers like molecular dyes and CdSe quantum

dots were tuned, as demonstrated by systematic steady-state photoelectrochemical investigations. This study provides an opportunity to manipulate photoelectrochemical reactions on a BFO-based ferroelectric photoelectrode and also an insight on the strategies for designing smart photoelectrochemical systems.

Finally, $CuWO_4$ nanograin arrays and Cu_2O NWs are successfully realized by utilizing AAO templates. The difference in-between distance of $CuWO_4$ nanograin in the array is successfully controlled by using AAO templates. As $CuWO_4$ nanograin array based photoelectrodes possess optimal width for the maximal penetration between surface and electrolyte as photon absorber, $CuWO_4$ nanograin array based photoelectrodes shows high current density (1.01 mA cm^{-2}) compared to thin film based photoelectrodes (0.23 mA cm^{-2}). APBE calculation also showed similar trend. Moreover, EQY measurement supports the assumption that nanograin arrays are highly effective for the distribution of electron generator compared to the thin films. On the other hand, a novel photocathode based on super-long Cu_2O NWs showed high photocurrent (–2.75 mA cm^{-2}) compared photocathode based on Cu_2O thin films (–1.00 mA cm^{-2}) due to the advantages high specific surface area, light-trapping and short carriers transfer of the nanowire based electrodes. After the optimized deposition of Pt NPs on the Cu_2O NWs via atomic layer deposition, the photocurrent plateau has been further amplified to 7 mA cm^{-2}. The result from this study provides an opportunity to utilize low-cost and naturally abundant material for application in photoelectrochemical cells.

To conclude, this dissertation proposed promising methodologies for the fabrication of p-type and n-type photoelectrodes to develop highly efficient photoelectrochemical water splitting devices. This in turn makes a positive contribution in addressing the world-wide energy requirements. Furthermore, our high dependency on complex and expensive

technologies for the development efficient photoelectrodes can be reduced by adopting the methodologies demonstrated in this treatise.

Chapter 10. Bibliography

[1] Y. J. Cheng, S.H. Yang, C.S. Hsu, Chem. Rev. 109, 2009, 5868–5923.

[2] J. Ronge, T. Bosserez, D. Martel, C. Nervi, L. Boarino, F. Taulelle, et al., Chem. Soc. Rev. 43, 2014, 7963–7981.

[3] Z. Yang, J. Zhang, M.C.W. Kintner-Meyer, X. Lu, D. Choi, J.P. Lemmon, et al., Chem. Rev. 111, 2011, 3577–3613.

[4] Ren 21, Renewables 2014 Global Status Report, 2014.

[5] N. S. Lewis, Solar Energy Use, 2007, 798–802.

[6] M. G. Walter, E. L. Warren, J.R. McKone, S.W. Boettcher, Q. Mi, E.A. Santori, et al., Solar Water Splitting Cells, Chem. Rev. 110 , 2010, 6446–647.

[7] K. J. Stevenson, V. Ozoliņš, B. Dunn, Electrochemical Energy Storage, Acc. Chem. Res. 46 , 2013, 1051–1052.

[8] Y. Zhao, Y. Ding, Y. Li, L. Peng, H.R. Byon, J.B. Goodenough, et al., A Chemistry and Material Perspective on Lithium Redox Flow Batteries Towards High-density Electrical Energy Storage, Chem. Soc. Rev. 44, 2015, 7968–7996.

[9] D. P. Dubal, O. Ayyad, V. Ruiz, P. Gomez-Romero, Chem. Soc. Rev. 44, 2015, 1777–1790.

[10] N. Tétreault, É. Arsenault, L.P. Heiniger, N. Soheilnia, J. Brillet, T. Moehl, et al., Nano Lett. 11, 2011, 4579–4584.

[11] D. C. Dillen, K. Kim, E.-S. Liu, E. Tutuc, Nat Nano. 9, 2014, 116–120.

[12] A. I. Hochbaum, P. Yang, Chem. Rev. 110, 2010, 527–546.

[13] M. L. Brongersma, Y. Cui, S. Fan, Nat Mater. 13, 2014, 451–460.

[14] (a) A. Stein, B.E. Wilson, S.G. Rudisill, Chem. Soc. Rev. 42, 2013, 2763–2803. (b) M. Kohler and W. Fritsche, chapter 4, Wiley-VCH Verlag GmbH & Co. KGaA, 2007

[15] A. S. Baranski, S. Bennett, and W. R. Fawcett.T. J. appl. Phys. 54, 1983,. 63-90

[16] K. M. Gorubunova and Y.I. Polukaro in: Advances in Electrochemistry and Electrochemical Engineering, Vol. *5*. Wiley/Interscience, New York 1967.

[17] A. Brenner, Electrodeposition of Alloys: Principle and Practice, Academic Press, New York 1963

[18] L. S. R. Yeh, P . G. Hudson and A. Dadijanovic, J. appl. Electrochem. 12, 1982, 133.

[19] M. M. Koltuns, elective Optical Surfaces for Solar Energy Converters, Allerton Press, Inc.,New York, 1981

[20] O. P. Aghiro and B. K. Gupta, Solar Selective Surfaces, John Wiley and Sons, New York, 1980

[21] J. Luo, L. Shreier, M Son, Marcel Schreier, Matthew T. Mayer, and Michael Gratzel, Nano Lett. 16, 2016, 1848-1857,

[22] Joseph E. Yourey, Kayla J. Pyper, Joshua B. Kurtz, and Bart M. Bartlett, J. Phys. Chem. C 117, 2013, 8708−8718,

[23] A. Martınez-Garcıa, V.K Vendra, S. Sunkara, P. Haldankar, J. Jasinski, and M. K. Sunkara, J. Mater. Chem. A1, 2013, 15235–15241

[24] P. K. Mahapatra a nd C. B. Roy, Electrochim. Acta 29, 1984, 1435

[25] G. Hodes and D. Cahen, Solar Cells 16, 1986, 245

[26] R. D. Srivatasva and R. C. Mukkereje J, appl. Electrochem. 6, 1976,.321

[27] J.Labrem and V. Delmas 6th EEC Photovoltaic Solar Energy Conf., London April 15 to19, 1985.
[28] Wen Ye, Fengjiao Chen, Feipeng Zhao, Na Han, and Yanguang Li, ACS Appl. Mater. Interfaces 8, 2016, 9211−9217.
[29] D. Cao, N.Nasori, Z, Wang,Y.Mi, L.Wen, Y.Yang, S. Qu, Z. Wang, and Y.Lei, J. Mater. Chem. A, 25, 2016
[30] A. Paracchino, V. Laporte, K. Sivula, M.Grätzel and E. Thimsen, Nat. Matt. 10, 2011.
[31] G.F. Fulop and R.M. Taylor, Ann.Rev. Mater.Sci 15.1985, 197-210.
[32] F. A. Krogers, Electrochem. Soc. 125, 1978, 20-28
[33] U. Cohen, R. A. Huggins, J. Electrochem. Soc. 123, 1976.381-383.
[34] J. J. Cuomo, , R. J. Gambino, Electrochem. Soc. 115, 1968, 755-759.
[35] Elwell, D., Feigelson, R. S. Sol. Energy Mater. 6, 1982, 123-145.
[36] Lee, C. H., Kroger, F. A. J.Electrochem. Soc. 129, 1982. 936-942.
[37] R. Mohan, T. R., Kroger, F. A. Electrochim. Acta 27, 1982, 371-77.
[38] Ou S. S., Bindal, A., Stafsudd, O. Wang, K. L., Basol, B. M. J. Appl. Phys.55: 1984, 1020-1022
[39] M.F. Weber, M. Dignam, J., Electrochem. Soc. 1984, 131 1258.
[40] H. Gereisher, J. Electroanal. Chem. 82, 1977,133.
[41] A.J. Bard, Wrington, M.S., J. Electrochem. Soc. 1977, 124, 1706.
[42] O. Khaselev, Turner A. J., J. Electrochem. Soc. 1998, 145, 3335.
[43] Heller A., Science 223,1984, 1141
[44] O. K.Varghese, Grimes C.A., Sol. Energy Matter Solar Cells, 2009.
[45] B. Parkinson, Acc. Chem. Res. 73, 1984, 431.
[46] M. G. Walter, E. L. Warren, J. R. McKone, S. W. Boettcher, Q. Mi, E.A. Santori, and N.S. Lewwis, Chem. Rev. 110, 2010, 6446-6473.
[47] B. M. Kayes, H. A. Atwater, N. S.Lewis, J. Appl. Phys. 97,2005, 11.
[48] J. M. Spurgeon, H. A. Atwater, N. S. Lewis, J. Phys. Chem. C, 112,2008, 6186.
[49] B. H. Erne, D. Vanmaekelbergh, J. J. Kelly, Adv. Mater. 7, 1995, 739.
[50] B. H. Erne, D. Vanmaekelbergh, J. J. Kelly, J. Electrochem. Soc. 143, 1996, 305. (b) J. R. Maiolo, H. A. Atwater, N. S. Lewis, J. Phys. Chem. C 112, 2008, 6194.
[51] J. R. Maiolo, B. M. Kayes, M. A. Filler, M. C. Putnam, M. D. Kelzenberg, H. A. Atwater, N. S. Lewis, J. Am. Chem. Soc. 129,2007, 12346.
[52] M. X.Tan, C. N. Kenyon, O. Kruger, N. S. Lewis, J. Phys.Chem. B 101,1997, 2830.
[53] O. Kruger, C. N.Kenyon, M. X. Tan, N. S. Lewis, J. Phys. Chem. B 101,1997, 2840.
[54] C. N. Kenyon, M. X.Tan, O. Kruger, N. S. Lewis, J. Phys. Chem. B 101,1997, 2850.
[55] M. X., Kenyon, C. N., & Lewis, N. S.. Experimental measurement of quasi-fermi levels at an illuminated semiconductor/liquid contact. Journal of Physical Chemistry, 98, 1994. 4959-4962.
[56] S. Sorrell, J. Speirs, R. Bentley, A. Brandt & R. Miller. Global Oil Depletion: An Assessment of the Evidence for a Near-Term Peak in Global Oil Production. UK Energy Research Center 2009, 1-198.
[57] N. A. Sciences & T. R. Society. Climate Change: Evidence and Causes. National Academies Press, 2014.
[58] AG Energiebilanzen. Stromerzeugung nach Energieträgern 1990 - 2014 Stand 27.02.2015.

[59] Amsterdam Roundtable Foundation and McKinsey & Company. Electric Vehicles in Europe: Gearing up for a New Phase, 2014, Ch. 1.
[60] B. E. Conway. Electrochemical Supercapacitors: Scientific Fundamentals and Technological Applications. Springer, 1999.
[61] P. Simon & Y. Gogotsi. Materials for Electrochemical Capacitors. Nature Materials 7, 2008, 845-854
[62] Z. Yang, J. Zhang, M.C.W. Kintner-Meyer, X. Lu, D. Choi, J.P. Lemmon, et al., Electrochemical Energy Storage for Green Grid, Chem. Rev. 111, 2011, 3577–3613.
[63] (a) Ren 21, Renewables 2014 (b) Global Status Report, 2014.
[64] N. S. Lewis, Solar Energy Use, 2007, 798–802.
[65] J.W. Long, B. Dunn, D.R. Rolison, H.S. White, Three-Dimensional Battery Architectures, Chem. Rev. 104, 2004, 463–492.
[66] J. Wallentin, N. Anttu, D. Asoli, M. Huffman, I. Aberg, M.H. Magnusson, et al., InP Nanowire Array Solar Cells Achieving 13.8 % Efficiency by Exceeding the Ray Optics Limit., Science 339, 2013, 1057–60.
[67] W. Lee, S.J. Park, Chem. Rev. 2014.
[68] O'Sullivan. P., J.; Wood, G. C. Proc. R. Soc. London, Ser. A 317,1970, 511.
[69] G. E. Thompson, Y. Xu, P.Skeldon, K. Shimizu, S. H.Han, G. C. Wood, Philos Mag B 1987, 55, 651.
[70] K. Shimizu, Kobayashi, K.; Thompson, G. E.; Wood, G. C. Philos Mag A 1992, 66- 643.
[71] G. E. Thompson, Thin Solid Films 297, 1997, 192.
[72] F. Y..Li, L.Zhang, R. M. Metzger, Chem. Mater. 10, 1998, 2470.
[73] J. M. Albella, I. Montero, M. C. Jimenez, J. M. Martinezduart, Electrochim. Acta 36, 1991, 739.
[74] T.Ozel, G. R. Bourret, C. A. Mirkin, Nat Nanotechnol 10,2015, 319.
[75] L. Y.Wen, Z. J.Wang, Y.Mi, R. Xu, S. H.Yu, Y. Lei, Small 11, 2015, 3408.
[76] H. Habazaki, Y. Konno, Y. Aoki, P. Skeldon, and G. E. Thompson, J. Phys. Chem. C 114,2010, 18853–18859
[77] T. Wang, Z. Luo, C. Li , J. Gong, Chem. Soc. Rev.43, 2014, 7469-7484
[78] V. Miikkulainen, M. Leskela, M. Ritala, R. L. Puurunen, J. Appl. Phys. 113,2013, 2.
[79] L. Y.Wen, Y.Mi, C. L.Wang, Y. G. Fang, F.Grote, H. P. Zhao, M. Zhou, Y.Lei, Small 10,2014, 3162.
[80] R. M. Penner, J Phys Chem C 118, 2014, 17179.
[81] https://en.wikipedia.org/wiki/Electron_beam_physical_vapor_deposition
[82] https://en.wikipedia.org/wiki/Scanning_electron_microscope.
[83] https://en.wikipedia.org/wiki/Scanning_electron_microscope
[84] https://en.wikipedia.org/wiki/Transmission_electron_microscopy
[85] https://en.wikipedia.org/wiki/Potentiostat
[86] https://en.wikipedia.org/wiki/Ultraviolet%E2%80%93visible_spectroscopy
[87] https://en.wikipedia.org/wiki/Time-resolved_spectroscopy
[88] Gong, D., Grimes, C. A., Varghese, O. K., Hu, W. C., Singh, R. S., Chen, Z., & Dickey, E. C.. J Mater Res 16, 2001: 3331.
[89] S. Berger, H. Tsuchiya, A. Ghicov and P. Schmuki, Appl. Phys. Lett., 2006, 88 203119.
[90] X. Qiu, J. Y. Howe, M. B. Cardoso, O. Polat, W. T. Heller and M. P. Paranthaman, Nanotechnology, 2009, 20, 455601
[91] A. Fujishima and K. Honda, Nature 238,, 1972, 37–38.
[92] K. Maeda, K. Teramura, D. Lu, T. Takata, N. Saito, Y. Inoue, K. Domen, Nature440, 2006, 295.
[93] A. Kudo and Y. Miseki, Chem. Soc. Rev., 2009, 38, 253–278.
[94] Z. Zou, J. Ye, K. Sayama, H. Arakawa, Nature, 2001, 625–627.
[95] A. J. Bard and M. A. Fox, Acc. Chem. Res. 28,, 1995, 141–145.
[96] K. Sivula, F. Le Formal and M. Grätzel, Chem. Sus. Chem 4, 2011, 432–449.

[97] S. U. M. Khan, Science, 2002, 297, 2243–2245.
[98] M. Ni, M. K. H. Leung, D. Y. C. Leung ,K. Sumathy, Renew. Sustain. Energy Rev. 11, 2007, 401–425.
[99] A. Paracchino, V. Laporte, K. Sivula, M. Grätzel and E. Thimsen, Nat. Mater. 10, 2011, 456–461.
[100] D. Cao, Z. Wang, Nasori, L. Wen, Y. Mi and Y. Lei, Angew. Chemie Int. Ed. 53, 2014, 11027–11031.
[101] R. Memming and G. Schwandt, Electrochim. Acta, 13, 1968,1299–1310.
[102] J. He, H. Lindström, A. Hagfeldt and S.-E. Lindquist, J. Phys. Chem. B, 1999, 103, 8940–8943.
[103] E. A. Gibson, A. L. Smeigh, L. Le Pleux, J. Fortage, G. Boschloo, E. Blart, Y. Pellegrin, F. Odobel, A. Hagfeldt and L. Hammarström, Angew. Chemie Int. Ed., 2009, 48, 4402–4405.
[104] W. Siripala, A. Ivanovskaya, T. F. Jaramillo, S.-H. Baeck and E. W. McFarland, Sol. Energy Mater. Sol. Cells, 2003, 77, 229–237.
[105] Z. Zhang and P. Wang, J. Mater. Chem., 2012, 22, 2456–2464.
[106] M. Halmann, Nature, 1978, 275, 115–116.
[107] N. T. Hahn, V. C. Holmberg, B. A. Korgel and C. B. Mullins, J. Phys. Chem. C, 2012, 116, 6459–6466.
[108] R. Patil, S. Kelkar, R. Naphade and S. Ogale, J. Mater. Chem. A, 2014, 2, 3661–3668.
[109] T. Arai, M. Yanagida, Y. Konishi, Y. Iwasaki, H. Sugihara and K. Sayama, J. Phys. Chem. C, 2007, 111, 7574–7577.
[110] W. Da Oh, S.-K. Lua, Z. Dong and T. T. Lim, Nanoscale, 2016, 8, 2046–2054.
[111] W. Da Oh, S. K. Lua, Z. Dong and T. T. Lim, Nanoscale, 2015, 7, 8149–8158.
[112] S. P. Berglund, H. C. Lee, P. D. Núñez, A. J. Bard and C. B. Mullins, Phys. Chem. Chem. Phys., 2013, 15, 4554–4565.
[113] Y. Nakabayashi, M. Nishikawa and Y. Nosaka, Electrochim. Acta, 2014, 125, 191–198.
[114] H. S. Park, C. Y. Lee and E. Reisner, Phys. Chem. Chem. Phys., 2014, 16, 22462–22465.
[115] M. Wang, J. Zai, X. Wei, W. Chen, N. Liang, M. Xu, R. Qi and X. Qian, CrystEngComm, 2015, 17, 4019–4025.
[116] Y. Mi, L. Wen, Z. Wang, D. Cao, H. Zhao, Y. Zhou, F. Grote and Y. Lei, Catal. Today, 2016, 262, 141–145.
[117] D. F. Zhang, H. Zhang, L. Guo, K. Zheng, X. D. Han and Z. Zhang, J. Mater. Chem., 2009, 19, 5220–5225.
[118] T. Arai, M. Yanagida, Y. Konishi, Y. Iwasaki, H. Sugihara and K. Sayama, J. Phys. Chem. C, 2007, 111, 7574–7577.
[119] C. Clavero, Nat. Photonics, 2014, 8, 95–103.
[120] A. Muthukrishnaraj, S. Vadivel, I. M. Joni and N. Balasubramanian, Ceram. Int., 2015, 41, 6164–6168.
[121] G. Sharma, Z. Zhao, P. Sarker, B. A. Nail, J. Wang, M. N. Huda and F. E. Osterloh, J. Mater. Chem. A, 2016, 4, 2936–2942.
[122] S. Bai, J. Ge, L. Wang, M. Gong, M. Deng, Q. Kong, L. Song, J. Jiang, Q. Zhang, Y. Luo, Y. Xie and Y. Xiong, Adv. Mater., 2014, 26, 1–7.
[123] Z. Zhang and P. Wang, J. Mater. Chem., 2012, 22, 2456–2464.
[124] M. Hara, T. Kondo, M. Komoda, S. Ikeda, J.N. Kondo, K. Domen, M. Hara, K. Shinohara, A. Tanaka, Chem. Commun. 2 (1998) 357.
[125] C. Xiang, G.M. Kimball, R.L. Grimm, B.S. Brunschwig, H. a. Atwater, N.S. Lewis, Energy Environ. Sci. 4 (2011) 1311.
[126] H. Azimi, S. Kuhri, A. Osvet, G. Matt, L. S. Khanzada, M. Lemmer, N. A. Luechinger, M. I. Larsson, E. Zeira, D. M. Guldi and C. J. Brabec, J. Am. Chem. Soc., 2014, 136, 7233–7236.
[127] A. Paracchino, N. Mathews, T. Hisatomi, M. Stefik, S.D. Tilley, M. Grätzel, Energy

Environ. Sci. 5 (2012) 8673.
[128] Z. Zheng, B. Huang, Z. Wang, M. Guo, X. Qin, X. Zhang, P. Wang, Y. Dai, J. Phys. Chem. C 113, 2009, 14448.
[129] L. Wu, L. Tsui, N. Swami, G. Zangari, J. Phys. Chem. C 114, 2010, 11551.
[130] Y.S. Lee, J. Heo, S.C. Siah, J.P. Mailoa, R.E. Brandt, S.B. Kim, R.G. Gordon, T. Buonassisi, Energy Environ. Sci. 6, 2013, 2112.
[131] Y. Mi, L. Wen, Z. Wang, D. Cao, H. Zhao, Y. Zhou, F. Grote, Y. Lei, Catal. Today 262 ,2016, 141.
[132] Y. Xu, H. Wang, Y. Yu, L. Tian, W. Zhao, B. Zhang, J. Phys. Chem. C 115, 2011, 15288.
[133] M.D. Susman, Y. Feldman, A. Vaskevich, I. Rubinstein, ACS Nano 8, 2014, 162.
[134] S. Brittman, Y. Yoo, N.P. Dasgupta, S.I. Kim, B. Kim, P. Yang, Nano Lett. 14, 2014, 4665.
[135] Y. Nakano, S. Saeki, T. Morikawa, Appl. Phys. Lett. 94 , 2009, 3.
[136] B.K. Meyer, A. Polity, D. Reppin, M. Becker, P. Hering, P.J. Klar, T. Sander, C. Reindl, J. Benz, M. Eickhoff, C. Heiliger, M. Heinemann, J. Bläsing, A. Krost, S. Shokovets, C. Müller, C. Ronning, Phys. Status Solidi B 249, 2012, 1487.
[137] R. Ji, W. Sun, Y. Chu, Chem. Phys. Chem 14, 2013, 3971.
[138] S. Poulston, P.M. Parlett, P. Stone, M. Bowker, Surf. Interface Anal. 24, 1996, 811.
[139] Y.K. Hsu, C.H. Yu, Y.C. Chen, Y.G. Lin, Electrochim. Acta 105, 2013, 62.
[140] Y. Sui, W. Fu, Y. Zeng, H. Yang, Y. Zhang, H. Chen, Y. Li, M. Li, G. Zou, Angew. Chemie Int. Ed. 49, 2010, 4282.
[141] X. An, K. Li, J. Tang, ChemSusChem 7, 2014, 1086.
[142] C. Cheng, Y. Wen, X. Xu, H. Gu, J. Mater. Chem. 19, 2009, 8782.
[143] Zhang, Y. Luo, Y. Xie, Y. Xiong, Adv. Mater. 26, 2014, 1.
[144] M.A. Mahmoud, W. Qian, M.A. El-Sayed, Nano Lett. 11, 2011, 3285.
[145] Y. Pan, S. Deng, L. Polavarapu, N. Gao, P. Yuan, C.H. Sow, Q. Xu, Langmuir 28, 2012, 12304.
[146] Y.L. Liu, Y.C. Liu, R. Mu, H. Yang, C.L. Shao, J.Y. Zhang, Y.M. Lu, D.Z. Shen, X.W. Fan, Semicond. Sci. Technol. 20, 2005, 44.
[147] E. Ko, J. Choi, K. Okamoto, Y. Tak, J. Lee, Chem. Phys. Chem. 7, 2006, 1505.
[148] D.F. Zhang, H. Zhang, L. Guo, K. Zheng, X.D. Han, Z. Zhang, J. Mater. Chem. 19, 2009, 5220.
[149] M. Chitambar, Z. Wang, Y. Liu, A. Rockett, S. Maldonado, J. Am. Chem. Soc. 134 (2012) 10670.
[150] H.I. Karunadasa, C.J. Chang, J.R. Long, Nature 464, 2010, 1329.
[151] K. Rajeshwar, in: S. Licht (Ed.), Semiconductor Electrodes and Photoelectrochemistry, vol. 6, Wiley-VCH, Weinheim, 2002, p. 1, Chap. 1.
[152] E.C. Heltemes, Phys. Rev. 141, 1966, 803.
[153] D. M. Chapin, C. S. Fuller, G. L. Pearson, J. Appl. Phys. 25, 1954, 676.
[154] J. Britt, C. Ferekides, Appl. Phys. Lett. 62, 1993, 2851.
[155] B. O'Regan, M. Grätzel, Nature 353, 1991, 737–740.
[156] M. Chitambar, Z. Wang, Y. Liu, A. Rockett, S. Maldonado, J. Am. Chem. Soc. 134, 2012, 10670–81.
[157] M. A. Green, K. Emery, Y. Hishikawa, W. Warta, E. D. Dunlop, Prog. Photovoltaics Res. Appl. 21, 2013, 827–837.
[158] M. A. Green, K. Emery, Y. Hishikawa, W. Warta, E. D. Dunlop, Prog. Photovoltaics Res. Appl. 22, 2014, 1–9.
[159] H.Taniguchi, A. Kuwabara, J. Kim, Y. Kim, H. Moriwake, S.Kim, T. Hoshiyama, T. Koyama, S. Mori, M. Takata, H. Hosono, Y. Inaguma, M. Itoh, Ferroelectricity Angew. Chem. Int. Ed., 52, 2013, 8088–8092.

[160] W. Ji, K. Yao, Y. C. Liang, Adv. Mater. 22, 2010, 1763–6.
[161] H. T. Yi, T. Choi, S. G. Choi, Y. S. Oh, S.-W. Cheong, Adv. Mater. 23, 2011, 3403.
[162] A. Bhatnagar, A. Roy Chaudhuri, Y. Heon Kim, D. Hesse, M. Alexe, Nat. Commun. 4,2013, 2835.
[163] T. Choi, S. Lee, Y. J. Choi, V. Kiryukhin, S.-W. Cheong, Science 324,,2009, 63.
[164] D. Cao, C. Wang, F. Zheng, W. Dong, L. Fang, M. Shen, Nano Lett. 12, 2012, 2803.
[165] D. Cao, J. Xu, L. Fang, W. Dong, F. Zheng, M. Shen, Appl. Phys. Lett. 96,2010, 192101.
[166] Y. Yuan, Z. Xiao, B. Yang, J. Huang, J. Mater. Chem. A 2, 2014, 6027-6041
[167] J. M. Frost, K. T. Butler, F. Brivio, C. H. Hendon, M. van Schilfgaarde, A. Walsh, Nano Lett. 14, 2014, 2584.
[168] J. Lee, S. Esayan, J. Prohaska, a. Safari, Appl. Phys. Lett. 64,1994, 294.
[169] L. Pintilie, M. Lisca, M. Alexe, Appl. Phys. Lett. 86,2005, 192902.
[170] S. Y. Yang, J. Seidel, S. J. Byrnes, P. Shafer, C.-H. Yang, M. D. Rossell, P. Yu, Y.-H. Chu, J. F. Scott, J. W. Ager, Nat. Nanotechnol. 5, 2010, 143–7.
[171] D. Lee, S. H. Baek, T. H. Kim, J.-G. Yoon, C. M. Folkman, C. B. Eom, T. W. Noh, Phys. Rev. B 84, 2011, 125305.
[172] W. Ji, K. Yao, Y.-F. Lim, Y. C. Liang, A. Suwardi, Appl. Phys. Lett.2013, 103, 062901.
[173] Z. L. Wang, W. Wu, Angew. Chem. Int. Ed. Engl. 51, 2012, 11700
[174] F. Gao, X. Y. Chen, K. B. Yin, S. Dong, Z. F. Ren, F. Yuan, T. Yu, Z. G. Zou, J.-M. Liu, Adv. Mater. 19, 2007, 2889–2892.
[175] S. K. Singh, H. Ishiwara, K. Maruyama, Appl. Phys. Lett. 88, 2006, 262908.
[176] H. Lee, Y. S. Kang, S.-J. Cho, B. Xiao, H. Morkoç, T. D. Kang, G. S. Lee, J. Li, S.-H. Wei, P. G. Snyder, et al., J. Appl. Phys. 98, 2005, 094108.
[177] S. Saha, T. Sinha, A. Mookerjee, Phys. Rev. B 62, 2000, 8828–8834.
[178] S. Y. Yang, L. W. Martin, S. J. Byrnes, T. E. Conry, S. R. Basu, D. Paran, L. Reichertz, J. Ihlefeld, C. Adamo, A. Melville, et al., Appl. Phys. Lett. 95, 2009, 62909.
[179] R. Schafranek, S. Payan, M. Maglione, A. Klein, Phys. Rev. B 77,2008 195310.
[180] B. C. Huang, Y. T. Chen, Y. P. Chiu, Y. C. Huang, J. C. Yang, Y. C. Chen, Y. H. Chu, Appl. Phys. Lett. 100, 2012, 122903.
[181] Z. Liu, F. Yan, Phys. status solidi - Rapid Res. Lett. 5, 2011, 367–369.
[182] P. M. Jones, D. E. Gallardo, S. Dunn, Chem. Mater.2008, 20, 5901–5906.
[183] Z. Wang, A. Shakya, J. Gu, S. Lian, S. Maldonado, J. Am. Chem. Soc. 135, 2013, 9275–8.
[184] J. W. Park, S. H. Baek, P. Wu, B. Winchester, C. T. Nelson, X. Q. Pan, L. Q. Chen, T. Tybell, C. B. Eom, Appl. Phys. Lett. 97,2010, 212904.
[185] A. Q. Jiang, C. Wang, K. J. Jin, X. B. Liu, J. F. Scott, C. S. Hwang, T. A. Tang, H. Bin Lu, G. Z. Yang, Adv. Mater. 23,2011, 1277–81.
[186] J. Wu, J. Wang, J. Appl. Phys.2010, 107, 034103.
[187] C. Wang, D. Cao, F. Zheng, W. Dong, L. Fang, X. Su, M. Shen, Chem. Commun. 49,2013, 3769–71.
[188] D. Cao, C. Wang, F. Zheng, W. Dong, L. Fang, M. Shen, Nano Lett.2012, 12, 2803–9.
[189] M. S. Wrighton, A. B. Ellis, P. T. Wolczanski, D. L. Morse, H. B. Abrahamson and D. S. J. Ginley, J. Am. Chem. Soc., 1976,98, 2774
[190] M. S. Wrighton, Acc. Chem. Res., 1979, 12, 303.

[191] N. S. Lewis, Acc. Chem. Res., 1990, 23, 176.

[192] E. Thimsen, F. Le Formal, M. Gra¨tzel, S. C. Warren. Nano Lett. 11, 2011, 35–43

[193] H. Chen, W. Leng, and Y. Xu, J. Phys. Chem. C 118,2014, 9982−9989

[194] F. Amano, D. Li, B. Ohtani, J Electrochem Soc 158, 2011, 426.

[195] S. Liew, Z. Zhang, T.G. Goh, G. Subramanian, H.D. Seng, T.A. Hor, et al. Int J Hydrogen Energy 39, 2014, 4291.

[196] M. Bao, Y. Chen, F. Li, J. Ma, T. Lee, Y. Tang, et al., Nanoscale, 6, 2014, 4063-4066

[197] H. Zhao, C. Wang, R. Vellacheri, M. Zhou, Y. Xu, Q. Fu, M. Wu, F. Grote and Y. Lei, Adv. Mater, 26, 2014, 7654–7659.

[198] L. Liang, Y. Xu, C. Wang, L. Wen, Y. Fang,Y. Mi, M. Zhou, H. Zhao and Y. Lei, Energy Environ. Sci.,2015, 8, 2954

[199] L. Wen, Y. Mi, C. Wang, Y. Fang, F. Grote, H. Zhao, M. Zhou and Y. Lei, Small, 2014, 10, 3162–3168.

[200] Z. Zhan and Y. Lei, ACS Nano, 2014, 8, 3862–3868.

[201] Y. Xu, M. Zhou, L. Wen, C. Wang, H. Zhao, Y. Mi, L. Liang, Q. Fu, M. Wu and Y. Lei, Chem. Mater., 2015, 27, 4274–4280.

[202] M. Denk, D. Kuhness, M. Wagner, S. Surnev, F. R. Negreiros, L. Sementa, G. Barcaro, I. Vobornik, A. Fortunelli, and F. P. Netzer. 8, 2014, 3947–3954

[203] J. E. Yourey and B. M. Bartlett, J. Mater. Chem., 21, 2011, 7651–7660.

[204] J. E. Yourey, K. J. Pyper, J. B. Kurtz and B. M. Bartlett, J. Phys. Chem. C 117,, 2013, 8708–8718.

[205] D. Hu, P. Diao, D. Xu, M. Xia, Y. Gu, Q. Wu, C. Li and S. Yang. Nanoscale, 8,2016, 5892.

[206] Y. Mi, L. Wen, R. Xu, Z. Wang , D. Cao, Y. Fang, and Y. Lei. Adv. Energy Mater. 150, 2016, 1496

[207] N. Gaillard, Y. Chang, A. DeAngelis, S. Higgins, A. Braun, Int J Hydrogen Energy 38, 2013, 316

[208] A. Kuzmin, A. Kalinko, R.A. Evarestov. Acta Materialia, 6, 2012, 1359-6454.

[209] K. Rajeshwar, in: S. Licht (Ed.), Semiconductor Electrodes and Photoelectrochemistry, vol. 6, Wiley-VCH, Weinheim, 2002, p. 1, Chap. 1.

[210] E.C. Heltemes, Phys. Rev. 141, 1966, 803.

[211] Z. Zhang and P. Wang, J. Mater. Chem., 22, 2012, 2456–2464

[212] A. Al-Haddad, Z. Wang, R. Xu, H. Qi, R. Vellacheri, U. Kaiser, and Y. Lei. J. Phys. Chem. C 119, 2015, 16331−16337

[213] M.M. Mohamed, S.A. Ahmed, K.S. Khairou, Applied Catalysi B:Environmental 150–151 ,2014, 63–73

[214] S. Arora, T. Mathew, N. Batra, J. Phys. D: Appl. Phys. 23, 1990, 460-464

[215] J. C. Hill and K.-S. Choi, J. Mater. Chem. A, 2013, 1, 5006–5014.

[216] K. J. Pyper, J. E. Yourey and B. M. Bartlett, J. Phys. Chem. C, 2013, 117, 24726–24732.

[217] Y. Gao, O. Zandi and T. W. Hamann, J. Mater. Chem. A, 2016, 4, 2826–2830.

[218] M. Valenti, D. Dolat, G. Biskos, A. Schmidt-Ott and W. A. Smith, J. Phys. Chem. C, 2015, 119, 2096–2104.

[219] Y. Chang, A. Braun, A. Deangelis, J. Kaneshiro and N. Gaillard, J. Phys. Chem. C, 2011, 115, 25490–25495.

[220] Y. Tang, N. Rong, F. Liu, M. Chu, H. Dong, Y. Zhang and P. Xiao, Appl. Surf. Sci., 2016, 361, 133–140
[221] J. C. Hill, Y. Ping, G. A. Galli and K.-S. Choi, Energy Environ. Sci., 2013, 6, 2440–2446.
[222] S. K. Pilli, T. G. Deutsch, T. E. Furtak, L. D. Brown, J. A. Turner and A. M. Herring, Phys. Chem. Chem. Phys., 2013, 15, 3273–3278.
[223] G. Sharma, Z. Zhao, P. Sarker, B. A. Nail, J. Wang, M. N. Huda and F. E. Osterloh, J. Mater. Chem. A, 2016, 4, 2936–2942.
[224] D. Y. Guo , J. B. Wang , C. Cui , P. G. Li , X. L. Zhong , F. Wang , S. G. Yuan , K. D. Zhang , Y. C. Zhou , Sol. Energy 2013 , 95 , 237
[225] L. Wen , Z. Wang , Y. Mi , R. Xu , S.-H. Yu , Y. Lei , Small 2015 , 11 ,3408 .
[226] Jain, P. K.; Huang, W.; El-Sayed, M. A. Nano Lett. 2007, 7,2080−2088.
[227] A. J. Bard and M. A. Fox, Acc. Chem. Res., 1995, 28, 141–145.
[228] X. Chen, S. Shen, L. Guo and S. S. Mao, Chem. Rev., 2010, 110, 6503–6570.
[229] R. Liu, Z. Zheng, J. Spurgeon and X. Yang, Energy Environ. Sci., 2014, 7, 2504–2517.
[230] S. J. A. Moniz, S. A. Shevlin, D. J. Martin, Z.-X. Guo and J. Tang, Energy Environ. Sci., 2015, 8, 731–759.
[231] C. Jiang, S. J. a Moniz, M. Khraisheh and J. Tang, Chem. - A Eur. J., 2014, 12954–12961.
[232] M. Hara, T. Kondo, M. Komoda, S. Ikeda, J. N. Kondo, K. Domen, M. Hara, K. Shinohara and A. Tanaka, Chem. Commun., 1998, 2, 357–358.
[233] G. Ghadimkhani, N. R. de Tacconi, W. Chanmanee, C. Janaky and K. Rajeshwar, Chem. Commun., 2013, 49, 1297–9.
[234] M. Cao, C. Hu, Y. Wang, Y. Guo, C. Guo and E. Wang, Chem. Commun., 2003, 1, 1884–1885.
[235] Y. Tan, X. Xue, Q. Peng, H. Zhao, T. Wang and Y. Li, Nano Lett., 2007, 7, 3723–3728.
[236] J. Zhang, J. Liu, Q. Peng, X. Wang and Y. Li, Chem. Mater., 2006, 18, 867–871.
[237] Y. Lei, W. Cai and G. Wilde, Prog. Mater. Sci., 2007, 52, 465–539.
[238] Y. Lei, S. Yang, M. Wu and G. Wilde, Chem. Soc. Rev., 2011, 40, 1247–1258.
[239] Y. Lei, L. D. Zhang, G. W. Meng, G. H. Li, X. Y. Zhang, C. H. Liang, W. Chen and S. X. Wang, Appl. Phys. Lett., 2001, 78, 1125.
[240] M. Law, L. E. Greene, J. C. Johnson, R. Saykally and P. Yang, Nat. Mater., 2005, 4, 455–459.
[241] P. J. Pauzauskie and P. Yang, Mater. Today, 2006, 9, 36–45.
[242] H. Sun, J. Deng, L. Qiu, X. Fang and H. Peng, Energy Environ. Sci., 2015, 8, 1139–1159.
[243] Q. Zhang and G. Cao, Nano Today, 2011, 6, 91–109.
[244] A. Ibhadon and P. Fitzpatrick, Catalysts, 2013, 3, 189–218.
[245] P. V. Kamat, J. Phys. Chem. Lett., 2010, 1, 520–527.
[246] I. Oh, J. Kye and S. Hwang, Nano Lett., 2012, 12, 298–302.
[247] K. Kinoshita, John Wiley Sons, Carbon: electrochemical and physicochemical proper New York, 1988.
[248] A. Brennere, electrodeposition of Alloys: Principle and Practice, Academic Press, New York, 1963.
[249] S. Bijani, R. Schrebler, E.A. Dalchiele, M. Gabas, L. Martinez, J.R.Ramos-Barrado, J.Phy. Che.C, 2011,115, 21373-21382.

Chapter 11. Appendix

1. Additional data for chapter 4

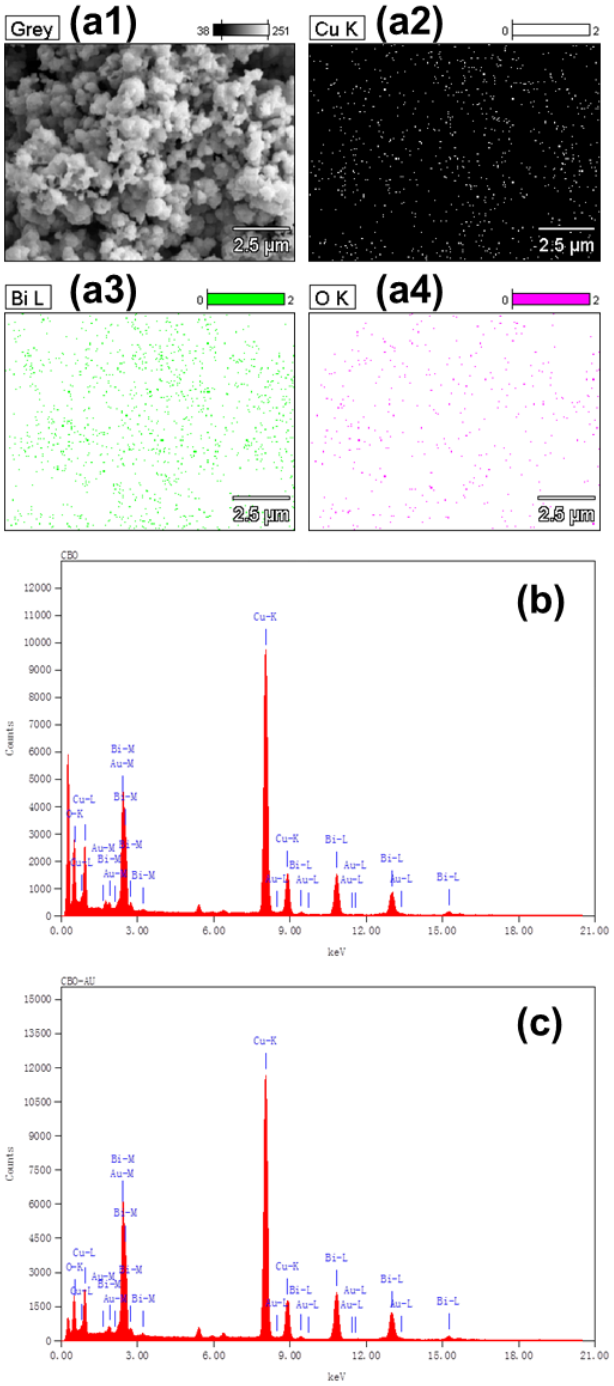

Figure 11.1 (a1) SEM image of CBO films on FTO, and corresponding EDX mapping image for (a2) Cu element, (a3) Bi element and (a4) O element. The representative EDX spectra of the CBO on FTO (b) and FTO/Au (c). In comparison with the spectrum from

FTO/CBO, the spectrum of the particles from FTO/Au/CBO does not show the indication in containing Au in the crystals.

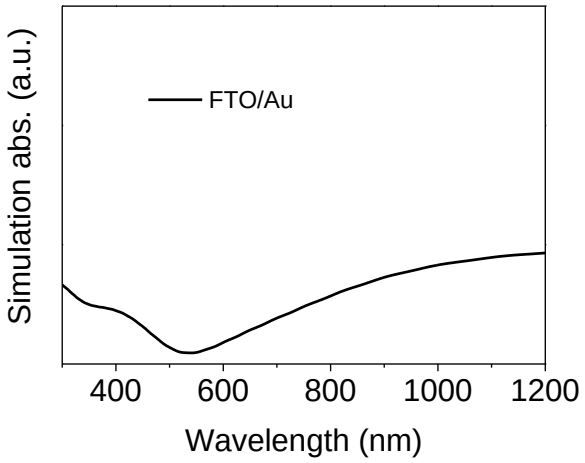

Figure 11.2 Simulated absorbance spectrum of the sample FTO/Au.

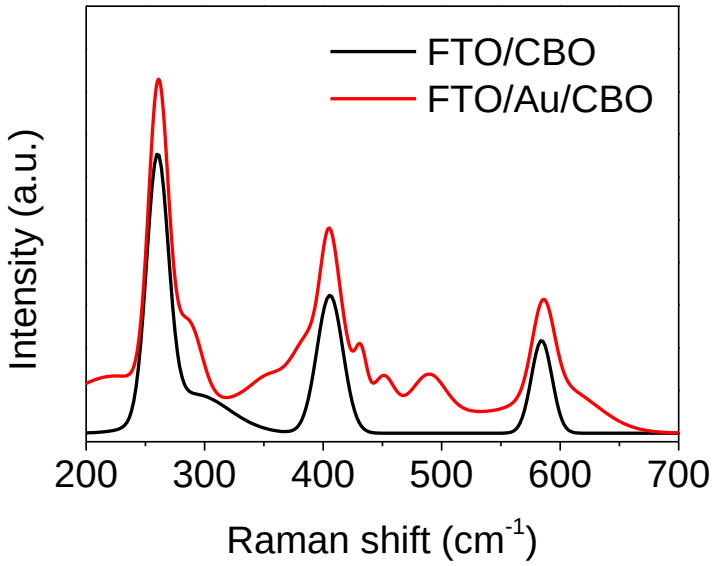

Figure 11.3 Raman spectra of CBO and Au/CBO on FTO glass. The distinct vibrational peaks at 262, 402 and 585 cm^{-1} demonstrate the presence of CBO, which is consistent with the previous report.

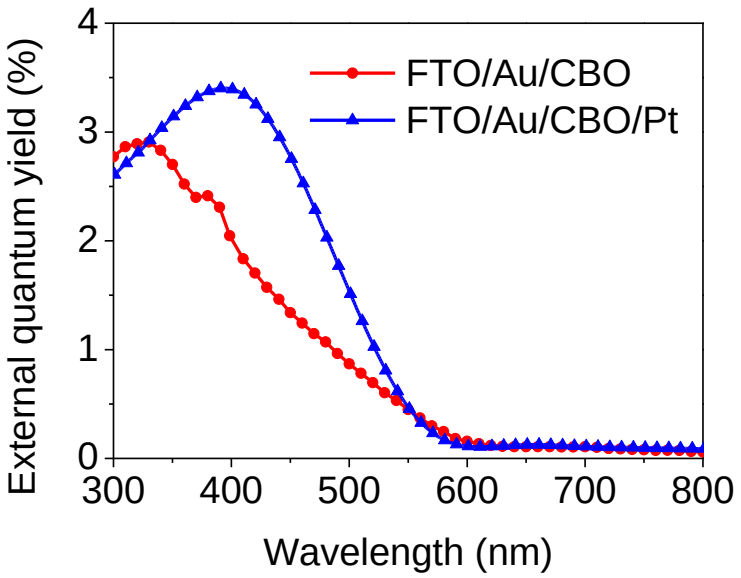

Figure 11.4 Wavelength-dependent external quantum yield spectra of the photoelectrodes with or without Pt catalyst (the spectra were measured in a two-electrode configuration without any external bias).

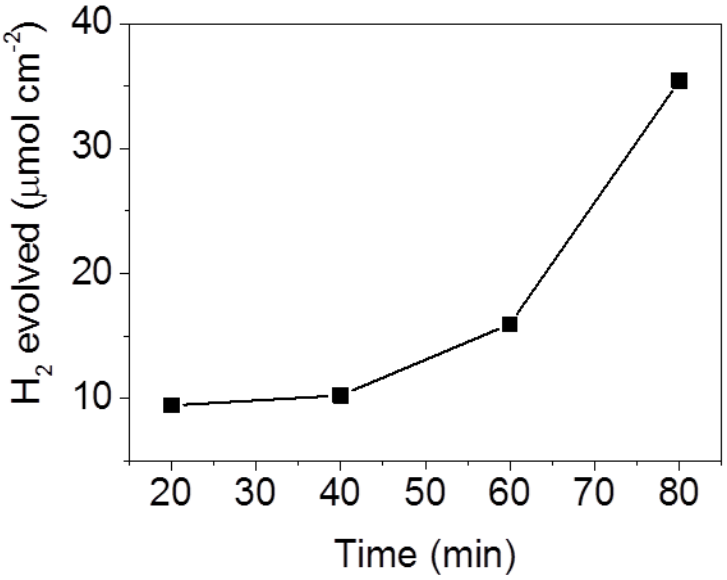

Figure 11.5 Hydrogen production on time measured under 0.2 V vs RHE with illumination of 100 mWcm^{-2}Xe lamp for the FTO/Au/CBOphotoelectrode with Pt nanoparticles. In our case, the water splitting reactorwas small in volume and the amount of evolved hydrogen was about µmol scale. Such small amount of hydrogen was quite easy to dissolve in the electrolyte solution and cannot be easily detected by the gas chromatograph equipment. In spite of these limitations, the result clearly shows that the

FTO/Au/CBO/Pt canactually work as photocathode for hydrogen production. The Faradic efficiency was calculatedas 84.49% for the water splitting reactor during 80 min.

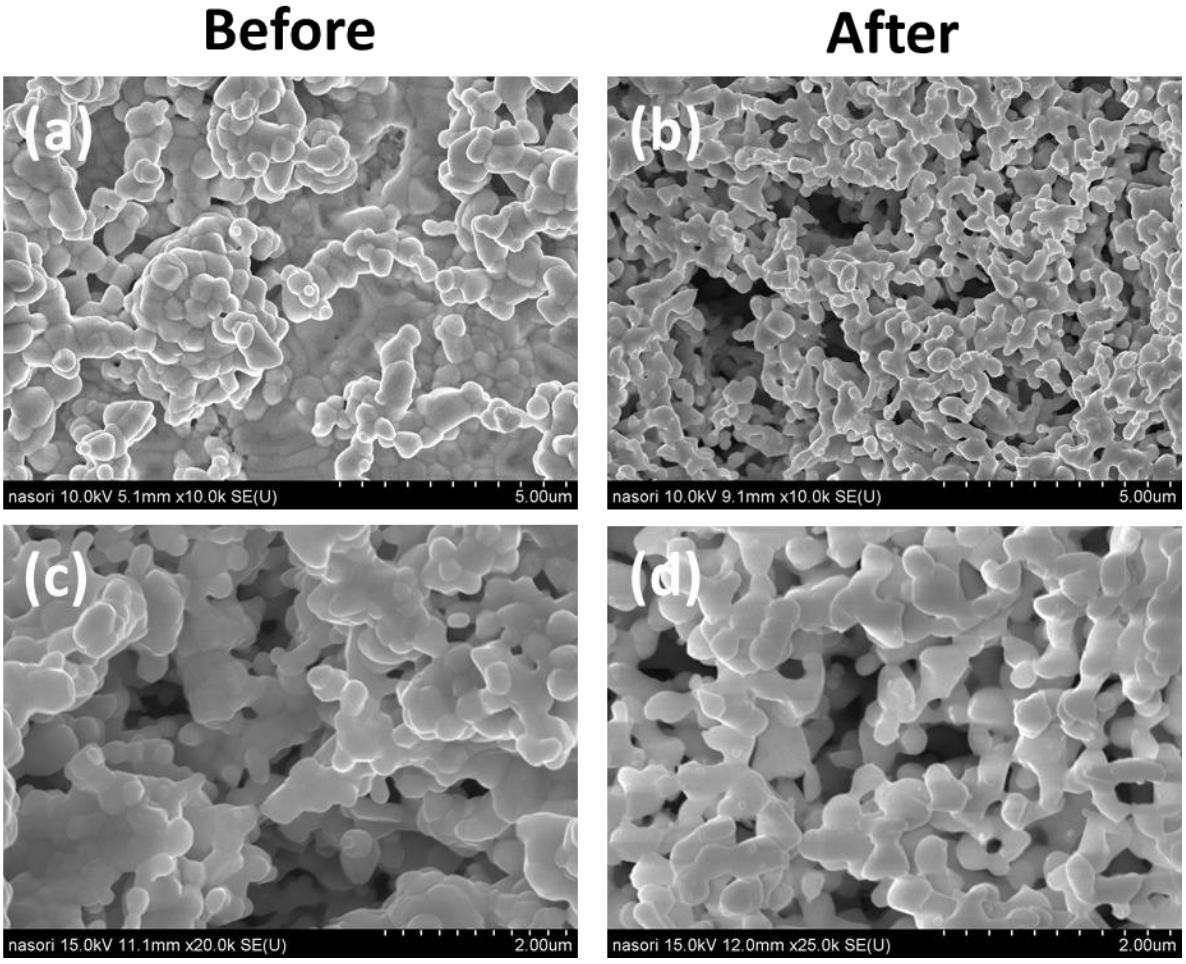

Figure 11.6 SEM images of FTO/Au/CBO before (a and c) and after (b and d) PEC measurement (3000 s).

2. Additional data for chapter 5

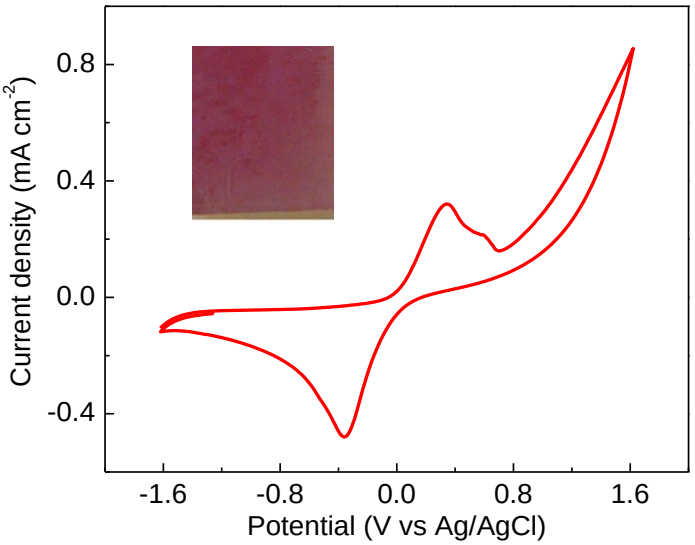

Figure 11.7 Cyclic voltammetry measurements for determining the depositing penitential of Cu_2O. In the curve, there are two peaks that can be ascribed to the reduction peak for Cu^{2+} to Cu_2O and the oxidation peak of Cu_2O, respectively. Accordingly, we choose a constant potential (−0.4 V vs Ag/AgCl) model for reducing Cu^{2+} to Cu_2O. The resulted thin films exhibit a dark red color as shown in the inset of Figure 11.7.

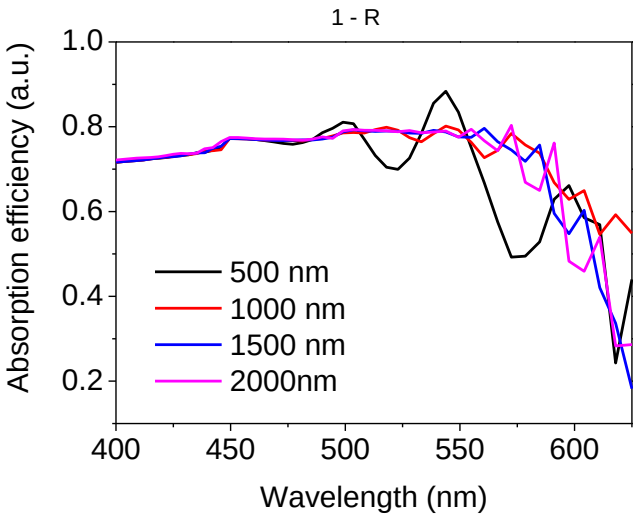

Figure 11.8 The calculated absorption efficiency in accordance with the thickness of Cu_2O on FTO/Au by FDTD simulation.

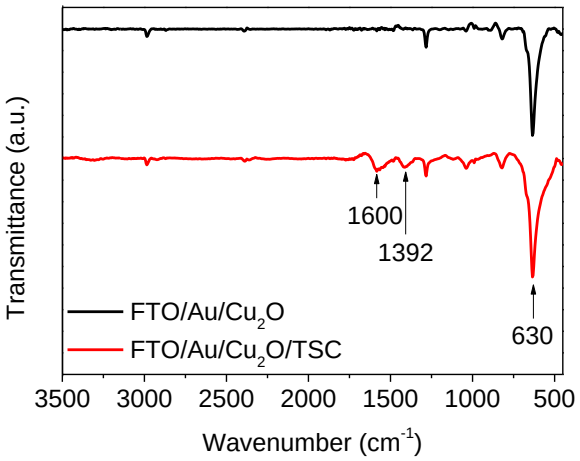

Figure 11.9 Fourier transform infrared transmission (FTIR) spectra for the FTO/Au/Cu_2O photoelectrode without/with TSC. Both the samples without and with surface treatment show the main peak of Cu_2O at about 630 cm^{-1}. Compared to the naked FTO/Au/Cu_2O sample, FTIR spectrum of the FTO/Au/Cu_2O/TSC exhibits the characteristic absorption peaks of carboxyl group of sodium citrate, such as 1600 cm^{-1} and 1392 cm^{-1} due to the –COO– symmetric and antisymmetric stretching respectively.

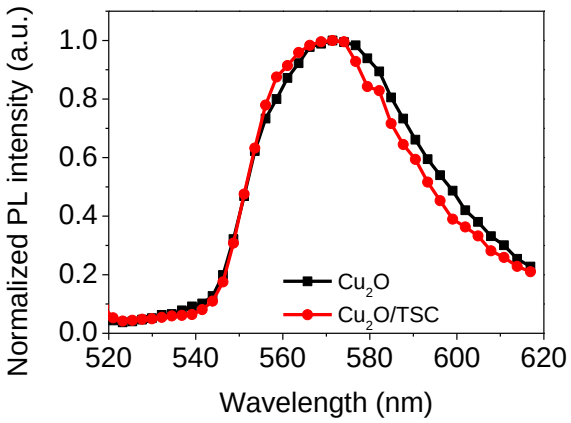

Figure 11.10 Normalized PL spectra of FTO/Au/Cu_2O and FTO/Au/Cu_2O/TSC.

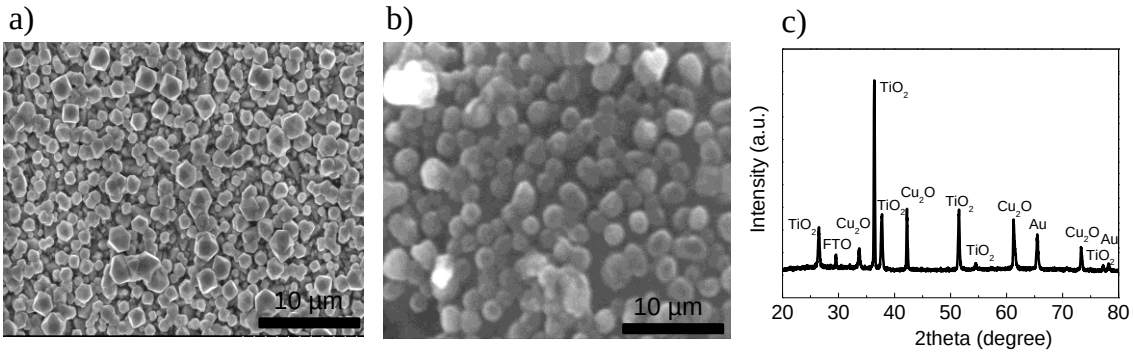

Figure 11.11 SEM images of a) FTO/Au/Cu_2O and b) FTO/Au/Cu_2O/TSC/TiO_2. c) XRD of the FTO/Au/Cu_2O/TSC/TiO_2 electrode. The thin layer of the TiO_2 was grown via an atomic layer deposition procedure at 200 °C. $TiCl_4$ and H_2O were selected as the precursors. In comparison with the intrinsic sample shown in Figure S3a, the TiO_2 passivated Cu_2O film shows a rough but homogenous surface, indicating a good strategy to protect the Cu_2O layer from corrosion during the measurements. The XRD pattern confirms the presence of TiO_2 on Cu_2O from other aspect.

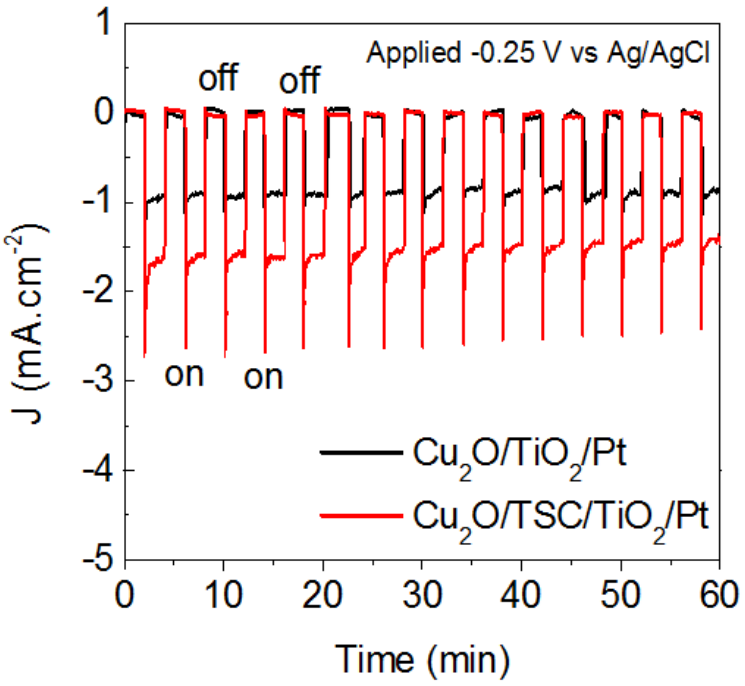

Figure 11.12 Curves of photocurrent vs time curve under interval on-off light irradiation of the FTO/Au/Cu_2O/TiO_2/Pt and FTO/Au/Cu_2O/TSC/TiO_2/Pt electrodes, applied −0.25 V vs Ag/AgCl.

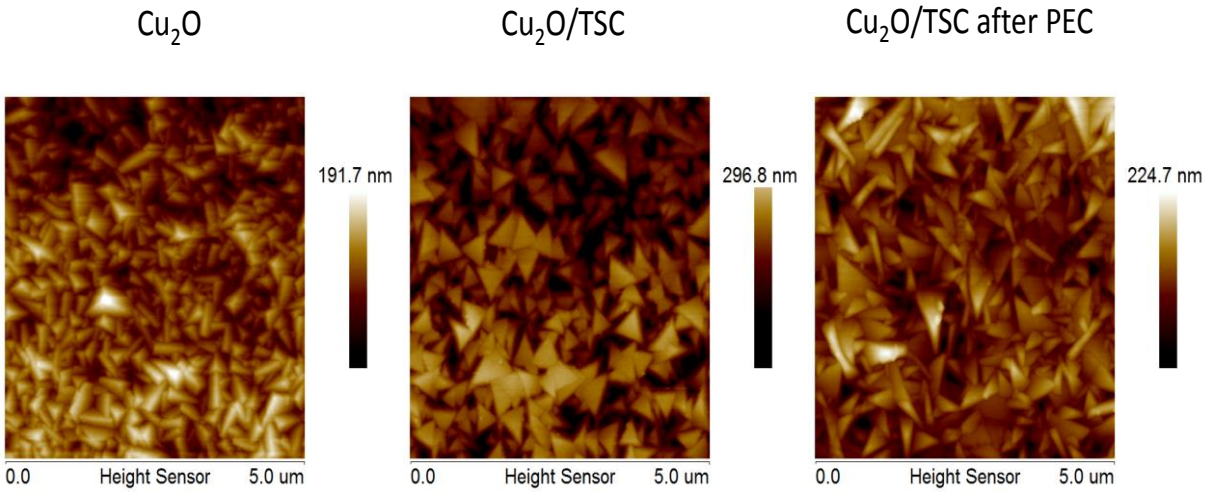

Figure 11.13 AFM of FTO/Au/Cu_2O, FTO/Au/Cu_2O/TSC and FTO/Au/Cu_2O/TSC after PEC measurement. No obvious changes of morphology before and after PEC measurement can be observed.

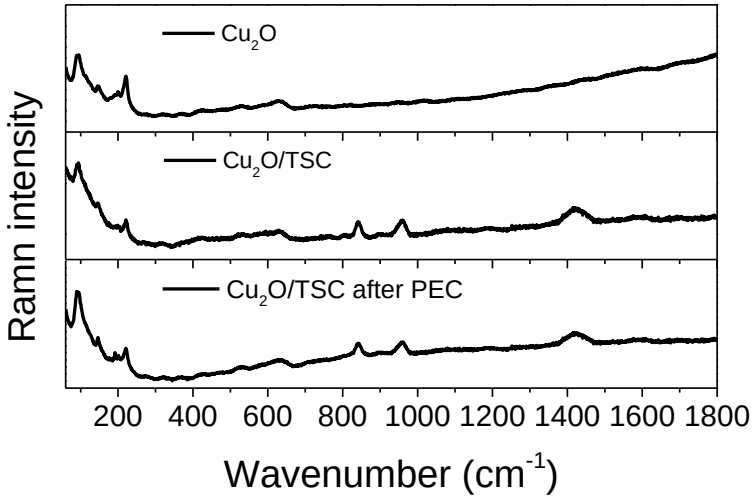

Figure 11.14 Raman spectrum of FTO/Au/Cu_2O, FTO/Au/Cu_2O/TSC and FTO/Au/Cu_2O/TSC after PEC measurement. The sample of FTO/Au/Cu_2O/TSC before and after PEC measurement exhibits the same assignment of the main bands of sodium citrate, such as 846 cm^{-1}, 945 cm^{-1} and 1435 cm^{-1}.

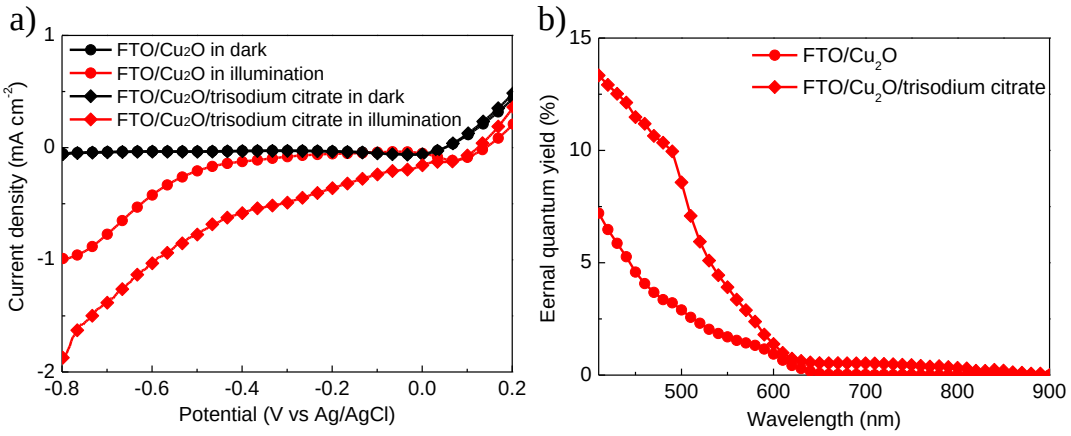

Figure 11.15 a) and b) Current density-potential curves and external quantum yield spectra for the FTO/Cu_2O photocathodes with different surface conditions. For the sample without surface treatment, photocurrent is lower than that from the bare photocathodes on the basis of FTO/Au/Cu_2O, due to the fact that the cubic morphology of the Cu_2O particles in the FTO/Cu_2O structure is disadvantageous in photocatalysis as compared with the polyhedral morphology of the particles in the structure of FTO/Au/Cu_2O. When the FTO/Cu_2O photocathode is soaked in TSC solution for 30 min, the photocurrent is enhanced markedly, showing the same tendency in the FTO/Au/Cu_2O measurements. The

external quantum yield spectra displayed in Figure 11.15b confirm this statement from another aspect. Thus, these data indicate that the surface treatment using TSC is applicable to Cu_2O films with different particle morphologies.

Table 10.1 Raw fitting parameters for transient photoluminescence analysis.

The curves of time resolved photoluminescence decay for the prepared Cu_2O thin films were fit by one exponential model in short time scale: $y=A\times\exp(-x/\tau)+y_0$.

Sample	A	y_0	τ (ns)
Au/Cu_2O	1.12	0.004	0.59±0.01
Au/Cu_2O/TSC	1.03	0.012	0.48±0.005

3. Additional data for chapter 6

A. Absorption spectroscopic analysis of the prepared BFO films on ITO/glass

Figure 11.16 displays the absorption spectra of the prepared BFO films. Contrary to most of the other ferroelectric materials like PZT and $BaTiO_3$,[176,189] BFO exhibits impressive absorption ability in the visible range of the solar energy. Considering the direct band gap structure in BFO,[172] a band gap value of 2.14 eV was estimated by converting the absorption spectrum to the $(ahv)^2$ vs.*hv* plot shown in the inset and calculating the intercept of the linear part of the plot with the X-axis. The obtained 2.14 eV is well matched with the values reported where else[174,163] and enables the BFO films with a promising potential in photoelectrochemical energy conversion and storage.

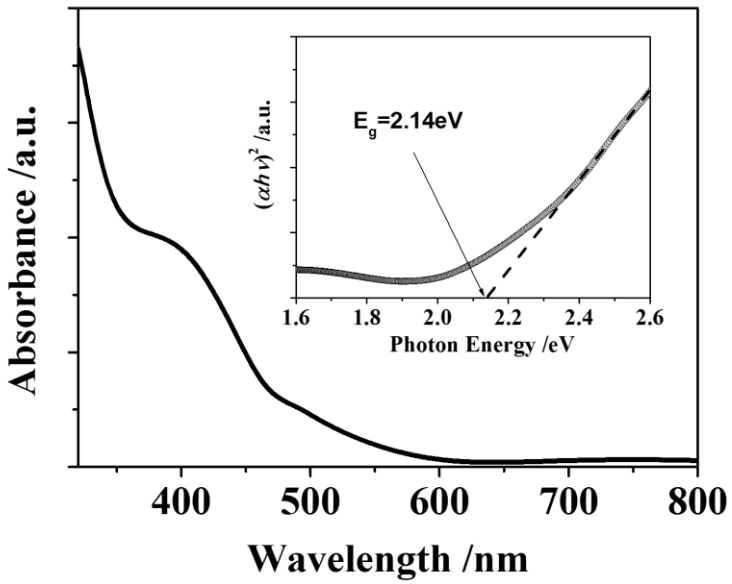

Figure 11.16 Absorption spectroscopic measurements of the BFO films

B. Polarization-electric (P-E) ferroelectric analysis of the prepared BFO films

Polarization-electric (P-E) hysteresis measurements as shown in Figure 11.17 clearly demonstrate the existence of the ferroelectric hysteresis that determines the switchable capability of the BFO film in both photovoltaic and photoelectrochemical applications. Particularly, the loop measured at 5V presents a clear hysteresis loop and roughly yields a coercive field as 200 kV/cm, close to the reported values.[178,185]When measuring at high voltages, the ferroelectric performance deteriorates mainly due to the large leakage current. The leakage current as obtained in Figure 3.2b is higher than the reported values for the BFO films made in high vacuum,[172,186] attributed to the cost-efficient fabrication technique. According to the measured coercive field as well as the reported values in the BFO films fabricated by high vacuum techniques,[184,185] a roughly estimated 8V poling bias is sufficient for tuning over the domain walls in the spin-coated BFO films with a thickness of 300 nm. Therefore, for the next procedure of poling treatment on the prepared BFO films, we choose the poling potential between −8 V to +8 V.

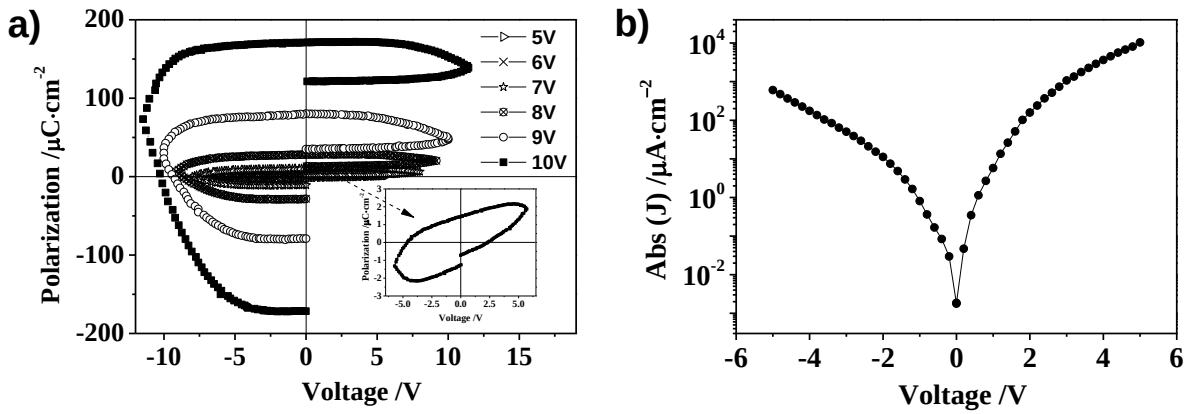

Figure 11.17 Ferroelectric properties of the BFO films: a) P-E hysteresis loop (the inset image: P-E hysteresis loop at 5 V; b) leakage current J-V curve

C. Discussion on the electrochemical poling pre-treatment

Considering the difficulty for the BFO photoelectrodes to be poled using a solid state method, we poled the photoelectrodes in propylene carbonate solution to avoid the small electrochemical window in aqueous solution. Though the ions in the electrolyte may screen the applied bias more or less, +8V and –8 V vs Pt counter electrode are sufficient for tuning the photoelectrochemical performance. As shown in Figure 6.2a and Figure 6.2b, the sample with +8 V poling pretreatment had a remarkable enhancement in external quantum yield as compared with the sample without any poling. When the sample experienced –8V poling subsequently, however, the external quantum yield decreased dramatically to a negligible value. As we re–poled the sample by +8 V, the external quantum yield restored to the previous value, strongly implying the existence of a distinct ferroelectric property in the prepared BFO films and orientations of the remnant polarization can be tuned well by the external biases. In addition, this electrochemical poling methodology also works well for PZT photoelectrodes, as illustrated in Figure 11.18b. All these data point to the validity of the poling pretreatment and the prepared ferroelectric films are stable after being used for many cycles of poling treatments. The PZT photoelectrodes were prepared following the procedure in our previous paper.[187] The P-E loop shown as the inset image of Figure 11.18b indicates that the 8V poling bias can also switch the orientations of the domain walls in PZT films.

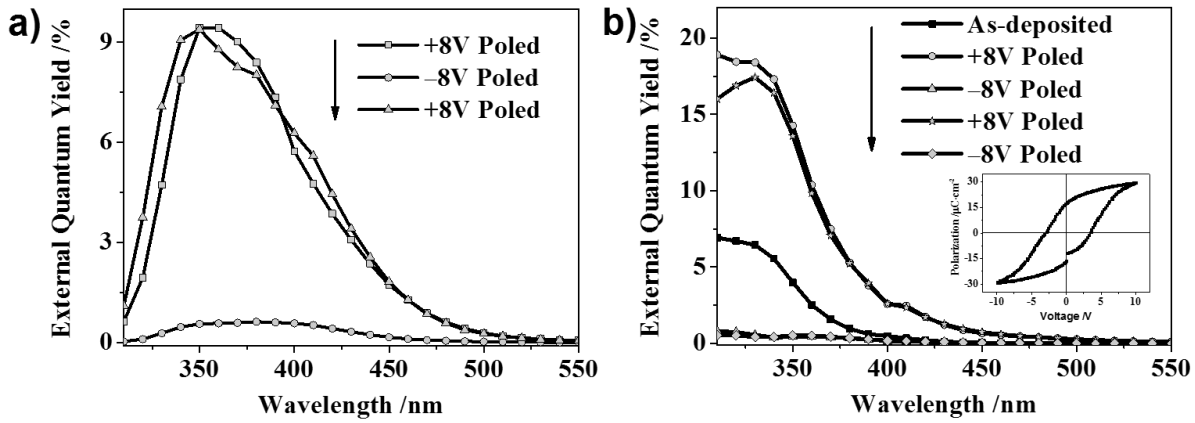

Figure 11.18 Investigation on the polarizations of the BFO and PZT photoelectrodes (inset: P-E loop of PZT films)

D. Discussion on the dependence of external quantum yield on the poling bias

Figure 11.19 illustrates a detailed analysis of the external quantum yield vs. poling bias in the positive direction. In the initial stage with the poling bias change from the intrinsic state (0 V) to 4 V, the external quantum yield increases slowly. After the subsequent poling treatment by enlarging the bias to the values higher than 6 V, however, the external quantum yield enhances abruptly and reaches a plateau, presenting a high similarity to the half loop in the P-E loops. The lower poling bias cannot turn over the domain walls. Once the positive poling potential is large enough for re-orientating the domain walls, the photocurrent signal increases greatly until to a plateau, due to the fact that the large positive potential can generate an upward band bending which promotes the separation of the photo-excited charges. Moreover, the threshold for the abrupt increase of external quantum yield is around 5 V, in consistence with the ferroelectric analysis. All these data strongly indicate the presence of pronounced ferroelectric properties in the prepared BFO films as that the orientations of the remnant polarization can be manipulated well by the external biases and the 8V poling potential behaves well for tuning the ferroelectric and photoelectrochemical performances of the spin-coated BFO films.

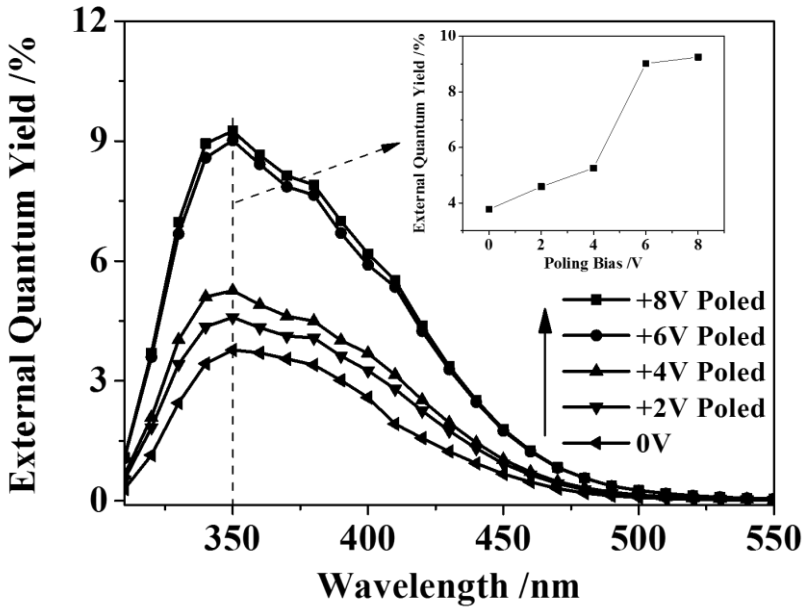

Figure 11.19 Dependence of external quantum yield on the poling bias for the prepared BFO photoelectrode

E. Investigations on switching photo–excited charge transfer from Rose Bengal and Brilliant Green to BFO photoelectrodes

In order to further support the conclusion about the charge transfer tuning from excited Rhodamine B to BFO films, we also checked the same scenario on the Rose Bengal and Brilliant Green. As demonstrated in Figure 11.20 a and b, excited charge transfer from these dyes is facilitated by the +8V poling and inhibited by the –8 V poling pretreatments, strongly concluding that charge transfer from the molecular dyes could be well controlled by the poling of the ferroelectric substrates.

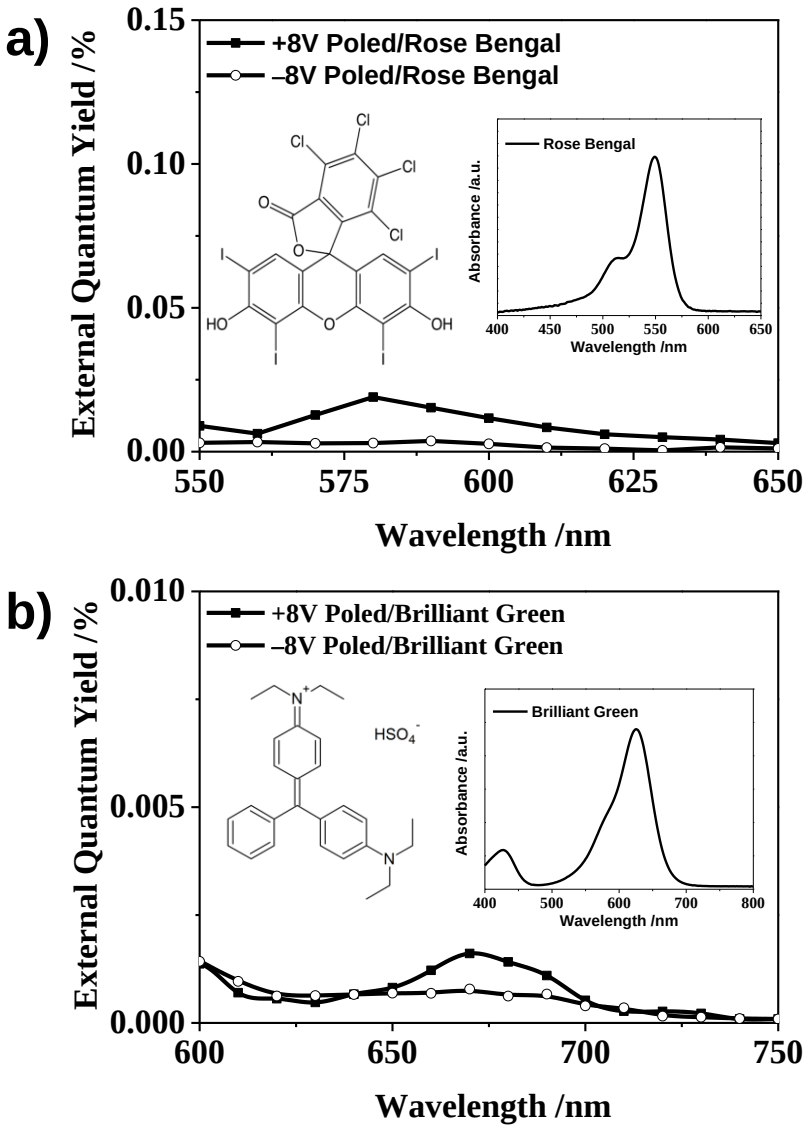

Figure 11.20 Investigation of tuning charge transfer from excited Rose Bengal and Brilliant Green

3. Additional data for chapter 7

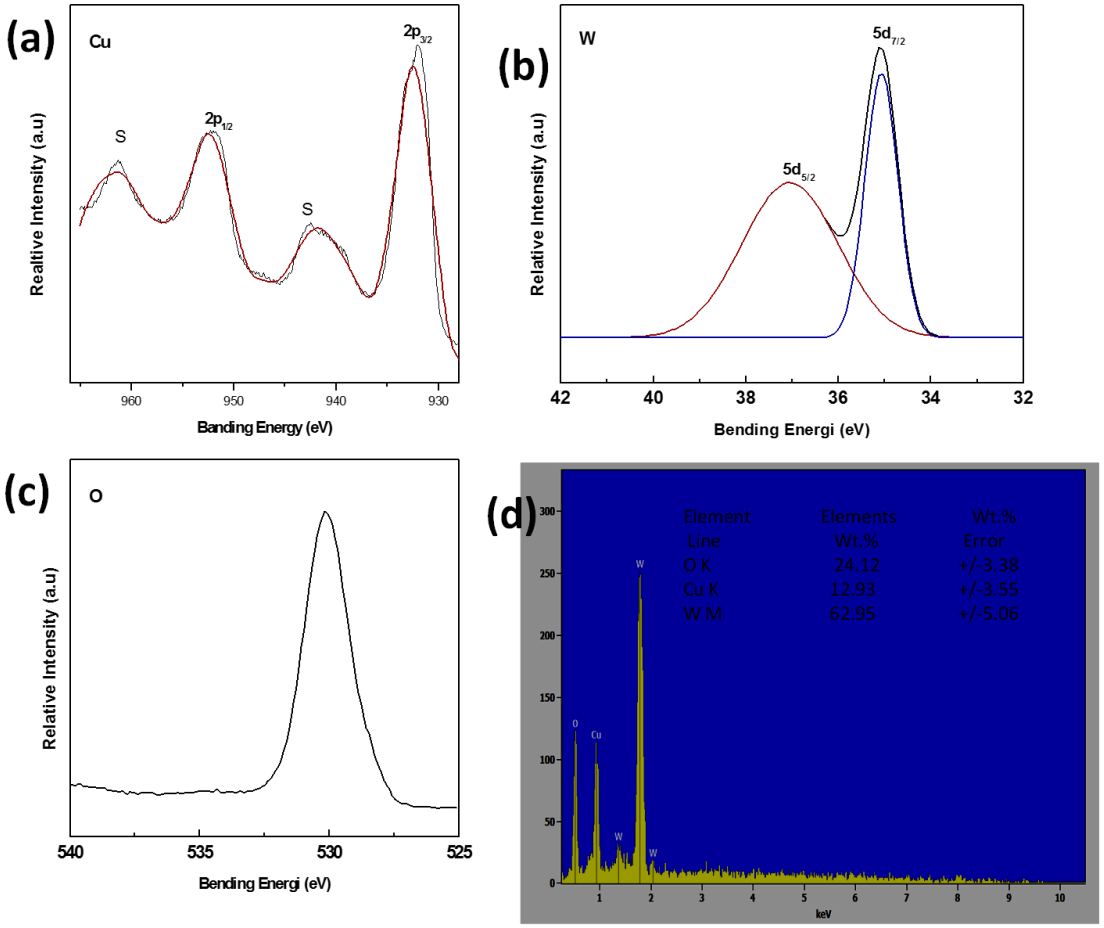

Figure 11.21 XPS survey of $CuWO_4$, core-level XPS of of Cu2p, core-level XPS of W 5d, and core-level XPS of O1s, respectively

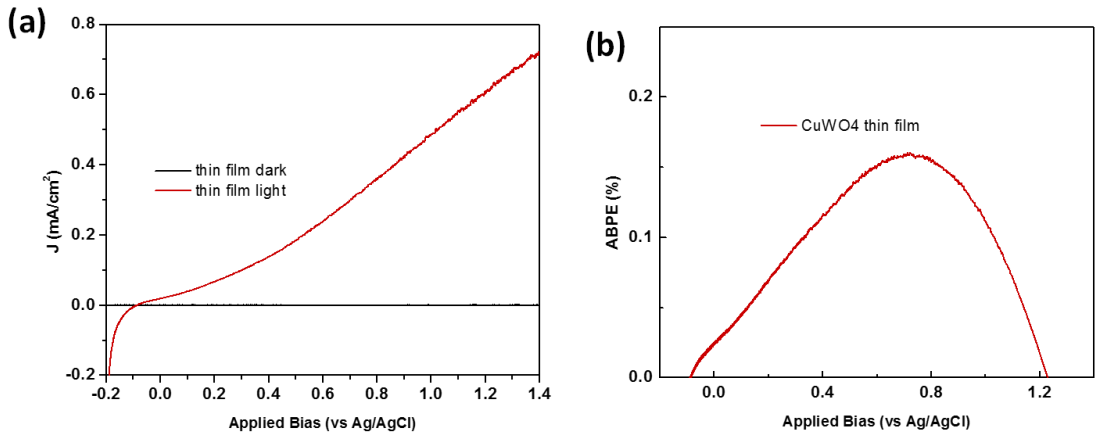

Figure 11.22 (a) LSV of a CuWO4 thin film photoanode in a three-electrode configuration described in the text and under AM 1.5G sunlight. The scans are collected from −0.2 to 1.4 V versus Ag/AgCl. (b) ABPEs of the relevant electrodes from (a).

Tabel 10.2 Previous report for photoelectrochemical measurements of the kinds $CuWO_4$ photoanode for oxygen evolution reaction

Photoanode Speciment	**Solution as Electrolyte**		**Linear potential sweep measurements**		**Constant potential measurements**	
			Scan rate (mV s^{-1})	**J_{ph} mA cm^{-2}) at 1.57 RHE**	**Potensial (V vs RHE)**	**J_{ph} (mA cm^{-2}) after 1 h**
This work:						
CuWO4	0.1 M Na_2SO_4	pH 6.8	10	0.3	1.21	0.26
CuWO4 nanocore	0.1 M Na_2SO_4	pH 6.8	10	1.01	1.21	0.98
$CuWO_4$ nanoflake [209]	0.1 M borate buffer	pH 9	10	0.58	1.57	0.52
H-treated $CuWO_4$ nanoflake [210]	0.1 M phosphate buffer	pH 7	10	0.58	-	-
	0.1 M borate buffer	pH 9	10	0.84	1.57	0.69
	1 M phosphate buffer	pH 7	10	0.82	-	-
$CuWO_4$ [207]	0.1 M borate buffer	pH 9	10	0.22	-	-
	0.1 M phosphate buffer	pH 7	10	0.2	-	-
	0.05 M H_2SO_4	pH 1	10	0.15	-	-

$CuWO_4$ [207]	0.1 M phosphate buffer	pH 7	20	0.26	1.23	0.064
	0.1 M phosphate buffer	pH 5	-	-	1.23	0.072
	0.1 M borate buffer	pH 7	-	-	1.23	0.075
	0.1 M phosphate buffer	pH 3	-	-	1.23	0.062
$CuWO_4$ [219]	0.1 M phosphate buffer	pH 7	10	0.26	1.13	0.07
	0.1 M acetate buffer	pH 2.9	10	0.23	0.874	0.038
	0.1 M $HClO_4$	pH 1.2	10	0.22	0.772	0.003
$CuWO_4$ [220]	0.5 M borate buffer + 0.2 M KCl	pH 7	50	0.14	-	-
$CuWO_4$ [221]	0.1 M borate buffer + 0.2 M KCl	pH 9	20	0.15	1.23	0.09
$CuWO_4$ [222]	0.1 M phosphate buffer	pH 7	-	0.04	1.23	0.02
$CuWO_4$ [223]	0.33 M H_3PO_4	pH 0	25	0.36	-	-
$CuWO_4$ [224]	0.1 M Na_2SO_4	pH 6.8	20	0.18	1.60	0.16
CuWO4+H-treated [225]	0.1 M Na_2SO_4	pH 6.8	20	0.55	1.60	0.45
$CuWO_4$ [226]	0.1 M phosphate buffer	pH 7	10	-	1.21	0.07
$CuWO_4$ [227]	1.0 M Na_2SO_4	pH 7	25	0.40	-	-

Scientific Contributions

During this PhD program, I authored 4 papers in SCI-indexed international scientific journals including 2 papers in journals with impact factor higher than 11 (Nature Communications, Angewandte Chemie International Edition) and 2 papers in journals with impact factor higher than 8 (Applied Catalysis B: Environmental, Journal of Materials Chemistry A). The published papers have been cited for more than 120 times (Source: Google scholar database).

Moreover, I have given 4 contributions at conferences, including 3 talks and 1 poster.

Peer-reviewed Publications in SCI-indexed Scientific Journals

1. Dawei Cao, **Nasori Nasori** (**Shared first author & equal contribution**), Zhijie Wang, Liaoyong Wen, Rui Xu, Yan Mi, Yong Lei*, 'Facile Surface Treatment on Cu_2O Photocathodes for Enhancing the Photoelectrochemical Response', **Applied Catalysis B: Environmental** (Impact factor:8.26), 2016, S0926-3373(16)30448-9 DOI: http://dx.doi.org/doi:10.1016/j.apcatb.2016.06.010
2. Dawei Cao, **Nasori Nasori** (**Shared first author & equal contribution**), Zhijie Wang, Yan Mi, Liaoyong Wen, Ying Yang, Shengchun Qu, Zhanguo Wang and Yong Lei*,' p-Type $CuBi_2O_4$: an Easily Accessible Photocathodic Material for High-Efficiency Water Splitting', **Journal of Materials Chemistry A** (Impact factor: 8.8), DOI: 10.1039/c6ta01234e, 2016
3. Zhijie Wang, Dawei Cao, Liaoyong Wen, Rui Xu, Manuel Obergfell, Yan Mi, Zhibing Zhan, **Nasori Nasori**, Jure Demsar, and Yong Lei*, 'Manipulation Of Charge Transfer And Transport In Plasmonic-Ferroelectric Hybrids For Photoelectrochemical Applications', **Nature Communications** (Impact factor: 11.470), (DOI: 10.1038/ncomms10348), 2016
4. Dawei Cao, Zhijie Wang, **Nasori Nasori**, Liaoyong Wen, Yan Mi, Yong Lei*, 'Switchable Charge-Transfer In The Photoelectrochemical Energy-Conversion Process Of Ferroelectric $BiFeO_3$ Photoelectrodes', **Angewandte Chemie International Edition**, 2014, 126, 11207-11211 (Impact factor: 11.261)

Manuscripts under revision or preparation

1. **Nasori Nasori**, Dawei Cao, Zhijie Wang, Ying Yang, Shengchun Qu, Zhanguo Wang, and Yong Lei*, 'Realizing Super-long Cu_2O Nanowires Arrays for High-efficient Water Splitting Applications with a Convenient Approach', **(Power Energy, under review)**
2. **Nasori Nasori**, Dawei Cao, Zhijie Wang, Ying Yang, Shengchun Qu, Zhanguo Wang, Agus Rubiyanto and Yong Lei*, 'First Optimation Of Space Effect In-Between $CuWO_4$ Nanograin Arrays For Supreme Performance of Photoanode Water Splitting', (**Under preparation**)

Conference contributions

1. **Nasori Nasori**, Dawei Cao, Zhijie Wang, Yang Xu, Yong Lei,'Polling Ferroelectric $BiFeO_3$ Photoelectrodes for Switchable Charge-Transfer in The Photoelectrochemical Energy-Conversion Process, Dresden, DPG Conference, 2017 (**Talk**)
2. Zhibing Zhan, **Nasori Nasori**, Dawei Cao, Yong Lei, 'Plasmonic and Novel p-type Material for Aplication in Pthotoelectrochemical (PEC)', 3st International Conference on Challenges and Perspectives of Functional Nanostructures, July 29-31, 2016, Ilmenau, Germany. (**Talk**)
3. Zhijie Wang, Dawei Cao, Yan Mi, **Nasori Nasori**, Ahmad Al-Haddad, Sammar Tarish, Chengliang Wang, Yong Lei,'Manipulations of Various Nano-structures for Photoelectrochemical and Electronic Applications', 1st International Conference & 3rd International MacroNano-Colloquium on the Challenges and Perspectives of Functional Nanostructures (CPFN), July 29-31.2014, Ilmenau, Germany. (**Talk**)
4. **Nasori Nasori**, Dawei Cao, Yong Lei' '*p*-Type $CuBi_2O_4$: An Easily Accessible Photocathodic Material for High-Efficiency Water Splitting', 3st International Conference on Challenges and Perspectives of Functional Nanostructures, July 29-31, 2016, Ilmenau, Germany.(**Poster**)

Declaration

I hereby confirm that this Ph.D. dissertation entitled "Design of Metal Oxide-Based Electrodes for Efficient Photoelectrochemical Water Splitting" represents my own work for the degree of Doctor of Philosophy under the supervision of Prof. Dr. Yong Lei. All dates and information in this work that have been directly or indirectly derived from other sources are clearly stated. This dissertation has not been submitted, in part or in whole, for the award of any other degree or examination in any other University or other tertiary institution. I have acknowledged all the sources of help, and I have made a clear statement of what was done by others. Most of the results have been published in scientific journals or elsewhere. I am aware that any falsity of this declaration would be regarded as an attempt at deception and will cause the derogation of the doctoral procedure.

Ilmenau, 14th September 2017

Nasori